This Dissertation Committee for Daniel John Dorsey
certifies that this is the approved version of the following dissertation:

Development of Neutron Beam Analytical Techniques for Characterization of Carbon Fiber Composite Materials

Committee:

William S. Charlton, Supervisor

Robert Hebner

Sheldon Landsberger

Arumugam Manthiram

Kenneth Ball

Development of Neutron Beam Analytical Techniques for Characterization of Carbon Fiber Composite Materials

by

Daniel John Dorsey, B.S., M.S.

Dissertation
Presented to the Faculty of the Graduate School of
the University of Texas at Austin
in Partial Fulfillment
of the Requirements
for the Degree of
Doctor of Philosophy

The University of Texas at Austin

May 2003

Dedication

To my wife, Staci.

Acknowledgments

The author wishes to express sincere gratitude to his advisor, Dr. William S. Charlton, for his advice and guidance during this investigation. It has been a privilege to work with Dr. Charlton the past 3 years.

I would also like to extend my thanks and appreciation to the Center for Electromechanics for providing the motive for this investigation, and for their assistance in supplying composite test samples.

Thanks are also due to my dissertation committee, the faculty of the Nuclear and Radiation Engineering program, and the staff of the Nuclear Engineering Teaching Laboratory. The reactor operators deserve special recognition. Without their help, dedication, and long hours I would still be sitting in the reactor bay acquiring data.

Development of Neutron Beam Analytical Techniques for Characterization of Carbon Fiber Composite Materials

Publication No. __________

Daniel John Dorsey, Ph.D.
The University of Texas at Austin, 2003

Supervisor: William S. Charlton

The cold neutron prompt gamma ray activation analysis (PGAA) facilities at the University of Texas at Austin (UT) Nuclear Engineering Teaching Laboratory (UT-NETL) have been used to characterize properties of advanced, carbon-fiber reinforced, epoxy-matrix composite materials. A method was developed using PGAA to measure the carbon fiber volume of different sample coupons. PGAA was also used to quantify amounts of water absorbed and desorbed from sample coupons. In support of these measurements, the PGAA facilities were optimized for the handling of unique composite samples. In particular, neutron and gamma shielding was reconfigured to minimize interference and background noise, and sample holders were designed to maximize radiative capture reaction rates within test samples. To allow quantitative calculations to be made, the temporal and spatial variations in the guided and focused cold neutron beam were characterized. The results of this investigation demonstrate the use of PGAA as a tool for the non-destructive analysis of advanced composite materials.

Table of Contents

List of Tables

List of Figures

CHAPTER 1. Introduction

1.1 Background

Material science and engineering has long since evolved to the point where composite materials can be fabricated with strength to weight ratios superior to more common engineering materials such as stainless steel; however, due to the complex, heterogeneous structure of most composite materials, accurate characterization of ultimate strength, failure mechanisms, and factors influencing ultimate strength and failure mechanisms has not been performed. For the most part, failure modes have not been rigorously investigated because it has generally been easier to over build composite components with large safety factors, ensuring that the ultimate strength of the material would never be exceeded. As the use of composite materials moves into more advanced applications that push the limits of material properties, the accurate determination of ultimate material strength and failure mechanisms becomes important. Calculations to gauge material performance are especially critical for space applications, where launch costs are proportional to mass and maintenance can be intermittent at best. Unfortunately, non-destructive tools and techniques to completely evaluate the composite materials are not readily available.

A program is currently underway at the University of Texas (UT) Center for Electromechanics (UT-CEM) to develop high strength, light weight composite flywheels using carbon fibers in a polymer matrix. Current non-destructive evaluation (NDE) techniques used to analyze polymer matrix composite materials at UT include acoustic sounding and x-ray radiography. Neutron radiation is very penetrating, and it is suspected that neutron beam surveys, particularly prompt gamma ray activation analysis (PGAA), will be a useful complement to the more conventional NDE techniques and possibly replace other destructive techniques. The application of PGAA to carbon/polymer composites will also require the refinement of PGAA techniques and modeling.

The UT Nuclear Engineering Teaching Laboratory (UT-NETL) is home to the UT-TRIGA, a 1 MW TRIGA Mark II research reactor. Beam port 3 of the UT-TRIGA is dedicated to the Texas Cold Neutron Source (TCNS), one of only two cold neutron sources in the country, and the only cold neutron source at a university. PGAA is the primary application for the TCNS. The facilities of the UT-CEM and UT-NETL, as well as their close proximity on the UT J.J. Pickle Research campus, combine to make a unique partnership and have lead to this investigation.

1.2 Problem Statement

The UT-CEM has performed destructive hydroburst testing of cured polymer matrix carbon fiber rings. Failure pressures have been reproducible, but occasionally batches fail at lower pressures for unknown reasons. It is unknown if these deviations are due to material flaws, or an error in the fabrication process. Evaluation techniques employed by the UT-CEM, both destructive and non-destructive, have not been able to characterize the factors that lead to substandard batches of composite rings. PGAA is a previously unused tool for the analysis of these materials.

Cold neutron PGAA can be used to identify the isotopic constituents of composite samples, but calibration techniques to make quantitative determinations and comparisons between samples of different constituents and geometries must be developed. It is hypothesized that isotopic constituent data can be used to infer material properties such as fiber volume and characteristics such as water content. The objective of this dissertation is develop cold neutron PGAA techniques and their application to the characterization of carbon reinforced polymer matrix composite properties that may influence the material strength.

The PGAA experiments described in this dissertation will be considered a proof of principle to demonstrate that PGAA can be used to characterize polymer matrix carbon composite materials. Low neutron flux levels and the low power level of the UT-NETL, coupled with the high ^{1}H background in the polymer matrix composites, significantly increase the time required to obtain useful statistics for PGAA data. A secondary goal of these experiments will be to show the usefulness of these techniques if applied at a higher power facility.

1.3 Review

1.3.1 Prompt Gamma Activation Analysis

PGAA is a non-destructive nuclear technique that can be used to obtain information on the isotopic constituents in a sample, in quantities ranging from trace levels to major abundances [1]. PGAA is based on the detection of gamma rays emitted after radiative neutron capture reactions:

$$ {}^{A}_{Z}X + {}^{1}_{0}n \rightarrow \left[{}^{A+1}_{Z}X \right]^{*} \rightarrow {}^{A+1}_{Z}X + \gamma \; . $$

Neutron binding energy typically leaves the compound nucleus in an excited state, which then promptly decays by gamma emission. Prompt gamma rays are characteristic to the excited nucleus and can be used to identify the target isotope. Neutron and high-energy gamma radiation are both penetrating, and PGAA can be used to probe a wide range of sample materials. In a properly calibrated system, quantitative determinations can be made.

PGAA can be performed on any type of sample with little preparation. It is typically used as a complement to neutron activation analysis (NAA) in situations where radioactive products cannot be formed. This technique is most useful for light elements, such as H, B, C, N, Cl, and S [1]. These elements are commonly found in polymer matrix carbon composites. In practice, the difference between NAA and PGAA is that PGAA is an online technique where data is acquired during irradiation. Because of the proximity of the photon detector to the neutron beam, background shielding can pose significant challenges. PGAA is perhaps more similar to x-ray fluoroscopy in the sense that emissions are stimulated by exposing a sample to radiation, although the radiation involved with prompt gamma work is much more penetrating. A general diagram of a possible PGAA facility is shown in Figure 1.1.

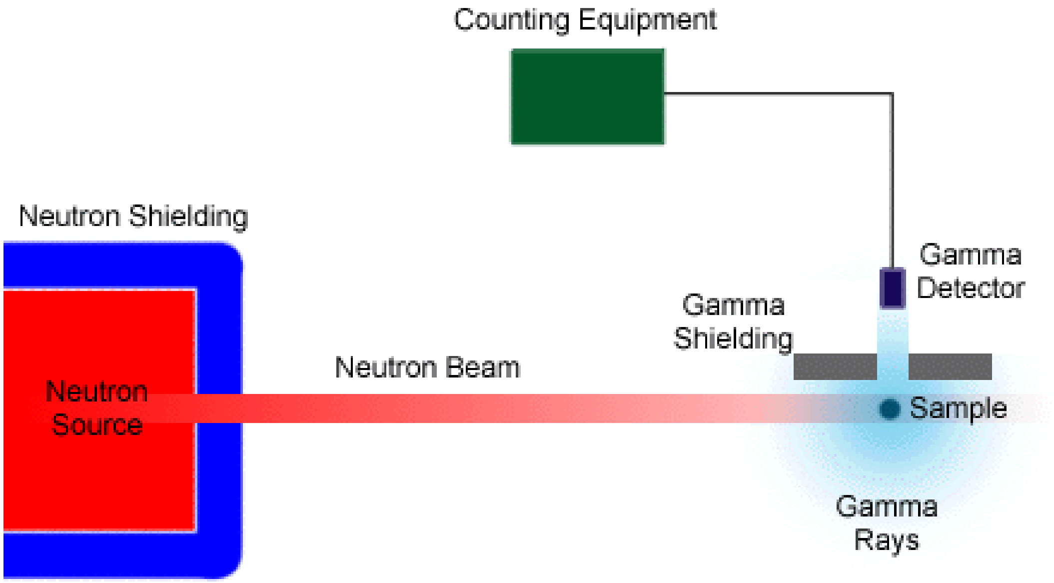

Figure 1.1. A general schematic for a PGAA facility.

Consider the prompt gamma analysis of hydrogen and carbon. Natural hydrogen is composed of ^{1}H (99.985%) and ^{2}H (0.015%). Natural carbon is composed of ^{12}C (98.89%) and ^{13}C (1.11%). Atomic mass data for hydrogen and carbon isotopes is shown in Table 1.1. Hydrogen and carbon are ill suited for NAA because the principal radioactive activation products, ^{3}H and ^{14}C, are produced in small quantities and do not decay by gamma ray emission (a requisite for NAA). Hydrogen and carbon emit prompt gamma rays during radiative capture events, however, and are candidates for PGAA.

Table 1.1. Atomic Mass Data for PGAA of H and C

Isotope	Atomic Mass [amu]
^{1}H	1.0078250
^{2}H	2.0141018
^{12}C	12.0000000
^{13}C	13.0033548
^{1}n	1.0086649

The radiative capture of neutrons by ^{1}H or ^{12}C results in a compound nucleus excited by the binding energy of the neutron. The excitation energy of the compound nucleus formed during the $^{1}H(n,\gamma)^{2}H$ reaction can be calculated by

$$E = \left\lfloor \left(M_{^1H} + M_n\right) - M_{^2H} \right\rfloor \cdot 931.49\, {}^{MeV}\!/_{amu}\,, \qquad \text{1-1}$$

where M is atomic mass and E is energy. Inserting atomic masses from Table 1.1 into equation 1-1 yields a compound nucleus excitation of 2224.5 keV. The same calculation can be applied to the $^{12}C(n,\gamma)^{13}C$ reaction to calculate a compound nucleus excitation of 4946.3 keV. Energy level diagrams for the ^{2}H and ^{13}C compound nuclei are shown in Figure 1.2 and Figure 1.3, respectively. Nuclear energy levels in Figure 1.2 and Figure 1.3 correspond with measured prompt gamma energies for ^{1}H and ^{12}C radiative capture reactions (see Appendix E).

Prompt gamma spectra generally cover wide energy ranges and individual gamma rays are well separated, even for spectra with many prompt gamma energies. ^{1}H is a simple case with only a single prompt gamma emitted with a 100% yield. Quantitative analysis of prompt gamma spectra can be complex, but the identification of prompt gamma rays and interferences within a spectrum can be easier than for NAA. Decay spectra can have many gamma energies, but tend to be compressed over a smaller energy range. Figure 1.4 shows the energy levels for the beta transition of ^{152}Eu to ^{152}Sm. ^{152}Eu is an isotope commonly used for energy calibrations due to its many decay energies.

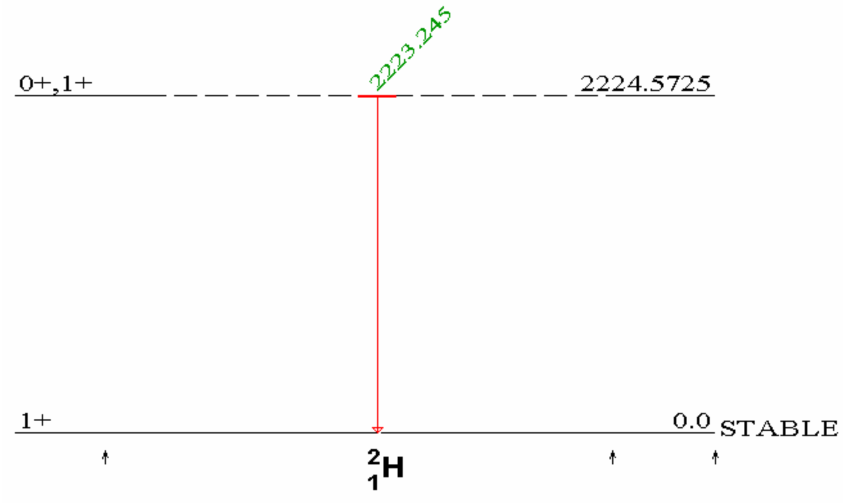

Figure 1.2. Nuclear energy level diagram for the ^{1}H(n,γ)^{2}H transition (data from ENSDF).

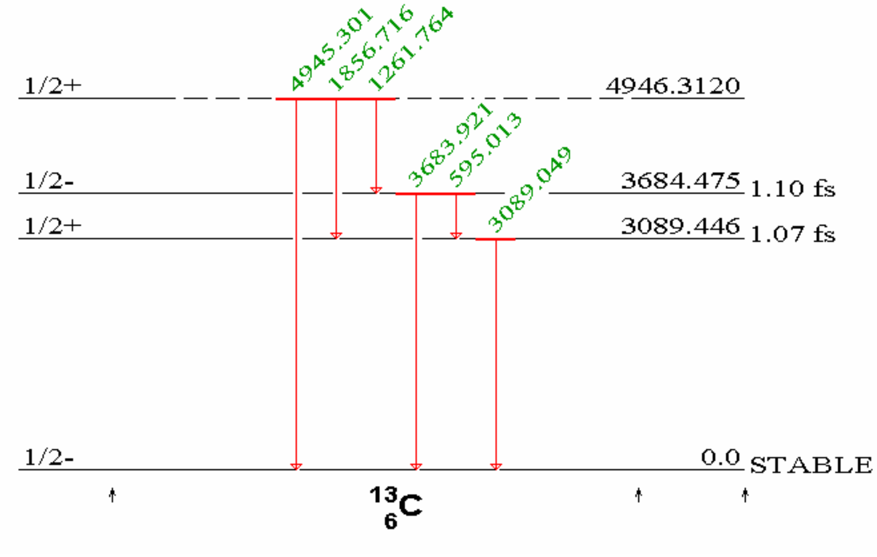

Figure 1.3. Nuclear energy level diagram for ^{12}C(n,γ)^{13}C transition (data from ENSDF).

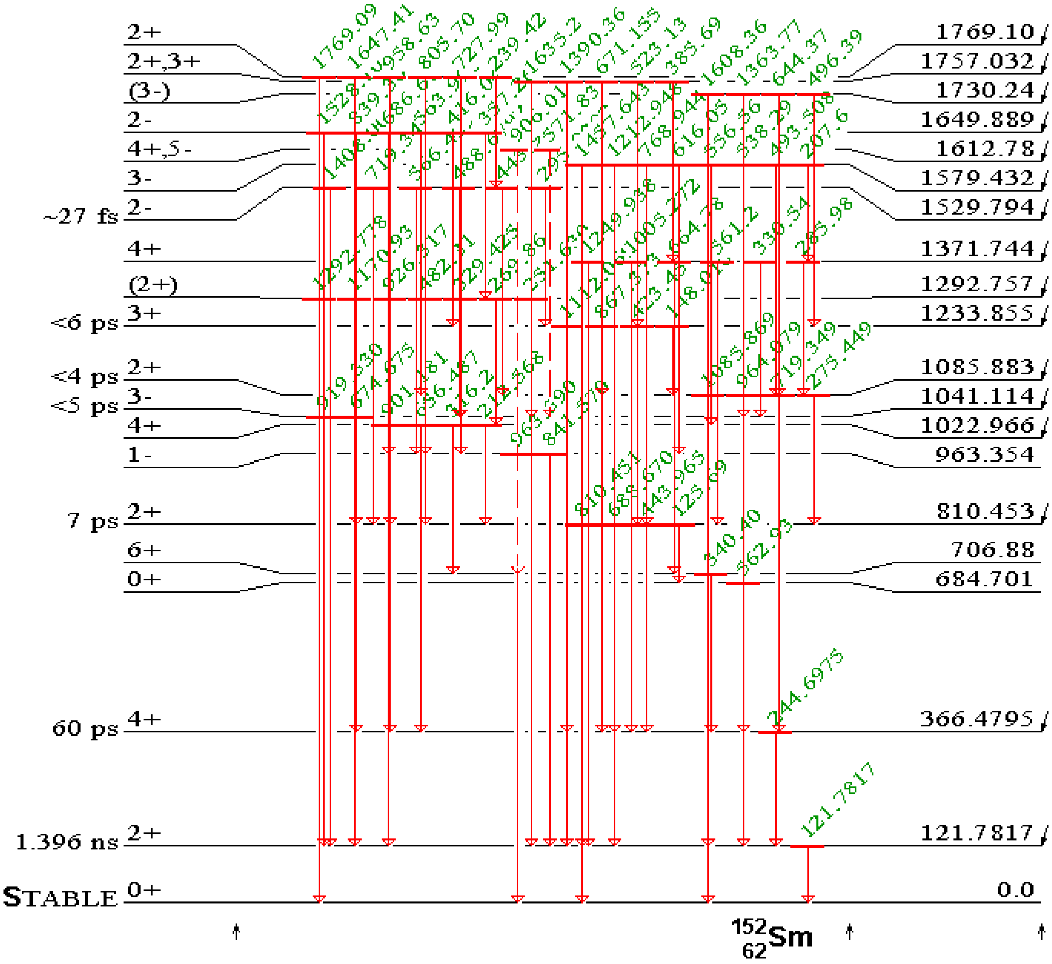

Figure 1.4. Nuclear energy level diagram for the β⁻ decay of ^{152}Eu to ^{152}Sm (data from ENSDF).

Radiative capture cross sections for ^{1}H and ^{12}C are shown in Figure 1.5 for a wide range of neutron energies and the cross sections for interaction with neutrons at standard room temperature is indicated. The plot shows that as neutron energy decreases, the radiative capture probability increases. The use of neutrons at energies below standard room temperature is advantageous for PGAA investigations.

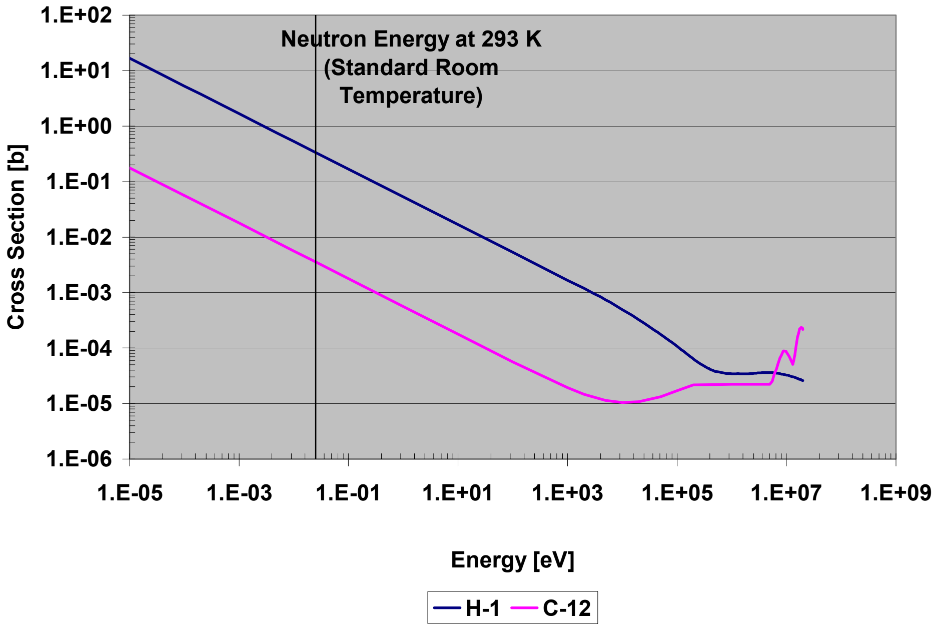

Figure 1.5. Radiative capture cross sections for ^{1}H and ^{12}C at 300 K (data from JENDL-3).

1.3.2 Cold Neutrons

PGAA relies on the detection of gamma rays emitted after neutron absorption events. Any steps that can be taken to increase the prompt gamma emission rate will increase the system sensitivity. Neutron absorption cross sections are typically proportional to the inverse of neutron velocity at low energies, as shown in Figure 1.5 and calculated by equation 1-2,

$$\sigma_\gamma(v_n) = \sigma_{\gamma 0}\frac{v_{n0}}{v_n}. \qquad 1\text{-}2$$

If the neutron velocity can be cut in half, the probability of a radiative capture event occurring can be doubled. The actual radiative capture cross section for ^{1}H at low velocities is shown in Figure 1.6. Thermal neutrons have a Maxwellian spread of velocities. At room temperature (293 K), this Maxwellian has an average velocity of 2200 m/s, corresponding to an energy of 0.025 eV.

Neutrons interact by scattering and absorption reactions to different degrees with any medium through which they pass. Low Z materials in which neutrons predominately scatter are considered moderators, and scattering reactions with these materials will result in significant decreases in neutron energy. Scattering neutrons will continue to lose energy until they reach the same energy range as the moderating medium. This is considered thermal equilibrium. If a moderator is chilled to cryogenic temperatures, scattering neutrons will come to thermal equilibrium at cryogenic temperatures. Such a cryogenically chilled moderator can be used to generate cold neutrons. The slower neutrons are then more apt to be absorbed in a sample, and can increase the prompt gamma emission rate.

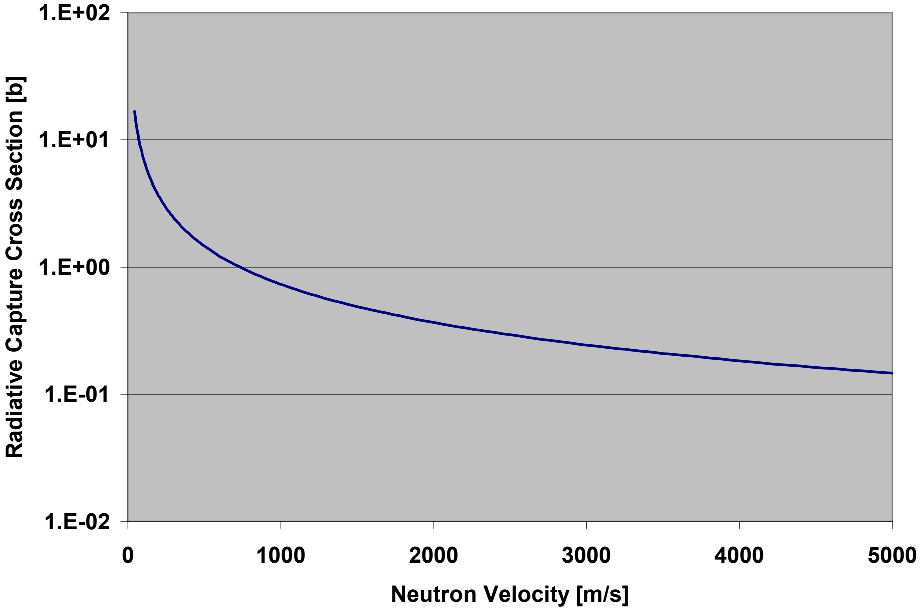

Figure 1.6. ^{1}H radiative capture cross section for slow neutrons (data from ENDF/B-VI).

All particles exhibit wavelength, due to wave-particle duality. The De Broglie wavelength of a particle is calculated as

$$\lambda = \frac{h}{p}, \tag{1-3}$$

where h is Planck's constant, and p is the particle momentum. A characteristic "thermal" neutron with a velocity of 2200 m/s has a wavelength of 1.8 Å. By comparison, a neutron in thermal equilibrium with liquid nitrogen at 77 K will have a velocity of 1200 m/s and a wavelength of 3.51 Å. In general, cold neutrons are considered neutrons below the energy 5.24 meV [2], which corresponds to a velocity of 1000 m/s. This energy corresponds to a wavelength of 3.95 A, the Bragg cut-off for beryllium.

The use of cold neutrons for PGAA activities is becoming more common as new reactor facilities are developed world-wide. Cold neutrons also display heightened wave-like properties and can be directed through neutron guides, much like photons through fiber optics. Guided neutron beams do not suffer from typical $1/r^2$ losses in intensity and can also be steered away from line of sight to the neutron source, resulting in an intense beam with low gamma background.

The wave-like properties of cold neutrons also allow for neutron focusing. The increased neutron flux in localized areas leads to increased reaction rates, and enhanced PGAA performance. Cold neutrons have been focused using converging guides [3] and more recently, with highly focusing poly-capillary lenses [4,5,6].

1.3.3 PGAA Facilities and Applications

Several dedicated PGAA facilities are in operation throughout the world, and there are many isotopic neutron source based field devices in use for various applications. This section will catalog active PGAA facilities and many current applications of PGAA. The UT-NETL PGAA system will be discussed in detail in Chapter 2.

The Center for Neutron Research (CNR) at the National Institute of Standards and Technology (NIST) has instruments for cold and thermal PGAA and is perhaps the preeminent facility in the world for PGAA. The CNR is home to a 20 MW heavy-water moderated research reactor. The thermal prompt gamma spectrometer is located at the end of a collimated vertical beam with a sapphire filter that delivers a flux of 3.0×10^{8} n/cm^{2}/s [7]. A second system is in place on a guided cold neutron beam [8] that delivers a thermal equivalent flux of 8.3×10^{8} n/cm^{2}/s [7]. Both the cold and thermal prompt gamma spectrometers are Compton suppressed [7].

Liquid H at ~20 K is the cold moderator at NIST. The cold neutron PGAA instrument is 41 m from the cold source, and the guided neutrons are filtered through Be and Bi crystals at 77 K in route to the PGAA sample. A 26% efficient HPGe detector inside a BGO Compton suppression detector is used to measure prompt gamma rays. 10 mm of Pb shielding surround the detector, and further neutron shielding is provided by ^{6}Li glass and ^{6}LiF loaded polymers. Samples and the detector assembly are mounted on an aluminum plate at a fixed distance from each other to ensure reproducible positioning, and the sample chamber atmosphere can be controlled. Data is acquired with a 16k channel ADC and Canberra Nuclear Data spectroscopy software [8].

The PGAA facilities at NIST have been used extensively for many applications, and to develop new PGAA techniques. Extensive work has been performed at NIST to characterize the effects of cold and thermal neutron scattering within PGAA samples [9,10,11,12,13], including the effects of sample temperature [14]. NIST has also used PGAA as part of the certification process for Standard Reference Materials (SRMs) since 1979 [15]. The PGAA facilities at NIST have been used to determine the constituents of dietary supplements [16] as well as meat homogenates [17]. PGAA is also a common technique for ^{1}H analysis [18]. Hydrogen and other elemental analysis at NIST [19] has included the study of ^{1}H content in doped $SrCeO_3$ [20] and Titanium [21]. NIST is also applying PGAA to the analysis of "high-tech" materials [22], including ^{1}H uptake in H-ZSM-5 zeolites [23] and the characterization of nafion membranes [24]. Trace elements in sapphire components for the Laser Interferometer Gravitational Wave Observatory have been examined using PGAA [25], as well as chloride distributions in concrete [26].

The Institute of Isotope and Surface Chemistry in Budapest, Hungary, is home to the Budapest Research Reactor (BRR), a 10MW research reactor. The BRR has a guided neutron beam capable of delivering a thermal equivalent of 2×10^{6} n/cm^{2}/s to a PGAA station monitored by a Compton suppressed HPGe detector [7]. The beam size is approximately 2 cm by 2 cm, and the sample to detector distance is 23.5 cm. Samples are held in a sealed target chamber lined with ^{6}Li poly [27]. The current PGAA facility is the result of refurbishments and upgrades to the BRR [28]. The main research effort underway at the BRR is the development of a new prompt gamma library in collaboration with Lawrence Berkeley National Laboratory [7,29,30,31]. Additional work at the BRR has been performed in areas of detector calibration [32], hydrogen determination [33], and the analysis of metals [34,35].

At India's Bhabha Atomic Research Center, there is a PGAA facility installed at the 100 MW Dhruva research reactor. The thermal guided beam delivers 1.4×10^{7} n/cm^{2}/s with a beam measuring 2.5×10 cm^{2} to a PGAA spectrometer. The detector system uses an 8k channel MCA and a 22% efficient HPGe detector [7]. Recent work performed at the Bhabha PGAA facility includes the study of the ^{59}Co(n,γ) reaction and the induced ^{60}Co activity as an efficiency standard for PGAA measurements [36].

The SNU-KAERI PGAA facility began operation at the 30 MW HANARO research reactor in Korea in May of 2001 [7] as the result of an effort to characterize ^{10}B and develop boron neutron capture therapy capabilities at HANARO [37]. The facility uses a set of pyrolytic graphite crystals to direct a polychromatic thermal neutron beam with a neutron flux of 7.9×10^7 n/cm^2/s in a 1 cm^2 area at the PGAA sample position [38]. The PGAA system uses a 43% efficient n-type HPGe detector with a fast 16k ADC for spectrum acquisition. The polychromatic beam is collimated with borated plastic, Pb, and polyethylene. A final collimator of ^{6}LiF is used to minimize background radiation, ^{6}LiF shielding is used extensively around the HPGe detector [39].

The Vietnam Atomic Energy Commission maintains a PGAA facility at their 500 kW Dalat Nuclear Research Reactor. The filtered thermal beam delivers 2.1×10^7 n/cm^2/s to the PGAA sample position, and prompt gammas are measured with a 90 cc HPGe detector. The Dalat facility is currently working to develop k_0 factors for several elements in partnership with the previously listed facilities [7]. k_0 factors can be used for the relative comparison of PGAA data and are discussed in Chapter 3.

The JRR-3M reactor is a 20 MW light water research reactor operated by the Japan Atomic Energy Research Institute (JAERI). The JRR-3M facility has a movable prompt gamma spectrometer that can be set at cold or thermal neutron guides, delivering 1.1×10^8 and 2.4×10^7 n/cm^2/s, respectively [40]. The system was designed to minimize background by using a HPGe-BGO Compton suppressed detector system, a PTFE (Teflon) sample chamber that can be purged with He, and LiF tiles for neutron shielding [41]. The PGAA facility at JRR-3M has seen extensive use over a wide range of areas. It has been used for boron determination in animal samples [42], and heavy metal uptake in rats [43]. PGAA has been applied to the analysis of marine oil, sediment, and bivalve samples at JRR-3M [36]. Studies have even been performed to analyze contaminants in agricultural samples [44].

Non-reactor based neutron sources have also been used to perform prompt gamma experiments. The SINQ spallation source at the Paul Scherrer Institute (PSI) in Villigen, Switzerland, is home to a cold neutron prompt gamma activation facility. Spallation neutrons are provided by acceleration protons through a 590 MeV accelerator into a heavy water cooled array of zircaloy rods in an aluminum container. A liquid deuterium moderator at 25 K cools a portion of the released neutrons, and a cold guide delivers a neutron flux of 6.9×10^7 n/cm^2/s to the PGAA sample at a proton current of 1 mA. The PSI PGAA facility utilizes capillary focusing optics to maximize beam intensity, and antimony free Pb and ^{6}LiF shielding to minimize background [45]. Prompt gamma investigations at the PSI have included traditional PGAA work in boron [46] and hydrogen [47] characterization, as well as more specialized work such as the two dimensional scanning of a geologic sample from the Oklo, Gabon, natural reactor site [48]. Another fixed accelerator driven facility is under development at King Fahd University of Petroleum and Minerals (KFUPM) in Saudi Arabia. The PGAA setup at KFUPM uses moderated 2.8 MeV neutrons from D-D accelerator pulses. Flux characterization has agreed reasonably with Monte Carlo calculations for the KFUPM setup [49].

In practice, prompt gamma measurements only require a neutron source and a photon detector. Portable prompt gamma devices have been developed using pulsed or isotopic neutron sources for applications where samples cannot be taken to a reactor or accelerator based facility. Although data analysis can be complex, the minimal equipment required and online nature of data acquisition has made PGAA a useful field technique.

Geological measurements often require portable PGAA devices, since it is impractical to bring large geological formations into a reactor facility. A common use for such portable devices is borehole logging for the analysis of coal deposits for multiple elements [50,51]. Also of particular interest is the monitoring of coal input and ash output of furnaces as a method of online monitoring of coal quality [52,53,54] and the immediate application of this analysis to optimize the combustion process. The characterization of boron in coal ash is also important to gauge environmental impacts [55]. Environmental prompt gamma measurements [56] often require portable systems as well, since natural samples cannot always be transported to a laboratory. A ^{252}Cf based probe was developed in Taiwan for the in situ analysis of river salinity [57] and lake pollutants [58,59].

PGAA is also useful for the identification of illicit materials, particularly high explosives. The low-Z nature of energetic compounds, coupled with low density, make them ideally suited for analysis by PGAA. Several systems have been considered for the screening of baggage for explosives at airports [60,61]. The assay of larger containers by PGAA has also been investigated [62]. Explosives detection with PGAA has reached the state where neural networks are being taught to identify PGAA signatures for explosives [63], and natural interferences are being investigated [64]. Prompt gamma measurements have also been used to identify fission events for safeguard purposes [65].

Several industrial applications require portable PGAA devices. Corrosion in iron pipes can be detected by prompt gamma emission rapidly, and without regard to pipe temperature or surface conditioning. Organic scales, which may be missed by more conventional techniques, can also be detected by PGAA [66]. Prompt gamma measurements have also shown promise for the analysis of “green liquor”, an aluminum form during the refinement processing, and may replace current atomic absorption spectroscopy techniques [67]. PGAA can also be applied to the analysis of planetary materials throughout the solar system [68].

1.3.4 PGAA Efficiency Calibration

Prompt gamma detection efficiency is the ratio of prompt gamma rays detected per prompt gamma rays emitted. Detection efficiency is unique to sample-detector geometry as well as the physical characteristics of the detector, and is a function of gamma ray energy. The measurement of detection efficiency is required to directly determine the radiative capture reaction rate from the measured number of prompt gamma rays.

Efficiency is simply the ratio of detections per event, as shown in equation 1-4 for decay sources,

$$\varepsilon_x = \frac{C}{y_x \cdot \int_{t_{start}}^{t_{end}} A(t)dt} . \qquad 1\text{-}4$$

In equation 1-4, C is the measured peak area in counts, y_x is the gamma yield in gamma rays per decay, $A(t)$ is the decay source activity (in decays per unit time), and t is time. Decay source activity decreases with a half-life characteristic to the particular isotope in use. For isotopes with long half-lives with respect to the efficiency calibration counting time, source activity may be accurately approximated as constant. Decreases in activity must be taken into account when counting isotopes with relatively short half-lives. Due to the high-energy of many prompt gamma rays, it is difficult to perform absolute efficiency calibrations. Radioactive isotopes with half-lives suitable to be economically used as reference sources typically have maximum decay energies between 1 and 2 MeV. ^{152}Eu is a common source for gamma spectroscopy calibration. ^{182}Ta and ^{133}Ba have also seen use over similar energy ranges, although their half lives are shorter than ^{152}Eu. ^{56}Co has several peaks above 3 MeV, but has a half-life of only 78.8 days.

Experimental techniques have been used to extend efficiency calibrations to higher energies [27,36,69]. They rely on the overlap of prompt gamma spectra with ordinary decay spectra. In Budapest, several absolute efficiency calibrations are performed with decay sources up to the 3.3 MeV limit of ^{56}Co. Relative efficiencies are then calculated for prompt gamma spectra from Ti, Cl, and N, and fit to the absolute efficiency curve developed with the decay sources. The result is an efficiency calibration reported to be accurate to within 1% from 50 keV to 10 MeV [27].

A second experimental method was developed whereby a PGAA spectrum is used to determine an absolute efficiency in conjunction with NAA. A cobalt sample was irradiated to obtain a prompt gamma spectrum, and then moved to another calibrated detector so the induced ^{60}Co activity of the foil could be determined. Using buildup and decay equations, the radiative neutron capture rate during the irradiation can be determined, and an absolute efficiency can be calculated using:

$$\varepsilon_x = \frac{C}{y_x \cdot S}, \qquad \text{1-5}$$

where y_x is the prompt gamma yield, and S is the total number of radiative captures within the sample during the irradiation [36]. A similar technique has been developed at UT where a V foil is irradiated, and the induced ^{52}V activity is allowed to come to equilibrium and used to determine the radiative capture reaction rate simultaneously with prompt gamma acquisition [69]. This technique will be discussed further in Chapter 4.

The drawback of experimental determinations of detector efficiency is that they rely on the accuracy of prompt gamma yields. Prompt gamma yields can only be measured as accurately as efficiencies are known, but to calculate efficiencies at high energies from prompt gamma spectra, yields must be known. Monte Carlo simulations, particularly with MCNP [70], have the possibility of setting up a source with known yields and calculating efficiency over any energy range [71,72,73]. The only limitations are knowledge of the detector geometry and cross section data. Monte Carlo simulations can also be used to model probes [74,75,76], determine interferences [77], and the effects of geometry [78,79,80] and matrix [81].

1.3.5 PGAA Data Libraries

As indicated in the previous section, library data is important to determine detector efficiency. It is also required to make quantitative determinations during sample analysis. The most common prompt gamma library is the Lone library [82], an elemental database of prompt gamma energies and yields. Another source of relative yields from an isotopic standpoint is the Evaluated Nuclear Structure Data Files (ENSDF) [83], a theoretically calculated data set. Periodically, specialized reports regarding the prompt gammas emitted by specific isotopes are published [84]. More recently, a new effort has been made to determine isotope specific prompt gamma information [29]. Another recent compilation of available data can be found in the Atomic Data and Nuclear Data Tables [85]. Generally speaking, prompt gamma ray energies are well known; however, prompt gamma ray yields may vary significantly from library to library. Thus, the uncertainty in yield values can be large.

Other constants relevant to PGAA analysis are energy dependent cross section data and isotopic abundances. Budapest yields have been reported in terms of cross section per prompt gamma, based on library values for abundance and 2200 m/s cross section [86,87]. For a more versatile application, the data can be deconvoluted to proper yields per radiative capture event for each isotope. Publications with measurements of specific cross sections are occasionally available [88]. Additional efforts have been made to improve the photon production libraries in the ENDF files [89], which are used by many nuclear engineering and physics codes.

1.3.6 Common Composite Evaluation Techniques

Many techniques are currently in use to analyze composite materials. The flywheel program at the UT-CEM has employed ultrasonic sounding and x-ray radiography and computed tomography for the NDE of composite flywheels [90]. Destructive analysis techniques include hydroburst testing to measure ultimate hoop strength of composite rings and acid digestion to determine carbon fiber volume [91].

Low frequency ultrasonics have shown promise as a means to identify and characterize small voids and delaminations in composite materials [92], as well as information on mechanical characteristics [93]. The propagation of sound waves through thick, multilayered materials has become the subject of rigorous study [94,95]. Pulse echo methods, where the reflection of an acoustic impulse is recorded to infer internal structure, have been able to detect defects as small as 125×125µm in standard flywheels with manufactured defects. Transmission techniques have successfully detected known defects as small as 250×250µm [90]. Unfortunately, acoustic techniques typically require the submersion of the test object into a fluid to couple sound waves from the transducer into the material, as shown in Figure 1.7. Water absorption is known to weaken epoxy based composite materials [96] and current methods of acoustic evaluation may damage the test samples.

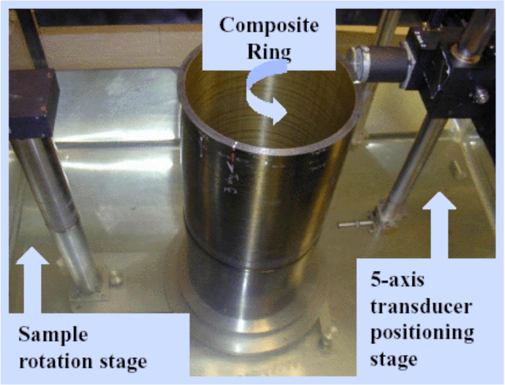

Figure 1.7. Single layer of composite ring undergoing ultrasonic testing.

X-ray radiography is also a common technique for non-destructive evaluation. Having been in use for nearly 100 years, x-ray radiography is a fairly mature science and x-ray machines are readily available. X-ray radiation is attenuated in a material proportional to the material density, and radiographs are essentially shadow images that can show variations in sample density. Modern x-ray techniques have evolved rapidly with the development of faster computers and digital imaging. Multiple frames of an object in different positions can be acquired quickly and reconstructed into a three dimensional image using computed tomography (CT). X-ray radiography has been used to detect prefabricated defects as small as 125×125μm in standard flywheels using conventional radiography and computed tomography [90]. A potential limitation for x-ray radiographic techniques is the low density of polymer matrix carbon fiber composites. Small defects may not provide enough contrast to be detectable using x-rays. The composite material and water are of similar density, making the detection of water with x-rays difficult [97,98].

The strength of polymer-based carbon composites is derived from the fiber content [99]. Accurate determination of fiber volume is critical to predict ultimate material strength. A common technique to determine fiber volume is acid digestion [90,100]. In this process, a sample is weighed, the polymer matrix is dissolved, and the remaining sample is weighed again. The change in mass is used to infer the bulk fiber volume. This technique has been shown to be accurate, but the sample is destroyed in the process. Fiber volume can also be determined on a microscopic level by visual inspection [99]. A sample can be sliced perpendicular to the fiber direction, and the cross section can be examined under microscope. This technique has the added benefit of discrimination between fiber, matrix, and voids. Unfortunately, it is also destructive.

Neutron beam techniques, particularly neutron radiography, have also been used to investigate carbon composite material properties. Neutrons interact with atomic nuclei, not electrons. Potentially, variations in light composite materials may be easier to detect with neutron radiography instead of x-ray radiography [98]. Thermal neutron radiography is commonly used to detect the presence of water in composite aircraft components. In many tests, a sample is radiographed, heated, and radiographed again [97]. If the contrast changes where the material is heated, water is assumed to have been liberated from that area. A change in contrast also indicates the presence of water. Fast neutron radiography has also been used to detect defects in thick composite materials [101]. Neutron radiography has also been used to track water diffusion profiles in epoxy and metals [102].

CHAPTER 2. Experimental Facilities and Setup

2.1 University of Texas Nuclear Engineering Teaching Laboratory

The UT-NETL operates a graphite-reflected 1 MW TRIGA MARK II reactor. The facility has 5 beam ports and several in-core irradiation positions and is used for a variety of neutron beam experiments and nuclear analytical services. A general picture of the reactor core is shown in Figure 2.1. Current beam port utilization is listed in Table 2.1.

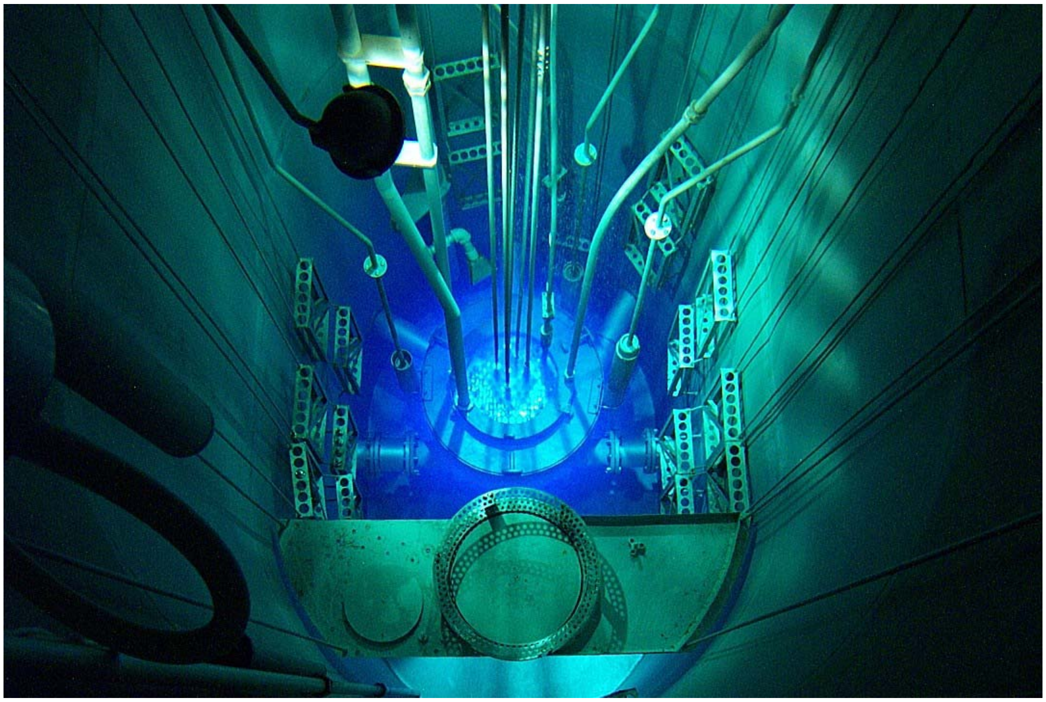

Figure 2.1. The UT-NETL reactor.

Table 2.1. Beam Port Utilization

Beam Port	Experiment
BP#1	Texas Intense Positron Source
BP#2	Neutron Depth Profiling
BP#3	Texas Cold Neutron Source (TCNS)
BP#4	Available for development
BP#5	Thermal Neutron Imaging Facility (TNIF)

In 2000, a flaw in a reflector clad weld that had lead to the flooding of the open volume within the reflector was diagnosed [103]. The additional water shielding has decreased the neutron flux in each beam port, but the experiments described in this dissertation primarily utilized BP#3, where the effects of the reflector conditions are minor [104].

2.2 Texas Cold Neutron Source

The TCNS, depicted in Figure 2.2, was completed in 1995 [105]. The TCNS is a robust cold neutron generator and filter. Neutrons leaking from the core into beam port 3 first enter a cold neutron moderating chamber which uses mesitylene (1,3,5-tri-methyl-benzene, C_9H_{12}) frozen to approximately 30 K to cool neutrons to sub-thermal temperatures. The moderating chamber can also be purged with helium for no cold neutron moderation. After the moderating chamber, the neutron beam encounters a series of neutron guides curved to a 300 m radius [106]. The curved guide takes advantage of the wave-like properties of cold neutrons and preferentially steers them away from the beam centerline. The final guide section is a converging guide [107], which provides a maximum gain of 5.5 [108] at the focal plane 24 cm from the mouth of the guide [109].

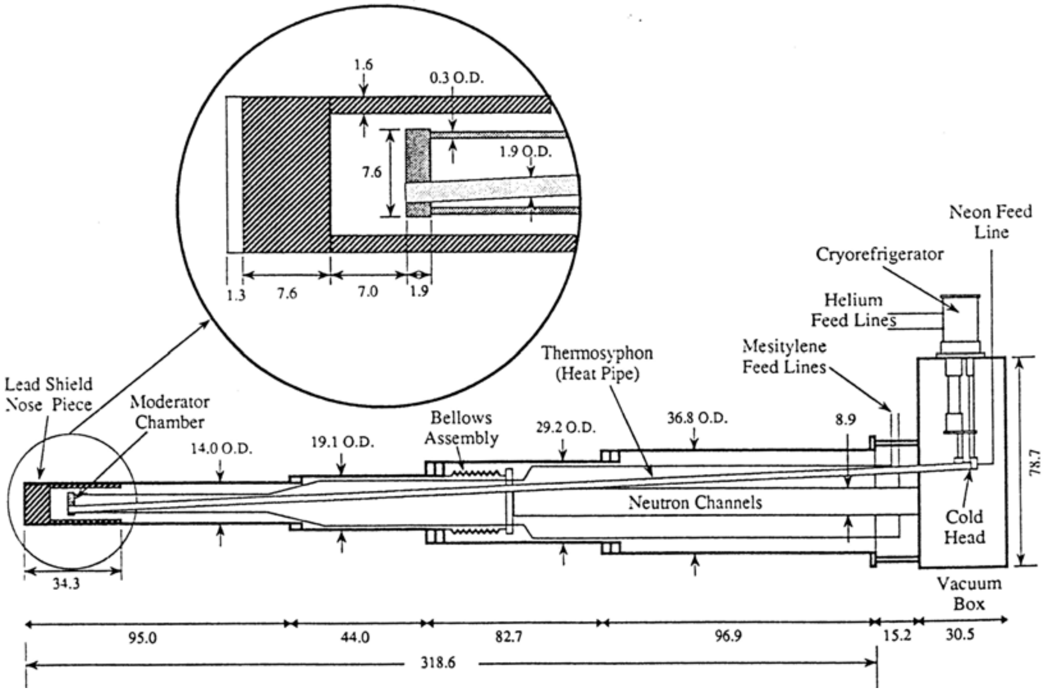

Figure 2.2. The Texas Cold Neutron Source as inserted into BP#3. Units are in cm.

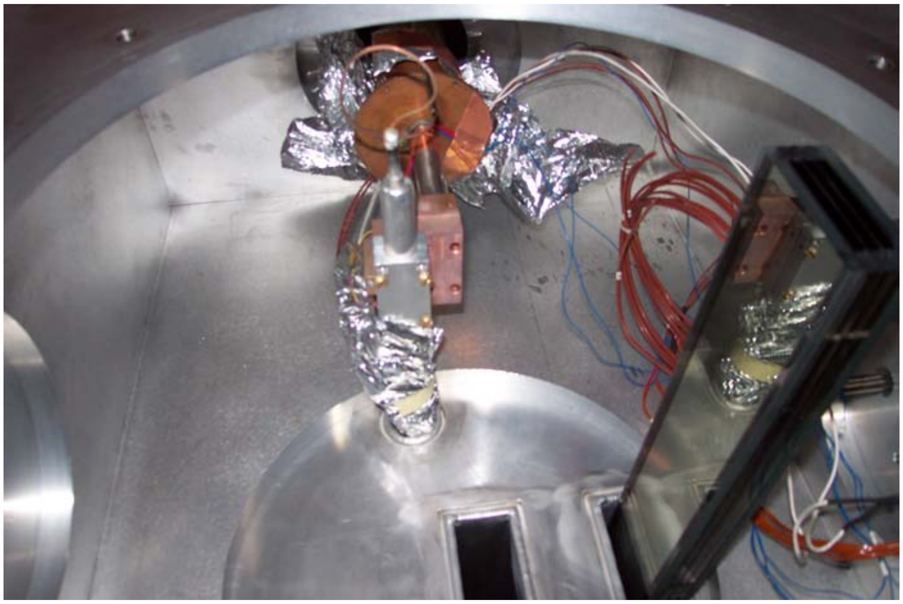

Figure 2.3. Inside of vacuum box at mouth of beam port 3.

Figure 2.4. Curved neutron guide exiting vacuum box and neutron shielding cave.

The moderating chamber is cooled by a neon thermo-siphon fixed to a Cryomech GB04 cryo-refrigerator in a vacuum box mounted to the biological shielding above the beam port opening. The GB04, and associated compressor unit, are capable of removing approximately 9.5 W of heat at 30 K. The system temperature is monitored by 3 thermocouples and a temperature controlled heater. Figure 2.3 shows the inside of the vacuum box. The GB04 cold finger and neon thermo-siphon are visible, as well as a curved neutron guide. Figure 2.4 shows the curved neutron guide leading from the vacuum box through the neutron shielding cave.

The TCNS was designed primarily to operate at or below reactor powers of 500 kW. At 1 MW, heat deposition rates in the moderating chamber exceed the capabilities of the cryo-refrigerator system. Temperatures increase steadily until the neon thermo siphon boils dry and heat removal is lost entirely [110,111,112]. Even temperature transients in the cold neutron moderating chamber are undesirable, as they will inevitably lead to changes in the magnitude and energy spectrum of the neutron flux delivered by the cold neutron guides. To eliminate this variable, the experiments described in this dissertation were performed with no cold moderation.

2.3 Cold Neutron PGAA

The guided beam delivers a thermal equivalent neutron flux of $(1.5 \pm 0.6)\times10^7$ n/cm^2/s to the focal plane with no cold moderation, and $(4.6 \pm 0.7)\times10^7$ n/cm^2/s while the cold moderator is frozen to 26 K [113]. Because there is no line of sight to the reactor, fast neutron and gamma ray background is extremely low. A sample is held in the focal region of the beam using a sample holding device [for example, an array of fluoro-ethylene propylene (FEP) string in an aluminum frame]. An FEP bag designed to fit over the sample stand is available to allow the volume to be purged with helium. A general setup for PGAA acquisition is shown in Figure 2.5. The horizontal sample holder has been installed on the background control base plate, although the FEP bag is not in use. The relationship between the PGAA system and the TCNS is shown in Figure 2.6 and Figure 2.7.

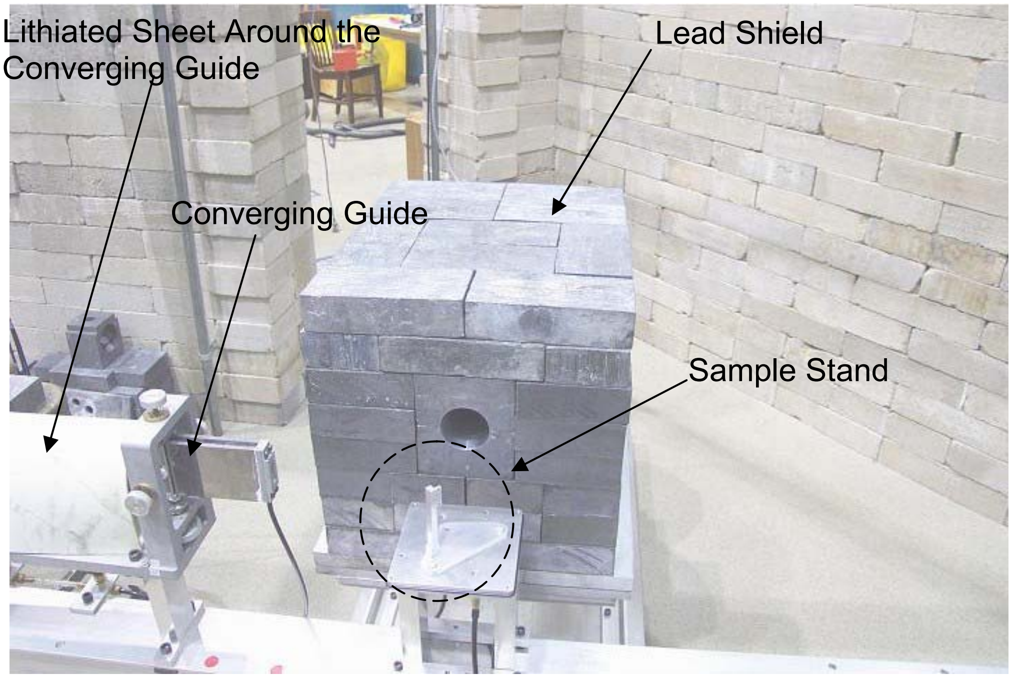

Figure 2.5. Shielded HPGe detector, PGAA sample area, and converging guide.

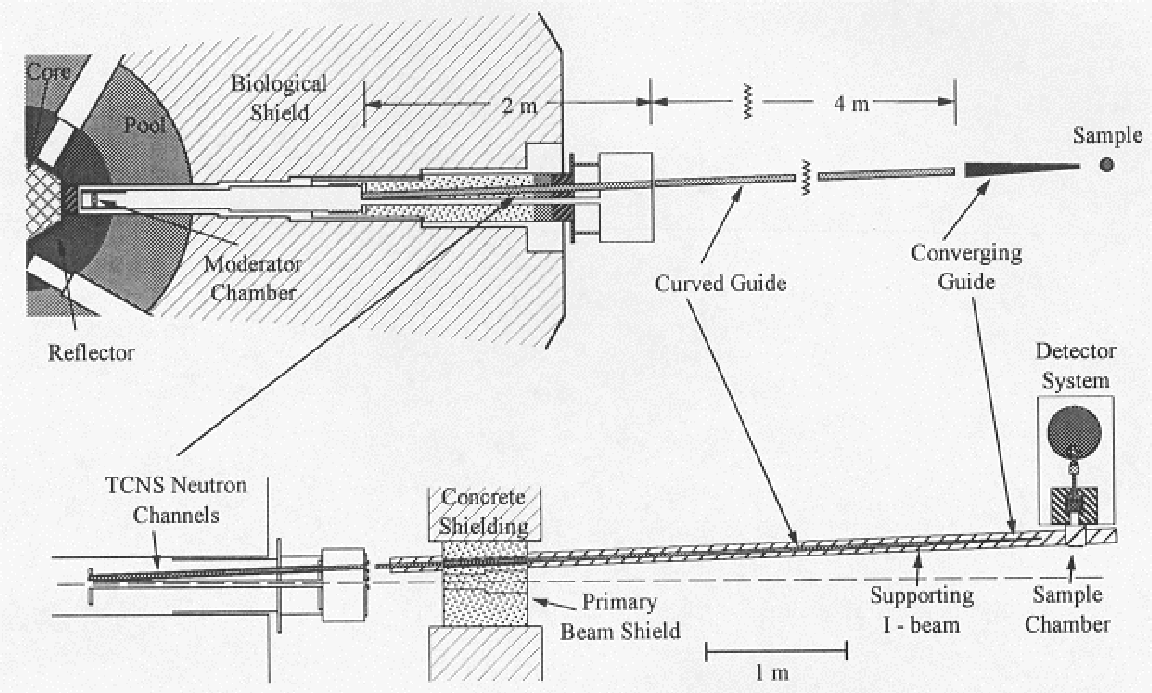

Figure 2.6. Relationship between TCNS and PGAA system.

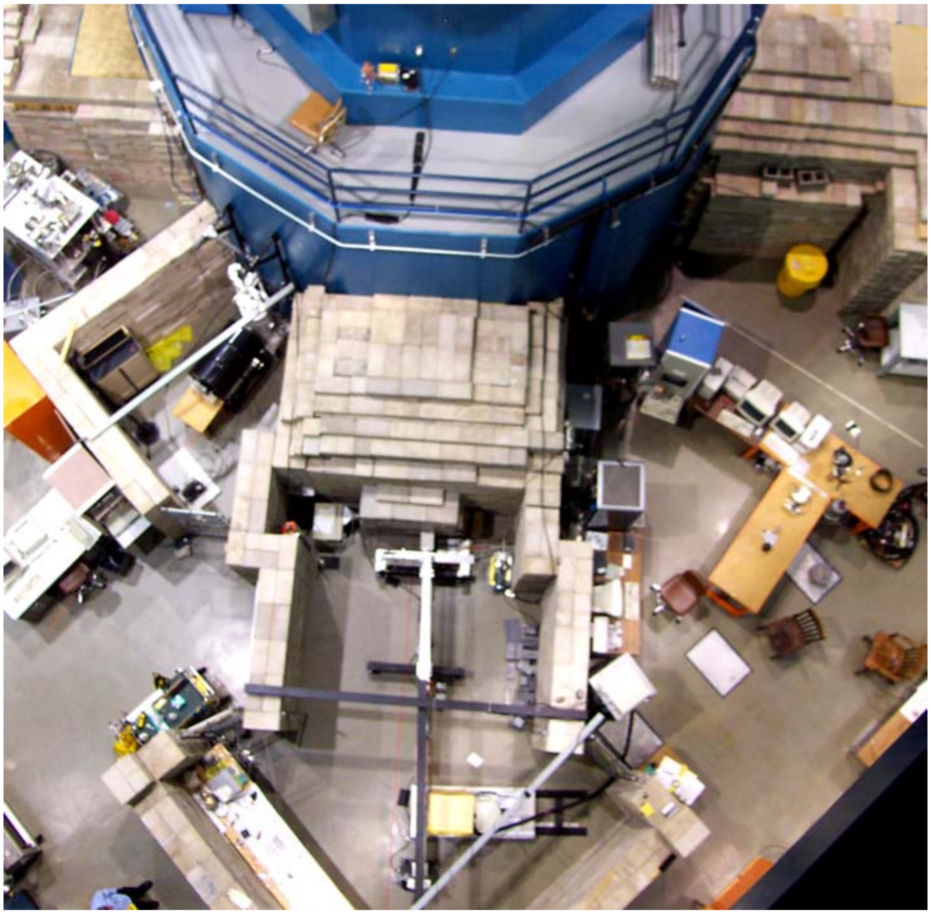

Figure 2.7. Arial photo of beam port three and PGAA facility.

Prompt gamma photons are normally detected with a horizontal, n-type ORTEC GMX Series GAMMA-X HPGe Coaxial Photon Detector System. The detector is 23% efficient at 1.33 MeV and has a 0.5 mm thick Beryllium window facing the PGAA sample. The detector head is shielded by approximately 6 inches of lead on all sides, with a 2" diameter collimation hole for the acquisition of prompt gamma rays. The shielding is stacked on an aluminum stand, which along with the detector dewar is seated on an aluminum trolley that allows the distance between detector and sample to be varied. In the event that the ORTEC detector requires service, a p-type, horizontal Canberra HPGe detector is available.

Data from the HPGe detector is acquired using a Canberra DSA 2000 digital spectroscopy system that has a 16k channel MCA. The DSA 2000 is a single unit which replaces NIM bin electronics typically used with gamma spectroscopy. The DSA 2000 is controlled by the Canberra Genie 2000 v1.4 Gamma Acquisition and Analysis software. The Genie 2000 package is used to control power supply and amplifier settings, acquire spectra, and quantitatively analyze spectra.

CHAPTER 3. PGAA Analysis

The acquisition of prompt gamma spectra is fairly straightforward. Prompt gamma peaks can be readily identified by energy and used to catalog the constituents of a sample; however, quantitative analysis for isotopic concentrations can be difficult. This section outlines several different cases.

All PGAA spectra analysis will begin with the general reaction rate equation,

$$\dot{C}(\vec{r},E_\gamma,E_n,t)=\varepsilon(\vec{r},E_\gamma)N(\vec{r})y(E_\gamma)\sigma_\gamma(E_n)\phi(\vec{r},E_n,t), \qquad 3\text{-}1$$

where $\dot{C}(\vec{r},E_\gamma,E_n,t)$ is the count rate density from position $\vec{r}$, at gamma energy E_γ, due to neutron interactions at energy E_n, at time t; $\varepsilon(\vec{r},E_\gamma)$ is the detection efficiency for gammas at energy E_γ emitted from position $\vec{r}$; $N(\vec{r})$ is the isotopic density of a constituent isotope at position $\vec{r}$; $y(E_\gamma)$ is the prompt gamma emission yield at energy E_γ; $\sigma_\gamma(E_n)$ is the radiative capture reaction cross section at energy E_n, and $\phi(\vec{r},E_n,t)$ is the neutron flux at position $\vec{r}$, neutron energy E_n, and time t. Note that $\vec{r}$ is used as shorthand notation for a position (x,y,z).

The spectroscopy equipment in use records data as counts per channel, calibrated to counts per energy window. Equation 3-1 shows that measured spectra will be influenced by the neutron energy, temporal and spatial variations in the neutron beam, and spatial variations in the detection efficiency for gammas across a wide photon energy range. These dependencies will be affected by the beam-sample-detector geometry, and may be significantly altered by the constituents of the sample. Proper analysis, as well as experimental control, is necessary to make rigorous quantitative determinations.

3.1 Point Sample

We will begin with the analysis of the simplest sample: a point. Point samples, or very small samples that approximate a point, are easy to evaluate and useful as a diagnostic tool. Since they are very small, energy and efficiency calibrations using a point source are very accurate. Also, as sample size decreases, attenuation of the neutron beam and emitted prompt gammas through the sample itself becomes negligible.

The analysis of a point sample begins with equation 3-1. The measured spectrum is the time integral of the experiment, so we will begin by introducing the total neutron fluence, $\Phi(\vec{r},E_n)$, defined in equation 3-2 as

$$\Phi(\vec{r},E_n)=\int_0^t \phi(\vec{r},E_n,t')dt' . \qquad 3\text{-}2$$

Integrating equation 3-1 over the irradiation time yields equation 3-3,

$$C(\vec{r},E_\gamma,E_n)=\varepsilon(\vec{r},E_\gamma)N(\vec{r})y(E_\gamma)\sigma_\gamma(E_n)\Phi(\vec{r},E_n), \qquad 3\text{-}3$$

which represents the total number of counts from any location in the sample, instead of a count rate. The next step will be to integrate over the sample dimensions and calculate the total number of counts from the sample, which is the measured value. The integral could be for any geometry.

$$\int_V C(\vec{r},E_\gamma,E_n)d\vec{r}=\int_V \varepsilon(\vec{r},E_\gamma)N(\vec{r})y(E_\gamma)\sigma_\gamma(E_n)\Phi(\vec{r},E_n)d\vec{r}$$

If the sample is sufficiently small, the efficiency will be constant throughout the sample volume. Furthermore, if the sample is optically thin in all dimensions, the fluence through the sample will be constant and can be factored out of the integral as well. Also, it is generally assumed that the atomic densities throughout the sample are uniform and don't vary with position (i.e. the sample is homogeneous). Thus, we acquire,

$$\int_V C(\vec{r}, E_\gamma, E_n) d\vec{r} = y(E_\gamma)\varepsilon(E_\gamma)\sigma_\gamma(E_n) N\Phi(E_n)\int_V d\vec{r} \; .$$

We are left with equation 3-4, where *c* is the total number of counts and *V* is volume,

$$c(E_\gamma, E_n) = y(E_\gamma)\varepsilon(E_\gamma)\sigma_\gamma(E_n) N\Phi(E_n) V \; . \qquad \text{3-4}$$

To remove the neutron energy dependency, equation 3-4 must be integrated over all neutron energies,

$$\int_0^\infty c(E_\gamma, E_n) dE_n = V y(E_\gamma)\varepsilon(E_\gamma) N \int_0^\infty \sigma_\gamma(E_n)\Phi(E_n) dE_n \; .$$

At this point we can take advantage of the fact that the neutron beam is composed of cold neutrons and the 1/v nature of the neutron radiative capture cross section below resonance regions (Recall the radiative capture cross sections for ^{1}H and ^{12}C shown in Figure 1.5). The cross section as a function of neutron energy will be proportional to a reference energy, as shown in equation 3-5,

$$\sigma_\gamma(E) = \sigma_{\gamma 0}\sqrt{\frac{E_0}{E}} \; . \qquad \text{3-5}$$

Substituting equation 3-5 into the integral yields equation 3-6,

$$c(E_\gamma) = Vy(E_\gamma)\varepsilon(E_\gamma)N\sigma_{\gamma 0}\sqrt{E_{n0}}\int_0^\infty \frac{\Phi(E_n)}{\sqrt{E_n}}dE_n \qquad 3\text{-}6$$

Unfortunately, the energy spectrum of the neutron fluence has not been determined as of this writing, and the integral cannot be explicitly solved. It is a common practice to report cold neutron flux values in terms of a thermal equivalent flux, or a 2200 m/s flux. We will calculate the 2200 m/s equivalent fluence using equation 3-7 and the 2200 m/s radiative capture cross section,

$$\sigma_{\gamma 2200}\Phi_{2200_{EQ}} = \int_0^\infty \sigma_\gamma(E_n)\Phi(\vec{r}, E_n)dE_n$$

$$\sigma_{\gamma 2200}\Phi_{2200_{EQ}} = \int_0^\infty \sigma_{\gamma 2200}\sqrt{\frac{E_{n2200}}{E}}\Phi(\vec{r}, E_n)dE_n$$

$$\Phi_{2200_{EQ}} = \sqrt{E_{n2200}}\int_0^\infty \frac{\Phi(E_n)}{\sqrt{E_n}}dE_n \, . \qquad 3\text{-}7$$

By substituting 3-7 into 3-6, we obtain an expression for the measured gamma spectrum peak area as a function of sample volume, gamma yield, detection efficiency, and the 2200 m/s cross section and equivalent flux, as described in equation 3-8,

$$c(E_\gamma) = Vy(E_\gamma)\varepsilon(E_\gamma)N\sigma_{\gamma 2200}\Phi_{2200EQ} \qquad 3\text{-}8$$

If the 2200 m/s equivalent fluence is known, the isotopic density, N, of the prompt gamma emitting isotope in the sample can be determined. Conversely, if a known sample is used, the 2200 m/s equivalent flux can be determined.

3.2 Attenuating Point Sample

In theory, equation 3-8 can be used to either determine the 2200 m/s equivalent flux, or to determine the number density of a particular isotope within a sample. The only requirements are that the neutron fluence is constant within the sample (i.e. no attenuation of the beam), and the sample is small enough to be approximated as a point source of radiation. Unfortunately, small sample size and low neutron absorption rates lead to low count rates, and extended irradiation times. In practice, it is better to use a small sample that is a strong neutron absorber. Neutron attenuation within the sample must be accounted for by modifying the integral of equation 3-3 to account for a spatial variation in the neutron fluence. We will consider a rectangular foil and use Cartesian coordinates. The sample will be assumed to be sufficiently small that fluence varies only due to linear attenuation within the sample, as indicated in equation 3-9,

$$c(E_\gamma) = y(E_\gamma)\varepsilon(E_\gamma)\sigma_{\gamma 2200} N \int_0^a dx \int_0^b dy \int_0^d \Phi_{2200EQ}(z)\,dz\,. \qquad \text{3-9}$$

For now, we'll continue to work with the 2200 m/s equivalent fluence. Assuming the sample is a pure (n,γ) absorber, the neutron fluence will be attenuated exponentially through the foil according to equation 3-10,

$$c(E_\gamma) = y(E_\gamma)\varepsilon(E_\gamma)\sigma_{\gamma 2200} N \int_0^a dx \int_0^b dy \int_0^d \Phi_{02200EQ} e^{-\sigma_{\gamma 2200} N z}\,dz\,, \qquad \text{3-10}$$

where $\Phi_{02200EQ}$ is the 2200 m/s equivalent fluence delivered to the surface of the sample. The integral can be solved to find equation 3-11,

$$c(E_\gamma) = a \cdot b \cdot y(E_\gamma)\varepsilon(E_\gamma)\Phi_{02200EQ}\left[1 - e^{-\sigma_{\gamma 2200} \cdot N \cdot d}\right]. \qquad \text{3-11}$$

Equation 3-11 can also be rearranged to solve for the 2200 m/s equivalent fluence that was delivered to the sample during the irradiation,

$$\Phi_{0\,2200\,EQ} = \frac{c(E_\gamma)}{a\cdot b\cdot y(E_\gamma)\varepsilon(E_\gamma)\left[1-e^{-\sigma_{\gamma 2200}\cdot N\cdot d}\right]}. \tag{3-12}$$

The analysis of an attenuating sample can also be performed without assuming a simplified 2200 m/s equivalent fluence, starting with equation 3-13,

$$c(E_\gamma, E_n) = y(E_\gamma)\varepsilon(E_\gamma)\sigma_\gamma(E_n) N \int_0^a dx \int_0^b dy \int_0^d \Phi_0(E_n) e^{-\sigma_\gamma(E_n)Nz} dz\ . \tag{3-13}$$

After solving the spatial integral, equation 3-13 becomes

$$c(E_\gamma, E_n) = a\cdot b\cdot y(E_\gamma)\varepsilon(E_\gamma)\Phi_0(E_n)\left[1-e^{-\sigma_\gamma(E_n)\cdot N\cdot d}\right],$$

which must be integrated over neutron energy to obtain equations 3-14 and 3-15.

$$\int_0^\infty c(E_\gamma, E_n) dE_n = a\cdot b\cdot y(E_\gamma)\varepsilon(E_\gamma)\int_0^\infty \Phi_0(E_n)\left(1-e^{-\sigma_\gamma(E_n)\cdot N\cdot d}\right) dE_n$$

$$c(E_\gamma) = a\cdot b\cdot y(E_\gamma)\varepsilon(E_\gamma)\int_0^\infty \Phi_0(E_n)\left(1-e^{-\sigma_{\gamma 0}\sqrt{\frac{E_0}{E_n}}\cdot N\cdot d}\right) dE_n \tag{3-14}$$

$$c(E_\gamma) = a\cdot b\cdot y(E_\gamma)\varepsilon(E_\gamma)\left(\int_0^\infty \Phi_0(E_n) dE_n - \int_0^\infty \Phi_0(E_n) e^{-\sigma_{\gamma 0}\sqrt{\frac{E_0}{E_n}}\cdot N\cdot d} dE_n\right) \tag{3-15}$$

We are still left in a situation where these equations cannot be solved without knowledge of the neutron energy spectrum; however, the only unknown in equations 3-14 and 3-15 is the function $\Phi_0(E_n)$. All other terms can be measured or found in the literature for any known sample. Equation 3-15 could be rewritten as

$$c(E_\gamma) = F(E_\gamma)\left(\int_0^\infty \Phi_0(E_n)dE_n - \int_0^\infty \Phi_0(E_n)e^{-\frac{G(N,d)}{\sqrt{E_n}}}dE_n\right), \qquad \text{3-16}$$

where *F* is a constant for any particular gamma, and the value of *G* can be calculated using ENDF cross section data at any energy. *G* can be varied by using samples of different thickness and/or different material. By doing so, the $\Phi_0(E_n)$ function could be unfolded. The equation 3-16 implies a method for determining the energy spectrum of any cold neutron beam. The only requirement is that test samples have a low scattering power. The ideal samples would be pure absorbers.

3.3 Planar Sample

The irradiation and analysis of a known point sample can be used to measure the magnitude, energy spectrum, and spatial variation of the delivered neutron fluence. When these factors are known, the analysis of the spectrum of an unknown point sample can yield isotopic concentrations within the sample. Unfortunately, the composite coupons used in this investigation cannot be accurately approximated as point samples. In fact, many samples are not even the same size or geometry. Proper analysis will require quantitative knowledge of the spatial variation in the neutron fluence.

The analysis will begin with a modified version of equation 3-9,

$$c(E_\gamma, E_n) = y(E_\gamma)\int_V \varepsilon(\vec{r}, E_\gamma)N(\vec{r})\sigma_\gamma(E_n)\Phi(\vec{r}, E_n)dxdydz\,. \qquad \text{3-17}$$

Since detection efficiency will vary with position, it must remain inside the volume integral. If the spatial variation of the fluence, number density, and efficiency are known, equation 3-17 can be integrated. Typically the efficiency and flux are measured values, and the number density is an unknown. It will be useful to discretize equation 3-17 into a summation over many sample volume units, as shown in equation 3-18,

$$c(E_\gamma, E_n) = y(E_\gamma) \sum_{i=1}^{I} \varepsilon_i(E_\gamma) N_i \sigma_\gamma(E_n) \Phi_i(E_n) \Delta V_i \, . \qquad \text{3-18}$$

Equation 3-18 assumes that the neutron fluence is constant throughout the i^{th} volume. The validity of this assumption will depend on the optical thickness of the sample, which is largely unknown. We can further assume that the number density in each volume unit is constant throughout the sample ($N_i = N$), allowing for equation 3-19,

$$c(E_\gamma, E_n) = y(E_\gamma) N \sum_{i=1}^{I} \varepsilon_i(E_\gamma) \sigma_\gamma(E_n) \Phi_i(E_n) \Delta V_i \, . \qquad \text{3-19}$$

The only step that remains is to integrate over neutron energy, which can be accomplished in the same manner as for the previous samples by assuming a 1/v absorber,

$$c(E_\gamma) = y(E_\gamma) N \left[\sum_{i=1}^{I} \Delta V_i \varepsilon_i(E_\gamma) \int_0^\infty \sigma_\gamma(E_n) \Phi_i(E_n) dE_n \right],$$

$$c(E_\gamma) = y(E_\gamma) N \left[\sum_{i=1}^{I} \Delta V_i \varepsilon_i(E_\gamma) \sigma_{\gamma 0} \sqrt{E_{n0}} \int_0^\infty \frac{\Phi_i(E_n)}{\sqrt{E_n}} dE_n \right], \qquad \text{3-20}$$

Equation 3-20 is not directly solvable without knowledge of the neutron energy spectrum. If it has not been determined, a 2200 m/s equivalent fluence can be inserted to obtain

$$c(E_\gamma) = y(E_\gamma) N \left[\sum_{i=1}^{I} \Delta V_i \varepsilon_i (E_\gamma) \sigma_{\gamma 2200} \Phi_{i2200_{EQ}} \right]. \qquad 3\text{-}21$$

A flux map is required to determine the flux delivered to each differential volume. It is possible to measure the spatial variation of the neutron flux across a sample by acquiring spectra with a known point sample in various positions. The flux delivered to the i^{th} channel could be determined by

$$\Phi_{i2200_{EQ}} = \frac{c_i(E_\gamma)}{a \cdot b \cdot y(E_\gamma) \varepsilon(E_\gamma) \left[1 - e^{-\sigma_{\gamma 2200} \cdot N \cdot c}\right]}, \qquad 3\text{-}22$$

and substituted back into equation 3-21. Such a scheme would require that the time variations in the neutron fluence be accounted for, as well as differences in irradiation time.

The application of a flux mapping scheme to a planar sample requires the use of a point sample that is a weak scatterer. In practice, the sample must also be a strong absorber in order to accomplish the experimental measurements with reasonable accuracy in short time periods. This method is only limited by the properties of the planar sample matrix. Significant neutron buildup, scattering, or attenuation within the planar sample will negate the constant flux assumption, although estimates of these effects could be measured by mapping the fluence that is transmitted through the sample.

3.5 Matrix Effects

The most significant issue for the analysis of prompt gamma spectra of large samples is knowledge of where neutrons have gone in the sample. The flux distribution will determine the spatial distribution of capture gamma reaction rates, and the spatially weighted average efficiency. Although spatially dependent efficiencies can be minimized with small sample size, the effects of scattering and attenuation within even small samples can be significant. Of particular concern is the effect of hydrogen and shifting energy spectra with cold neutrons.

Several researchers have attempted to model the effects of scattering within different matrices [80,81,114]. More sophisticated investigations have taken place using a variation of the Monte Carlo Library Least Squares (MCLLS) approach, a common technique used for the analysis of energy-dispersive X-ray fluorescence (EDXRF) spectra. The MCLLS technique uses Monte Carlo simulations to determine a material composition matching the measured spectra. It eliminates the need to use empirical formulas or fundamental mathematical models to account for matrix effects [115]. An initial guess of sample constituents is required, but that can usually be obtained from the measured spectra. MCLLS techniques have been applied to PGAA for several applications, including the analysis of bulk coal on simulated conveyor belts and the analysis of vitrified waste [116]. Iterations have been performed with MCNP, and the modified Monte Carlo program CEARPGA, which is based on the EDXRF simulation program CEARXRF [117]. MCLLS methods have also been applied to the analysis of green liquor, although PGAA techniques were ultimately deemed unsuitable for that study [67].

3.4 Relative Analysis by Ratio

Matrix effects can be ignored within an individual sample when comparing relative abundances of isotopes within that sample. Consider equation 3-6 for the simple point case in ratio with itself for two different isotopes in one sample, using data from the same irradiation,

$$\frac{c_1\left(E_{\gamma 1}\right)}{c_2\left(E_{\gamma 2}\right)}=\frac{Vy_1\left(E_{\gamma 1}\right)\varepsilon\left(E_{\gamma 1}\right)N_1\sigma_{\gamma 01}\sqrt{E_{n0}}\int_0^{\infty}\frac{\Phi\left(E_n\right)}{\sqrt{E_n}}dE_n}{Vy_2\left(E_{\gamma 2}\right)\varepsilon\left(E_{\gamma 2}\right)N_2\sigma_{\gamma 02}\sqrt{E_{n0}}\int_0^{\infty}\frac{\Phi\left(E_n\right)}{\sqrt{E_n}}dE_n}\,. \qquad 3\text{-}23$$

Since the numerator and denominator describe the same sample, the flux and volume terms will cancel, leaving

$$\frac{c_1\left(E_{\gamma 1}\right)}{c_2\left(E_{\gamma 2}\right)}=\frac{y_1\left(E_{\gamma 1}\right)\varepsilon\left(E_{\gamma 1}\right)N_1\sigma_{\gamma 01}}{y_2\left(E_{\gamma 2}\right)\varepsilon\left(E_{\gamma 2}\right)N_2\sigma_{\gamma 02}}\,,$$

which can be rearranged to determine the isotopic ratios within the sample,

$$\frac{N_1}{N_2}=\frac{c_1\left(E_{\gamma 1}\right)y_2\left(E_{\gamma 2}\right)\varepsilon\left(E_{\gamma 2}\right)\sigma_{\gamma 02}}{c_2\left(E_{\gamma 2}\right)y_1\left(E_{\gamma 1}\right)\varepsilon\left(E_{\gamma 1}\right)\sigma_{\gamma 01}}\,. \qquad 3\text{-}24$$

If the flux can be monitored from irradiation to irradiation, or is known to be invariant, and a known comparator can be obtained with a similar sample matrix, quantitative determinations can be made using two separate irradiations and a variant of equation 3-24,

$$N_1=N_c\frac{c_1\left(E_{\gamma 1}\right)y_c\left(E_{\gamma c}\right)\varepsilon\left(E_{\gamma c}\right)\sigma_{\gamma 0c}}{c_c\left(E_{\gamma c}\right)y_1\left(E_{\gamma 1}\right)\varepsilon\left(E_{\gamma 1}\right)\sigma_{\gamma 01}}f\,, \qquad 3\text{-}25$$

where *f* is a correction factor for differences in sample volume and delivered integrated fluence. The subscript *c* indicates a controlled standard. If the selected standard contains the same isotope as the unknown sample, equation 3-25 can be reduced further to

$$N_1 = N_c \frac{c_1}{c_c} f \, . \tag{3-26}$$

This is the basis of the k_0 approach, a technique whereby ratios are taken to remove unknown terms or those with large errors. k_0 factors are typically calculated as

$$k_c(x) = \frac{C_x m_x / t_x}{C_c m_c / t_c} = \frac{y_x \sigma_{\gamma 0x} / M_x}{y_c \sigma_{\gamma 0c} / M_c} \frac{\varepsilon\left(E_{\gamma_x}\right)}{\varepsilon\left(E_{\gamma_c}\right)} \text{ [118],} \tag{3-27}$$

where m_x is the mass of isotope x within the sample and M_x is atomic weight. The subscript c again denotes the controlled standard. Equation 3-27 can be applied to obtain isotopic masses within a sample according to

$$m_x = k_c(x) \frac{C_c t_x}{C_x t_c} m_c \, . \tag{3-28}$$

The k_0 method is a common technique to minimize errors during the analysis of NAA spectra [119]. The measurement and application of PGAA k_0 factors for a variety of samples and standards is of great interest to the prompt gamma community [7,118,120,121,122].

CHAPTER 4. Characterization Experiments

Experiments have been performed to gauge the capabilities of the UT PGAA system to make accurate determinations about carbon fiber composite coupons. In particular, tests were performed to measure or verify the following:

1. Reproducibility of PGAA measurements and the minimization of background radiation and interferences.
2. Uniformity of isotopic constituents of cured composite samples from multiple batches.
3. Use of a ^{3}He detector as a neutron flux monitor.
4. The 2200 m/s equivalent flux delivered by the TCNS.
5. New techniques for high energy efficiency calibrations.
6. Quantitative determination of spatial variations in the neutron flux.

4.1 Reproducibility

4.1.1 Sample Positioning

As built, the UT-PGAA system held samples suspended by FEP strings woven through an aluminum frame. This positioning system has a very low contribution to background, but is not suitable for reproducible sample positioning. The UT-PGAA facility uses a focused cold neutron beam with a well defined focal region. To maximize the radiative capture reaction rate, any sample positioning system should be able to reliably hold a sample in the focal volume of the converging neutron beam. Neutron beam intensity drops off rapidly away from the focal volume, so reproducible positioning is required when analyzing different samples where internal comparators cannot be used to remove exposure variations.

Several new sample holders were designed to securely hold a composite coupon with minimal PGAA spectral interference. Composite coupons from a given batch were generally of the same width and thickness, but length varied from sample to sample. To account for these differences, the sample holders were designed so that the coupons would completely traverse the beam in a given direction, as shown in Figure 4.1, and small variations in length would not affect the volume of the sample within the beam. The actual sample holder components remain outside the neutron beam.

Three sample holders were fabricated, and schematics are shown in Appendix D. The initial design held the sample horizontally through the beam. To allow for samples of varying thickness, a clasp mimicking the function of the chuck that holds the cutting tool on a machinists lathe was designed to clamp the sample in place, as depicted in Figure 4.2. The horizontal sample holder fits onto the pre-existing mounts on the background control base plate (described in Chapter 2). Subsequent MCNP calculations indicated chambers to control the background due to air actually increased the amount of spectral interference, by replacing the background from air with that of the chamber walls. Further, it was determined that by removing the base plate from the PGAA sample stand, interference from ^{27}Al radiative capture gammas could be reduced.

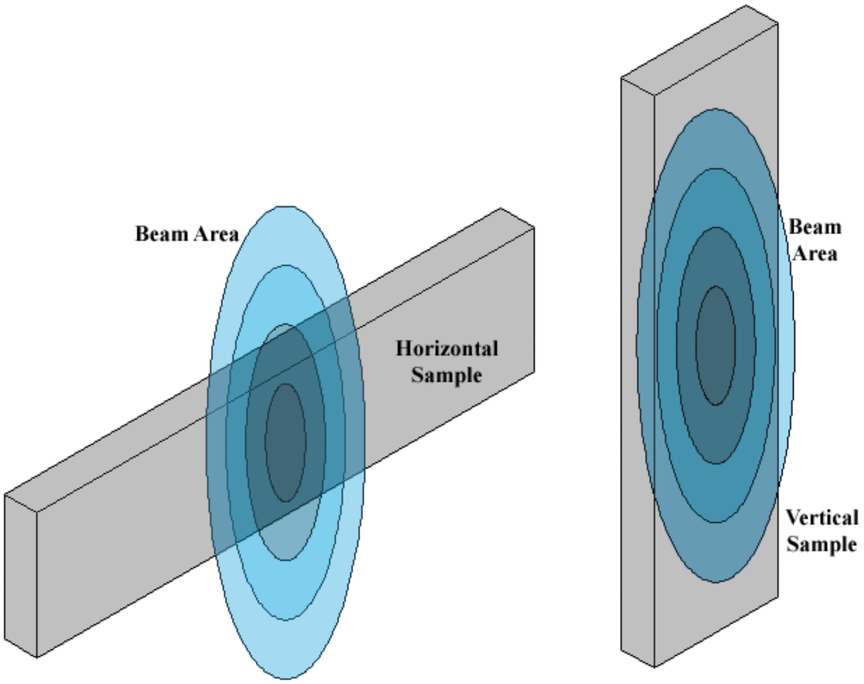

Figure 4.1. Depiction of horizontal and vertical samples in beam of non-uniform intensity.

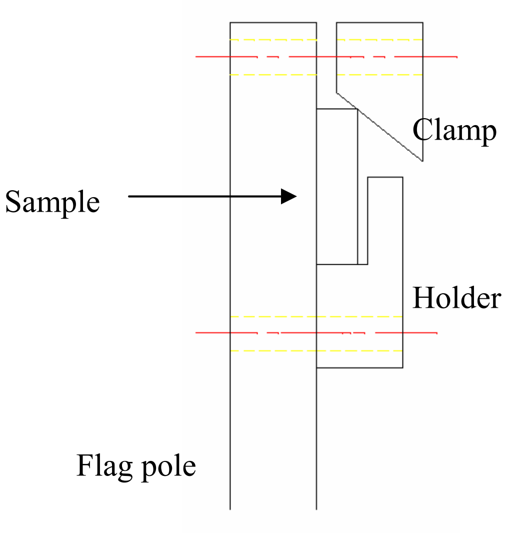

Figure 4.2. Cross sectional view of sample in flag geometry sample holder.

Initial experiments were performed with the horizontal sample holder, partially due to the fact that the coupons used in early experiments were too short to traverse the beam vertically. Later experiments required better counting statistics, however, and steps were taken to improve the radiative capture rate within the sample. Coupons were cut to longer lengths, allowing for the use of vertical sample holder. The new sample holder was designed based on previous MCNP results, and components were fabricated to mount on one of the aluminum support columns instead of the base plate.

The first several sets of test coupons obtained from the UT-CEM were curved samples cut from hydroburst rings. Sample holders were designed as such to hold curved samples. A final set of flat panel coupons were eventually obtained, and a vertical sample holder specifically for these samples was fabricated.

4.1.2 Reproducibility and Shield Optimization

Experiments to verify the reproducibility of PGAA measurements were performed concurrently with shielding optimization experiments. A series of five four-hour irradiations were performed on a single sample fabricated from YLA, Inc. materials in the horizontal sample holder. A precise elemental analysis was not available for the proprietary materials, but a general breakdown of the elemental components is shown in Table 4.1. The summed 20 hour PGAA spectrum for these measurements is shown in Figure 4.3 and several composite and interference peaks have been identified. The acquired prompt gamma spectra for the five irradiations are shown in Figure 4.4, Figure 4.5, and Figure 4.6.

It should be noted that the ^{10}B peak shown in Figure 4.6 is not a true prompt gamma ray peak. It is a result of the $^{10}B(n,\alpha)^{7}Li^{*}$ reaction. The $^{7}Li^{*}$ recoil nucleus is produced in an excited state, which promptly decays at 478 keV. This prompt gamma appears as a "hump" instead of a sharp peak due to Doppler broadening as a result of the kinetic energy and velocity vector of the recoil $^{7}Li^{*}$ nucleus. Throughout this dissertation, the broadened 478 keV peak will be described as a ^{10}B prompt gamma for simplicity.

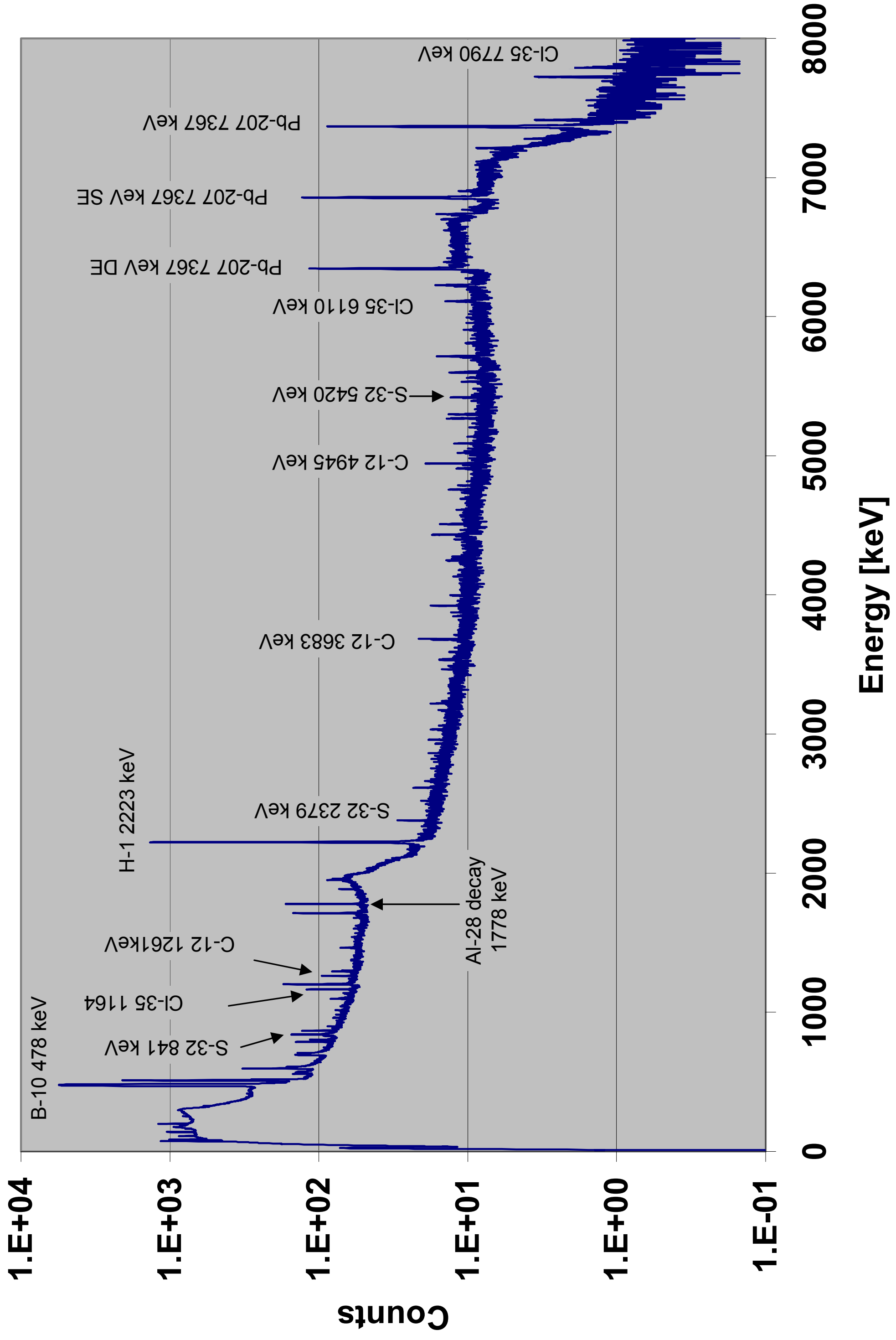

Figure 4.3. Measured PGAA spectrum for composite coupon.

Gamma shielding, in the form of a Pb stack, remained constant through each irradiation. Neutron shielding, however, went through 3 evolutions. For irradiations 1 and 2, the Pb stack was covered with borated polyurethane, with a hole providing line of sight from the detector to the sample. For irradiation 3, additional borated polyurethane was placed around the Pb stack, and a lithiated polymer was placed around the converging guide. Before irradiation 4, a lithiated polymer window was placed between the borated polyurethane and the lead shielding, covering the collimation hole and shielding the detector from scattered neutrons. The addition of neutron shielding to the lead gamma ray shielding is shown in Figure 4.7 (note the contrast with Figure 2.5)

The presence of ^{10}B, ^{12}C, ^{35}Cl, ^{1}H, and ^{32}S are confirmed by PGAA spectra. Oxygen has a very small radiative capture (n,γ) cross section of 0.28 mb and the detection of even large quantities is difficult with short irradiations. Nitrogen also has a small radiative capture (n,γ) cross section, 1.91 b. The presence of nitrogen is only evident if the 5 spectra are combined, indicating a small concentration in the epoxy.

Table 4.1. YLA Composite Constituents (RS36T)

Ingredient	Approximate Percentage	Elements Present
Epoxy Resin	70%	C, H, O, N
Thermoplastic Resin	5%	C, H, S, O
Aromatic Amine	25%	C, H, N, S
Lewis Acid	0.1%	BCl_3
Known Impurities	Trace	Na

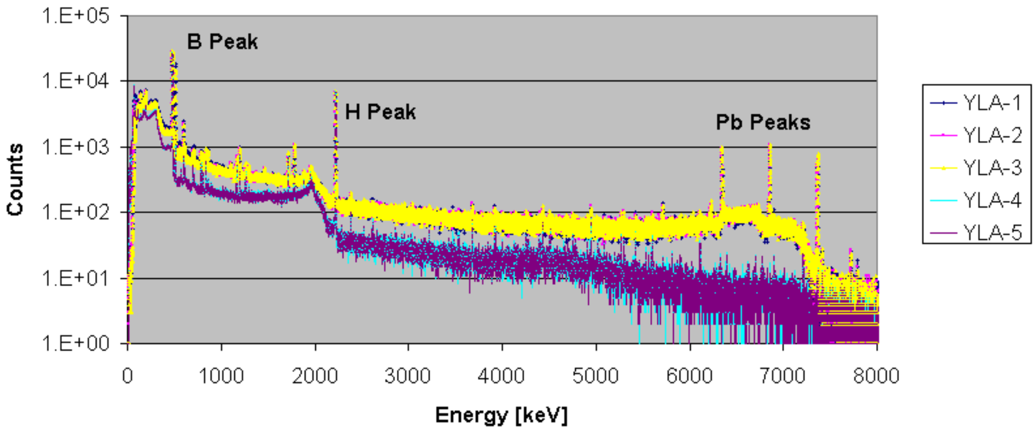

Figure 4.4. Full PGAA spectra acquired for 5 irradiations.

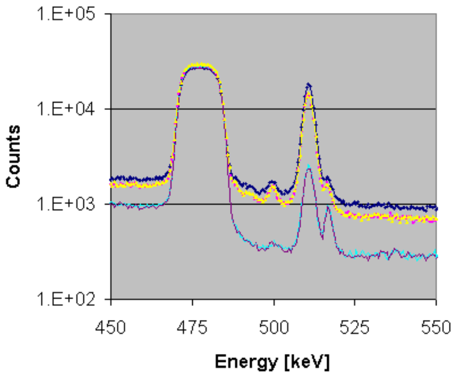

Figure 4.5. Boron peak for each irradiation.

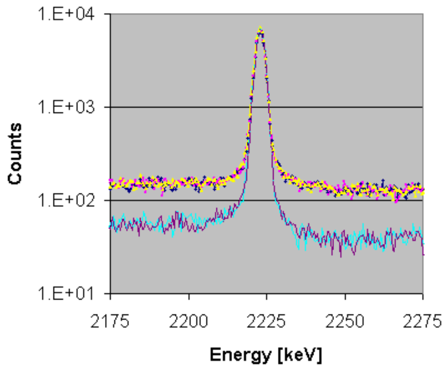

Figure 4.6. Hyrodgen Peak for each irradiation.

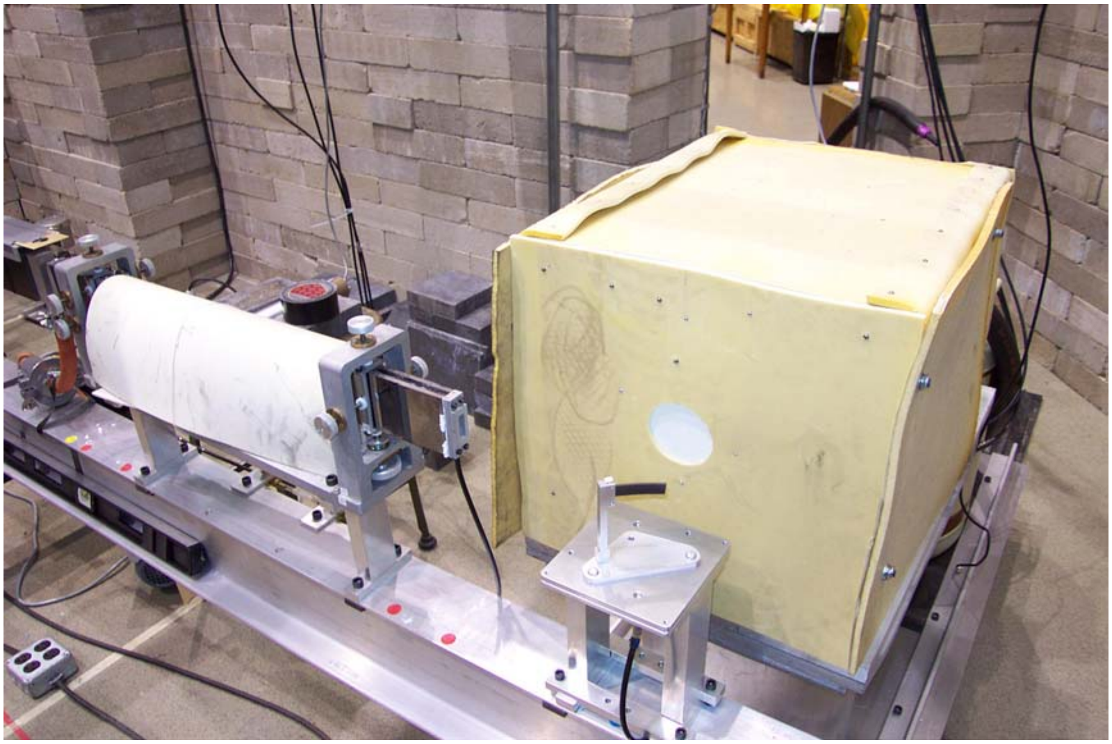

Figure 4.7. PGAA spectrometer after addition of neutron shielding.

Consider a simplified version of equation 3-1,

$$\dot{C}_{ix} = \varepsilon_x N_i y_{ix} \sigma_\gamma \phi \,, \qquad 4\text{-}1$$

where $\dot{C}_{ix}$ is the measured count rate of gammas at energy *x* of isotope *i*, ε_x is the detection efficiency at energy *x*, y_{ix} is the yield for isotope *i* at energy *x*, σ_γ is the radiative capture cross section, and ϕ is the neutron flux. The neutron radiative capture rate, $\dot{A}_{ix}$, is defined as

$$\dot{A}_{ix} = N_i \sigma_\gamma \phi \,. \qquad 4\text{-}2$$

The acquired spectra were used to compute the neutron absorption rate for each isotope using

$$\dot{A}_{ix} = \frac{\dot{C}_{ix}}{\varepsilon_x y_{ix}}. \tag{4-3}$$

^{12}C, ^{35}Cl, and ^{32}S emit multiple prompt gamma rays, and weighted averages were taken to determine the average radiative capture rate. Measured absorption rates are shown in Figure 4.8, and indicate reasonable reproducibility. Some variation is expected due to changes in the integrated neutron current during different irradiations.

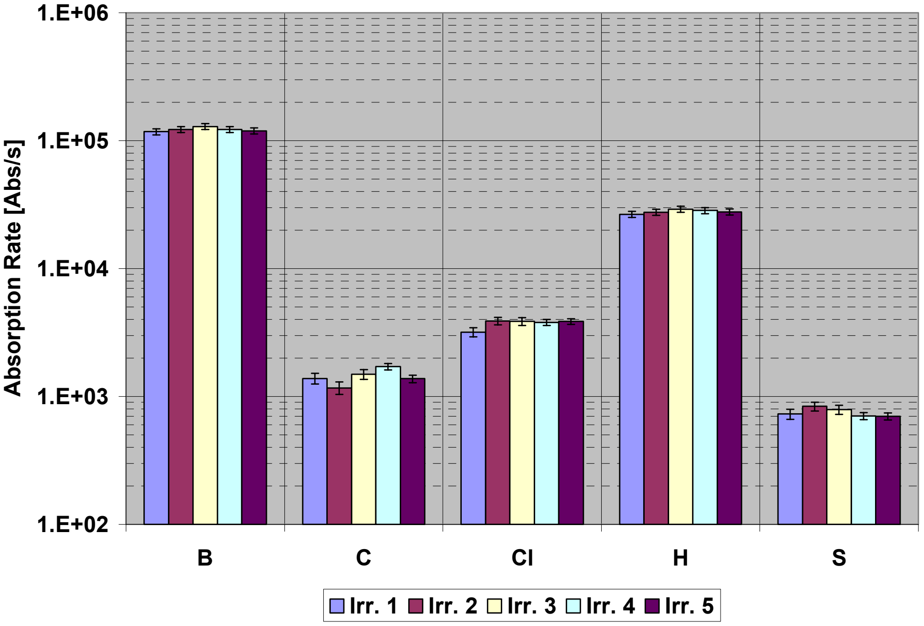

Figure 4.8. Calculated radiative capture absorption rates for five irradiations of CC1.

The effects of shielding modifications are best demonstrated by Figure 4.4, Figure 4.5, and Figure 4.6. The addition of the lithiated window between the detector and the sample prevented scattered neutrons from interacting with the inner walls of the Pb collimator. The spectrum figures clearly show the reduction in ^{207}Pb prompt gamma peaks, and the ensuing reduction in the background continuum. Table 4.2 contains peak area information for ^{1}H, ^{10}B, and ^{207}Pb. For the first three irradiations, the ^{1}H/^{10}B ratio remains constant, a good indicator of reproducibility. The ratio is constant for irradiations 4 and 5, but is almost 2% higher than for irradiations 1-3 because of added ^{1}H interference due to radiative capture events in the lithiated polymer shielding. The addition of this systematic error is important to note, but is worth the added gain due to background reduction.

These experiments enhanced the shielding configuration for the HPGe prompt gamma detector, and showed that reasonable reproducibility could be achieved. Raw count data show that the neutron fluence can vary by several percent from irradiation to irradiation, depending on reactor conditions. Ratios of count data obtained during a single irradiation can been used to eliminate variations in the neutron fluence. These experiments have also shown that four hour irradiation times are not sufficient to obtain counting statistics suitable for quantitative determination.

Table 4.2. Selected Peak Area Data

Irradiation	^{1}H	^{10}B	^{1}H/^{10}B	^{207}Pb
1	41839 ± 236	602992 ± 904	0.0694 ± 0.0004	7737 ± 99
2	4344 ± 239	627157 ± 878	0.0693 ± 0.0004	8107 ± 101
3	45771 ± 244	661249 ± 926	0.0692 ± 0.0004	8404 ± 101
4	44772 ± 244	634546 ± 888	0.0706 ± 0.0004	85 ± 18
5	43602 ± 222	617152 ± 864	0.0707 ± 0.0004	80 ± 15

4.2 Batch Comparisons

A second set of experiments was performed to measure the uniformity of the isotopic concentration in samples cut from the same hydroburst ring. Two groups of samples were used: (1) a set fabricated using YLA, Inc. materials, and (2) a set fabricated using Fiberite materials. The first sample from the YLA group, designated batch A, was the sample used for reproducibility tests. The precise chemical makeup for each batch is unknown but was expected to be similar. Table 4.3 shows the irradiation history for each sample. Figure 4.9 and Figure 4.10 show the absorption rates for batch A and batch B, respectively.

Table 4.3. Irradiation History for each sample

Batch A Samples – YLA	Total Irradiation Time	Batch B Samples – Fiberite	Total Irradiation Time
CCA1	20 h *	CCB1	16 h
CCA2	10 h	CCB2	10 h
CCA3	10 h	CCB3	11.5 h

*Shielding improvements made the last 8 hours of data for CCA1 more useful than the total 20 hours. Only the last 8 hours are used in these calculations.

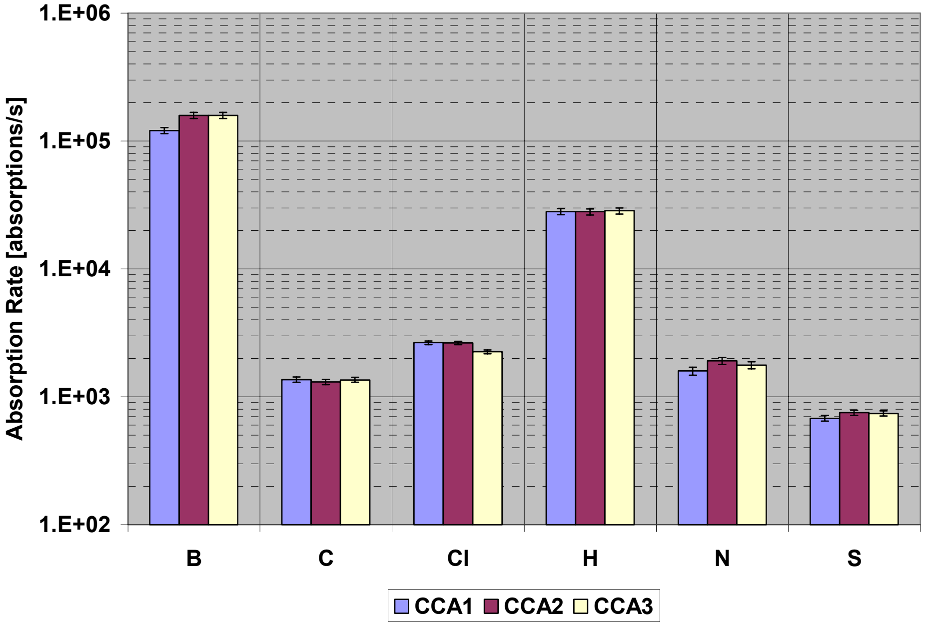

Figure 4.9. Average absorption rates for several elements in samples from Batch A.

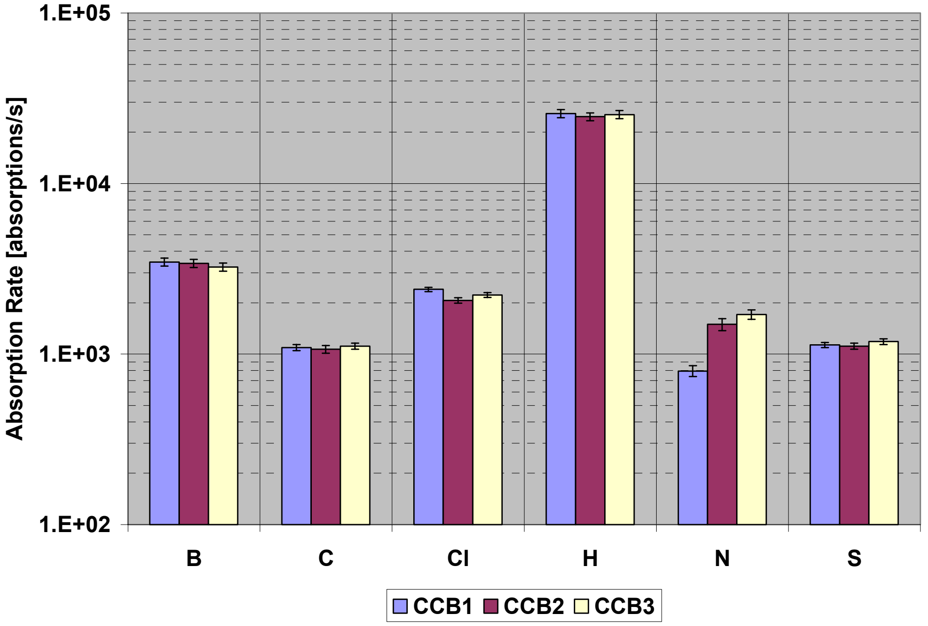

Figure 4.10. Average absorption rates for several elements in different from Batch B.

The composite samples in Batch A are somewhat uniform. From Figure 4.9, it can be seen that the carbon content is nearly identical; however, there appears to be a variation in the boron content. Figure 4.10 shows a variation in the nitrogen content between different samples as well. The measured variations may be due to differences between the sample materials, or a combination of changes in the integrated neutron fluence and uncontrolled interferences.

Figure 4.11 contains the atomic density of elements in each batch relative to the atomic density of carbon in Batch A. The carbon content in each sample is similar, as might be expected for carbon fiber composite materials. It is also interesting to note there is significantly more boron than chlorine in Batch A, not the 1:3 ratio as would be expected for BCl_3, the only known chemical in the samples. There could be several explanations for this discrepancy, including an additional source of boron as an impurity. Batches A and B also differ substantially. There is almost a 2 order of magnitude difference in the boron content, and detectable differences in the nitrogen and sulfur content as well. Thus, the elemental constituents of different carbon fiber composites can vary significantly.

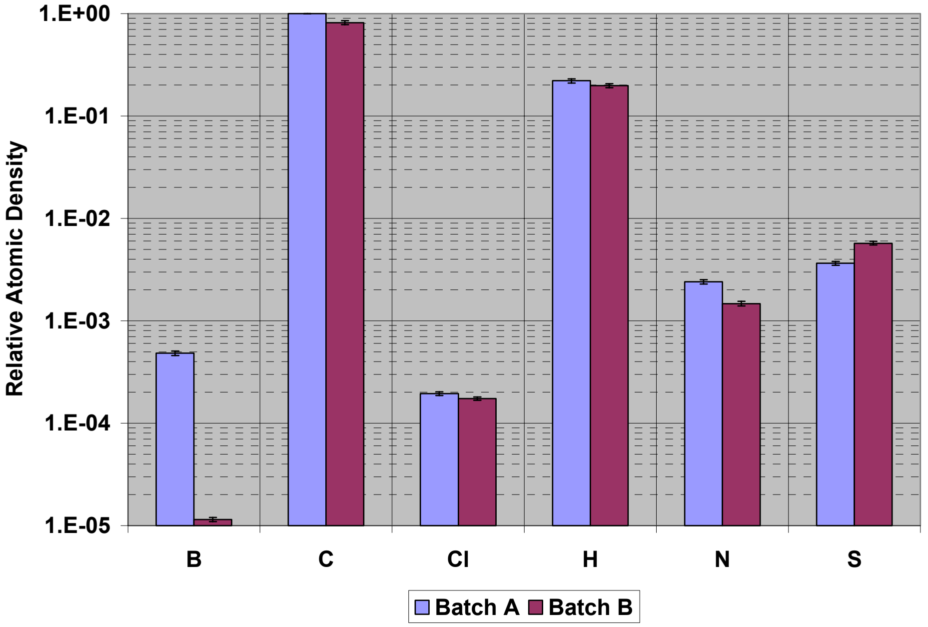

Figure 4.11. Relative average atomic density of elements in Batch A and Batch B compared to the atomic density of carbon in Batch A.

4.3 Beam Monitor Experiments

The neutron flux delivered by the TCNS varies with reactor conditions and will be affected by many factors, including control rod positions and fission product inventory. Variation in the intensity of the neutron flux during the previously described experiments will influence radiative capture reaction rates and prompt gamma measurements. The measured peak areas depend on the total number of radiative capture events, which will depend on the time integrated neutron fluence. Fluence variations must be accounted for when comparing measurements from different irradiations, and the total neutron current delivered must be known for direct quantitative calculations.

Several methods were considered to monitor the neutron flux. The use of photon detectors to count prompt gamma rays from test foils was considered and briefly tested with a NaI(Tl) detector. Logistically, the setup of a second detector presented difficulties, and the development of a flux monitor with neutron detectors was pursued. Tests were made with a ^{3}He tube and two different fission chambers. Dead time measurements and HV curves are shown in Appendix F.

4.3.1 ^{3}He Detector Measurements

^{3}He detectors had previously been used to monitor the neutron flux delivered by the TCNS and were known to saturate at powers greater than a few watts. However, it was suspected that the amount of neutrons leaking out of the neutron guides was proportional to the current of neutrons delivered to the sample. A ^{3}He detector was placed in several locations on and near the neutron guides to count leaking neutrons, as shown in Figure 4.12.

In Position 1, the ^{3}He tube was placed directly on top of the converging guide. The entire guide, including the detector, was wrapped in a lithiated polymer to shield leaking neutrons. This shielding also served to prevent background neutrons from scattering into the ^{3}He detector. Initial measurements were made at a reactor power of 500 kW. Count rate data for 12 subsequent irradiations is shown in Table 4.4, and normalized data (normalized to the first measurement) is plotted in Figure 4.13.

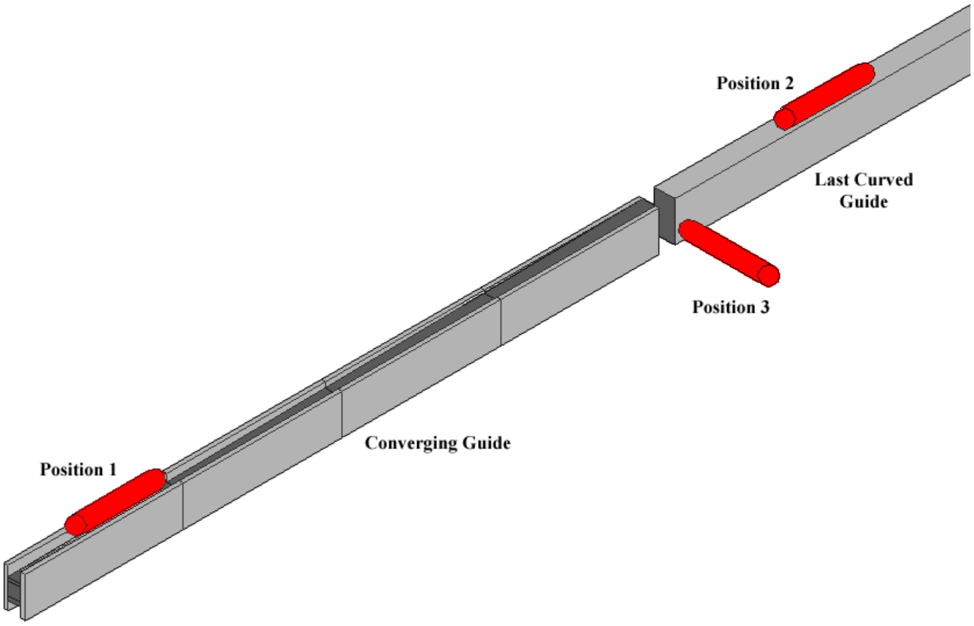

Figure 4.12. Test locations for the ^{3}He detector.

The count rate, and ensuing dead time in position 1 was clearly too high. Figure 4.13 shows a trend in the measured count rates. An additional low power series of measurements were performed to determine if the variations in the 500 kW data were indeed due to changes in the neutron flux delivered to the sample. A series of ^{3}He measurements were made in conjunction with PGAA measurements on a boral plate at a reactor power of 50 kW. By comparing changes in peak areas for the ^{10}B(n,α) reaction with the measured ^{3}He count rate, the source of trending in the ^{3}He measurements might be identified. Data measured during this experiment is shown in Table 4.5, and normalized measurements are plotted in Figure 4.14. The average ^{3}He tube dead time for Position 1 at 50 kW was 7.2%.

Table 4.4. ^{3}He Detector Measurements in Position 1 at 500 kW

Irradiation	Time [s]	CPS	Dead Time
1	60	10297 ± 17	39.0%
2	60	10420 ± 17	39.3%
3	60	10517 ± 17	39.5%
4	60	10601 ± 17	39.7%
5	60	10664 ± 17	39.8%
6	60	10840 ± 17	40.2%
7	60	10906 ± 17	40.3%
8	60	10927 ± 17	40.4%
9	60	11003 ± 18	40.6%
10	60	10966 ± 18	40.5%
11	600	11221 ± 6	41.0%
12	1800	11172 ± 3	40.9%

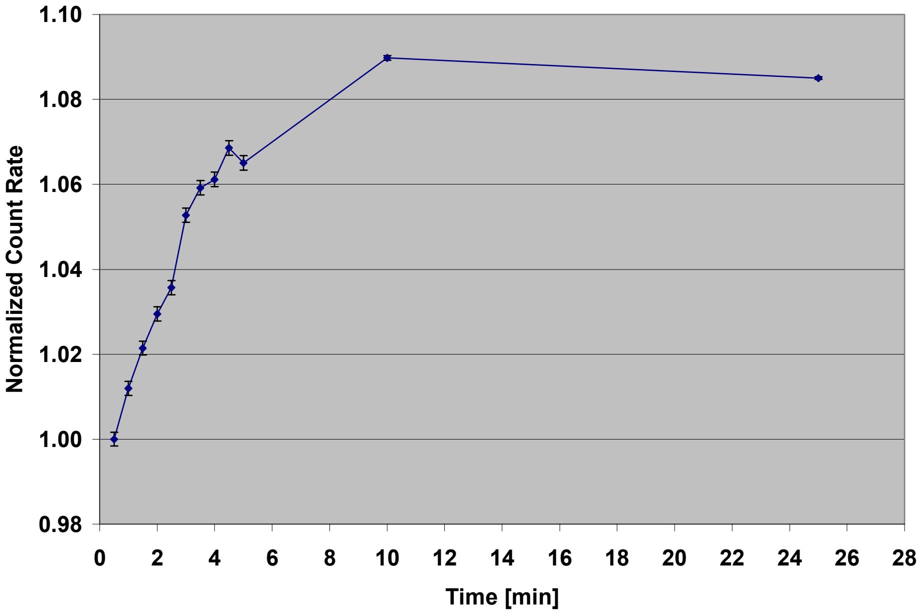

Figure 4.13. Normalize ^{3}He count rate data plotted at center of counting time interval.

Table 4.5. Measured ^{10}B (n,α) and ^{3}He count rates at 50kW

Irradiation	^{10}B [CPS]	^{3}He [CPS]
1	58.1 ± 0.5	1323 ± 2
2	60.2 ± 0.5	1245 ± 2
3	60.5 ± 0.5	1240 ± 2
4	59.9 ± 0.5	1237 ± 2
5	60.3 ± 0.5	1244 ± 2
6	59.9 ± 0.5	1240 ± 2

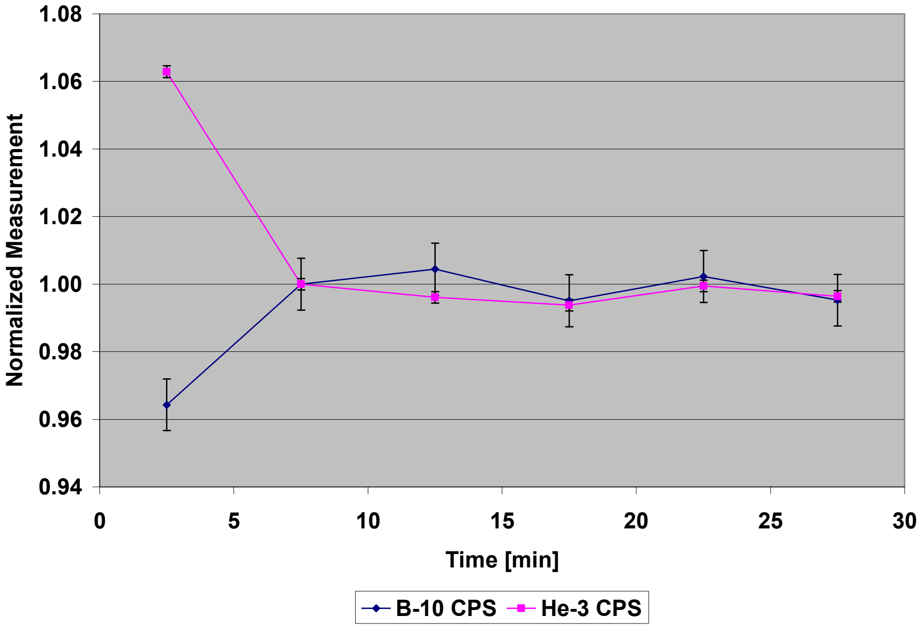

Figure 4.14. Normalize comparison of ^{10}B and ^{3}He count rates during 5 minute irradiations at 50kW with ^{3}He detector in Position 1.

Data in Figure 4.14 is normalized to the second irradiation. It is suspected that the helium gas concentration in the converging guide had not yet come to equilibrium, increasing the rate at which neutrons scattered out of the guide and decreasing the net flux delivered to the sample. Subsequent measurements clearly show that the ^{3}He detector tracks well with count rates measured by PGAA. Significant trending in either measurement is not seen, as had been observed in previous ^{3}He data at 500 kW. Nevertheless, it was decided that the use of a ^{3}He neutron detector to count neutrons that scattered out of the cold neutron guides would be sufficient to track changes in the neutron flux delivered to a PGAA sample. It was decided that the ^{3}He flux monitor would be placed in a location where the maximum dead time would be less than 5%.

Additional flux monitor tests were made in position 2 with the ^{3}He tube fixed to the top of the last curved guide with nylon straps. The curved guides are wrapped in a borated material to shield leaking neutrons, and lower count rates are expected. A potential drawback, however, is that measurements of neutrons leaking from the curved guides occur farther away from the sample. Count rate data for the ^{3}He detector and PGAA data for the Boral plate were measured at multiple power levels, as plotted in Figure 4.15. Raw data is shown in Table 4.6.

The irradiations for ^{3}He were performed in the order shown in Table 4.6. Measurements at 1000 kW gradually trend lower. Once the power was decreased to 500 kW, measurements gradually trended back to higher values. The cause for these changes in the neutron flux has not yet been determined, but the ^{3}He detector adequately tracks the variations in the neutron flux. It is hypothesized that these are changes due to actual variations in the core power level and not poor indications from the ^{3}He tube. The measured dead times at Position 2 are still greater than the 5% cutoff, and the ^{3}He tube was moved to Position 3.

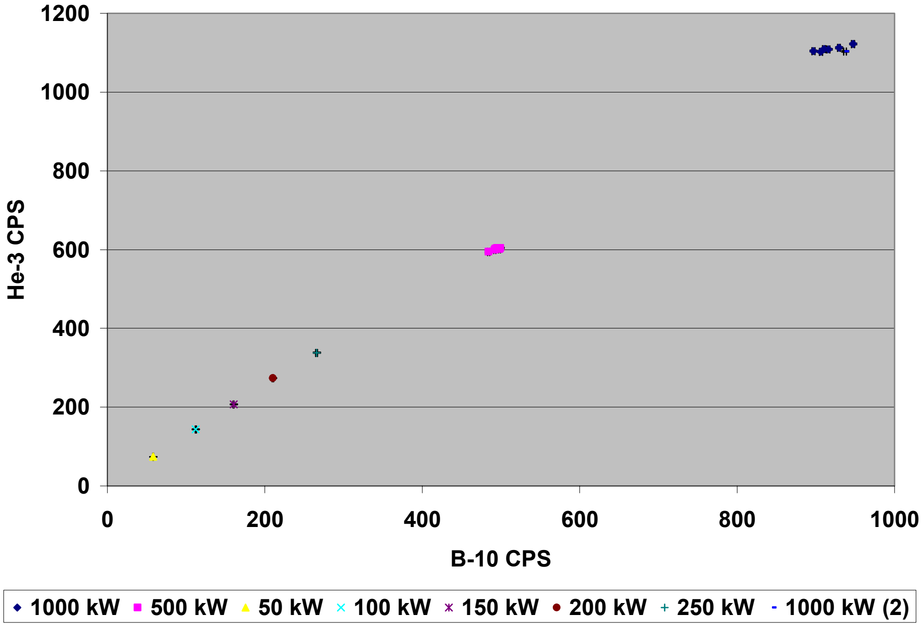

Figure 4.15. ^{3}**He count rate vs.** ^{10}**B count rate during 5 minute irradiations at various power levels. The** ^{3}**He tube is in position 2.**

Table 4.6. Series of 5 Minute Irradiations with ^{3}**He Detector in Position 2.**

Irradiation	Power [kW]	^{10}B [CPS]	^{3}He [CPS]	^{3}He Dead Time
1	1000	947 ± 2	1122 ± 2	6.51%
2	1000	929 ± 2	1113 ± 2	6.45%
3	1000	916 ± 2	1108 ± 2	6.43%
4	1000	910 ± 2	1109 ± 2	6.44%
5	1000	906 ± 2	1103 ± 2	6.40%
6	1000	897 ± 2	1104 ± 2	6.41%
7	500	484 ± 1	594 ± 1	3.56%
8	500	492 ± 1	600 ± 1	3.59%
9	500	493 ± 1	602 ± 1	3.60%
10	500	495 ± 1	604 ± 1	3.61%
11	500	498 ± 1	601 ± 1	3.59%
12	500	499 ± 1	604 ± 1	3.61%
13	50	58.2 ± 0.5	74 ± 0	0.46%
14	100	112.2 ± 0.6	144 ± 1	0.88%
15	150	160.4 ± 0.8	207 ± 1	1.27%
16	200	210.3 ± 0.9	274 ± 1	1.67%
17	250	266 ± 1	338 ± 1	2.05%
18	1000	937 ± 2	1103 ± 2	6.40%

At Position 3, the ^{3}He tube is pointed at the gap between the curved guide and the converging guide with the intent of counting neutrons that scatter in air between the two guides. The tube itself has also been wrapped with borated polyurethane to reduce the influence of background neutrons that have leaked from other locations. PGAA measurements at Position 3 were taken with the ORTEC HPGe detector using a boron atomic absorption standard solution as the sample. The HPGe detector position and shielding, as well as the detector and sample, are different than the previous measurements (shown in Table 4.5 and Table 4.6) so direct comparisons are not meaningful. The goal of these experiments is to determine the appropriate location for the ^{3}He detector so comparisons to previous measurements are not needed.

A series of 36 twenty minute irradiations was carried out over several days to determine how well the ^{3}He detector in Position 3 tracked the neutron flux delivered to the sample. Measured count rate data has been tabulated in Table 4.7, and has been plotted in Figure 4.16.

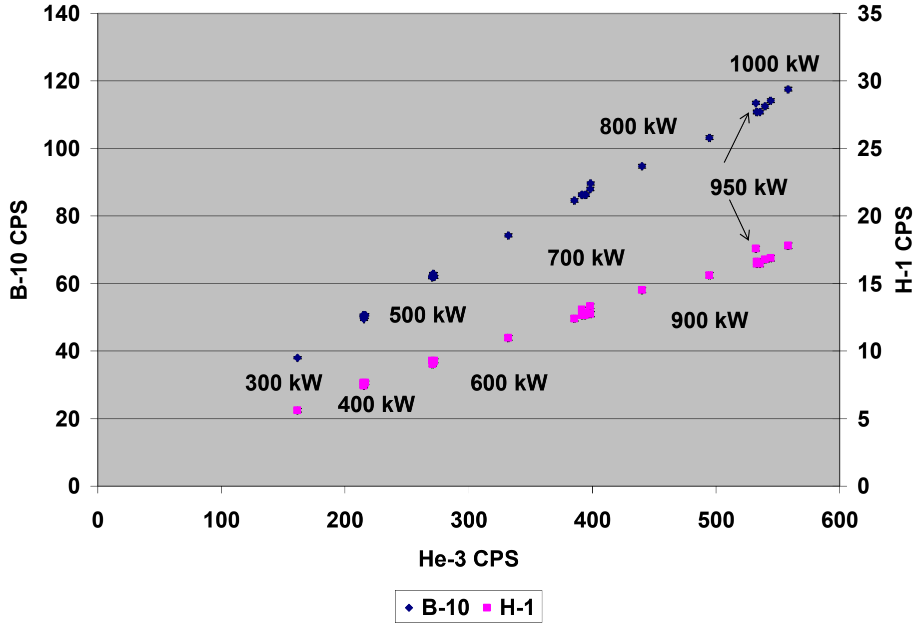

Figure 4.16. Measured count rates with Boron AAS solution and ^{3}He detector in position 3.

Table 4.7. Measured Data with Boron AAS Solution and ^{3}He Detector in Position 3.

Irradiation	Power [kW]	^{10}B [CPS]	^{1}H [CPS]	^{3}He [CPS]	^{3}He Dead Time
1	950	113.5 ± 0.5	17.6 ± 0.2	270.7 ± 0.5	2.5%
2	500	62.2 ± 0.4	9.0 ± 0.2	271.8 ± 0.5	1.3%
3	500	62.1 ± 0.4	9.2 ± 0.2	271.1 ± 0.5	1.3%
4	500	62.8 ± 0.4	9.1 ± 0.2	272.1 ± 0.5	1.3%
5	500	62.0 ± 0.4	9.3 ± 0.2	271.6 ± 0.5	1.3%
6	500	62.8 ± 0.4	9.2 ± 0.2	270.3 ± 0.5	1.3%
7	500	61.9 ± 0.4	9.3 ± 0.2	215.0 ± 0.4	1.3%
8	400	50.1 ± 0.4	7.5 ± 0.1	214.8 ± 0.4	1.0%
9	400	50.6 ± 0.4	7.7 ± 0.1	215.2 ± 0.4	1.0%
10	400	49.9 ± 0.4	7.4 ± 0.1	215.6 ± 0.4	1.0%
11	400	50.1 ± 0.4	7.6 ± 0.1	216.3 ± 0.4	1.0%
12	400	50.7 ± 0.4	7.7 ± 0.1	215.3 ± 0.4	1.0%
13	400	49.5 ± 0.4	7.5 ± 0.1	558.2 ± 0.7	1.0%
14	1000	117.6 ± 0.6	17.8 ± 0.2	544.0 ± 0.7	2.6%
15	1000	114.2 ± 0.6	16.9 ± 0.2	539.6 ± 0.7	2.5%
16	1000	112.5 ± 0.6	16.8 ± 0.2	535.5 ± 0.7	2.5%
17	1000	110.8 ± 0.6	16.5 ± 0.2	533.0 ± 0.7	2.5%
18	1000	110.8 ± 0.6	16.5 ± 0.2	533.0 ± 0.7	2.5%
19	1000	110.8 ± 0.6	16.6 ± 0.2	398.4 ± 0.6	2.5%
20	700	89.7 ± 0.5	12.7 ± 0.2	398.3 ± 0.6	1.9%
21	700	88.0 ± 0.5	13.3 ± 0.2	394.8 ± 0.6	1.8%
22	700	86.3 ± 0.5	12.8 ± 0.2	393.9 ± 0.6	1.8%
23	700	86.3 ± 0.5	12.7 ± 0.2	391.4 ± 0.6	1.8%
24	700	86.3 ± 0.5	13.1 ± 0.2	391.7 ± 0.6	1.8%
25	700	86.3 ± 0.5	12.7 ± 0.2	494.7 ± 0.6	1.8%
32	900	103.2 ± 0.5	15.6 ± 0.2	385.4 ± 0.6	2.3%
33	700	84.6 ± 0.5	12.4 ± 0.2	161.5 ± 0.4	1.8%
34	300	38.0 ± 0.3	5.6 ± 0.1	331.9 ± 0.5	0.7%
35	600	74.3 ± 0.4	11.0 ± 0.2	440.1 ± 0.6	1.5%
36	800	94.8 ± 0.5	14.5 ± 0.2	0.0 ± 0.0	2.0%

The measured count rates and dead times with the ^{3}He detector in Position 3 are acceptable. Transients in the reactor conditions, i.e. significantly changing the reactor power, lead to slower transients in the neutron flux delivered to a PGAA sample. PGAA and ^{3}He count rates increase and decrease linearly with small changes in reactor power. Large changes, i.e. from 500 kW to 1000 kW, do not increase the delivered flux by a factor of 2. Also, after large changes in reactor power, the neutron flux delivered by the TCNS appears to undergo a slow transient in the inverse direction of the power change after the new level is attained. This again appears to be due to actual tends in the core power and not due to incorrect indications by the ^{3}He tube. It is recommended that PGAA irradiations always be performed at maximum power to maximize the neutron flux delivered to the sample, but the measured trends show that ^{3}He measurements can be used to compare the relative flux delivered to PGAA samples during different irradiations of any power.

4.4 Flux and Efficiency Calibrations

To be able to quantitatively calculate the amount of a particular isotope in a PGAA sample from a single irradiation, both the integrated neutron fluence and the detection efficiency for the emitted prompt gammas must be known. In practice, these terms can be difficult to determine experimentally or calculate accurately. A technique has been developed to allow the determination of both quantities simultaneously by irradiating an isotope that will activate with a short half-life and emit a spectrum of prompt and decay gammas with reasonable intensity. For this investigation, a vanadium foil was used.

4.4.1 Theory

The method described in this section can be applied to any sample with similar prompt and radioactive decay properties. Consider the physical data listed for vanadium in Appendix E. Natural vanadium is composed almost entirely of ^{51}V (99.750%). ^{51}V has a 2200 m/s radiative capture cross section of 4.9 barns and emits a wide spectrum of prompt gamma rays. The activation product, ^{52}V, has a half-life of 3.743 minutes and decays by the emission of a 1434.1 keV gamma ray with a 100% yield. Consider the ^{52}V activity as a function of time during the irradiation of a 37 mg foil at 1×10^7 n/cm^2/s, as shown in Figure 4.17. After 30 minutes of irradiation, the activity will be 99.6% saturated and reasonably constant.

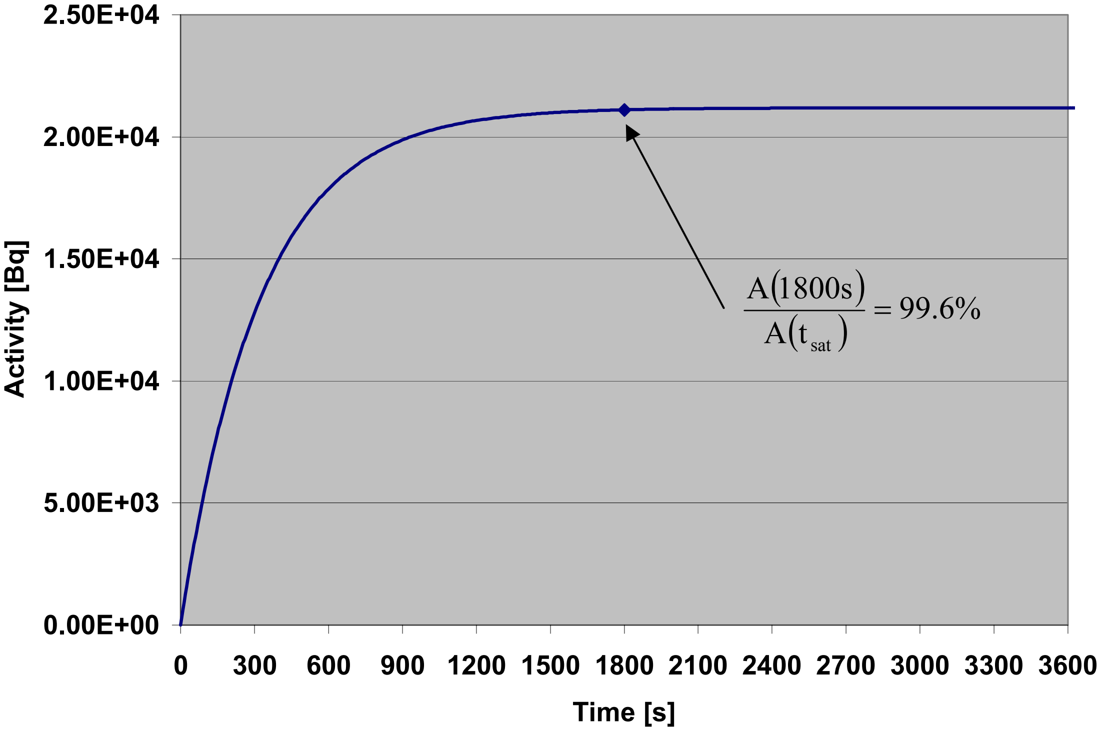

Figure 4.17. Calculated ^{52}V activity as a function of time for a 37 mg natural Vanadium foil exposed to a 1×10^7 n/cm^2/s neutron flux.

If a PGAA spectrum of the vanadium foil is acquired after the sample is allowed to reach a saturation activity, the emission rate of the 1434.1 keV decay gamma will be constant and directly related to the neutron fluence rate according to

$$A_{^{52}V} = \int_V \int_0^\infty N_{^{51}V}(\vec{r})\sigma_{n,\gamma\,^{51}V}(E)\phi(\vec{r},E)dEd\vec{r}\ . \qquad 4\text{-}4$$

This equation can be simplified by using the total number of ^{51}V atoms and a 2200 m/s cross section to calculate a 2200 m/s equivalent flux spatially averaged across the vanadium foil, and rearranged to obtain

$$\phi_{2200EQ} = \frac{A_{^{52}V}}{N_{^{51}V}\sigma_{n,\gamma 2200\,^{51}V}}. \qquad 4\text{-}5$$

The total number of ^{51}V atoms can be determined from the foil mass, cross sections can be looked up from tabulated values, and the ^{52}V activity must be measured. ^{52}V is particularly well suited for this method, as it has a decay gamma at 1434.1 keV, which is very close to the ^{152}Eu 1408 keV decay peak. If the detector is calibrated with a ^{152}Eu source prior to the irradiation, the ^{52}V activity and the neutron flux can be measured.

Flux merasurements do not necessarily require that ^{52}V be allowed to saturate, as buildup and decay equations are well known and can easily be solved analytically when using the spatial and energetic assumptions employed here. To calculate efficiency, however, the ^{52}V activity must be allowed to saturate so we can determine the neutron absorption rate within the V foil. By definition, saturation occurs when the decay rate equals the production rate, and ^{52}V is produced by neutron capture events with ^{51}V. Prompt gamma yields are tabulated values. If the prompt gamma emission rate is known and the detection rate has been measured, the efficiency can be determined easily.

4.4.2 Data

The vanadium foil experiment was initially performed before the flux monitor was installed. Also, the first attempt was ended prematurely by a reactor scram 2 hours into the run after saturation. The neutron flux, however, has been calculated based on the data acquired during the first 30 minutes of irradiation. The ^{52}V peak area at 1434.1 keV was measured as 5447 ± 87 after 1800 seconds of live time. The efficiency at this energy had previously been determined during a 60 hour calibration with a ^{152}Eu source with an activity known to within 5%. The measured efficiency at 1434.1 keV was 0.000159 ± 0.000008. The average thermal equivalent neutron flux was calculated using

$$\phi_{2200\,EQ} = \frac{C_{measured}}{\varepsilon_{measured}\sigma_{2200}N_{^{51}V}\left[t - \frac{1}{\lambda}\left(1 - e^{-\lambda t}\right)\right]} . \qquad 4\text{-}6$$

The average 2200 m/s equivalent flux in the vanadium foil for this 30 minute irradiation at 950 kW was calculated to be $(1.09 \pm 0.06)\times10^{7}$ n/cm^{2}/s. The error in this measurement is dominated by the error in the ^{152}Eu calibration source.

The experiment was repeated two days later and data was successfully acquired during an 8 hour irradiation at 950 kW after the vanadium foil was allowed 30 minutes to approach a saturation activity. The ^{52}V peak area at 1434.1 keV was measured as 90303 ± 348 after 28800 seconds of live time. The corresponding average 2200 m/s equivalent flux in the vanadium foil is $(9.28 \pm 0.51)\times10^{6}$ n/cm^{2}/s. The flux measured over the 8 hour period is nearly 15% lower than the flux measured over 30 minutes in the previous test. The decrease in flux is not inconsistent with trends seen in the neutron flux delivered by the TCNS. Fission product inventories due to recent reactor activities influence the neutron flux from day to day and while operating at high power. The neutron flux has been shown to decrease over the course of a day.

The saturated ^{52}V activity during the 8 hour irradiation was measured at 19.7 ± 1.0 kBq, and a radiative capture reaction rate of 19700 ± 1000 reactions per second. Efficiencies at the vanadium prompt gamma energies were calculated using

$$\varepsilon_{x} = \frac{\dot{C}_{x}}{RR_{measured}\,y_{x}} . \qquad 4\text{-}7$$

Efficiency curves extrapolated from the existing ^{152}Eu calibration, and the efficiency curve calculated from the vanadium data are shown in Figure 4.18. The vanadium efficiency curve will only be as accurate as the prompt gamma yields in the selected library. Figure 4.18 clearly shows some outliers where the yield is either incorrect or there is unidentified interference.

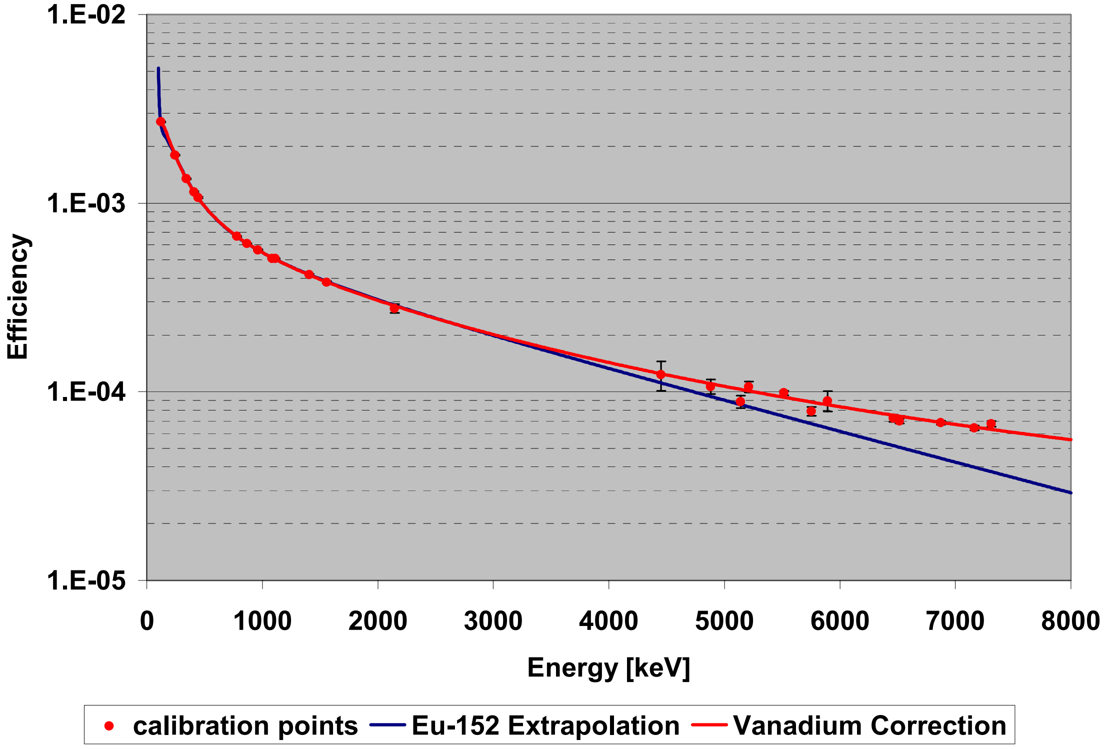

Figure 4.18. Detection efficiency curves in Fall of 2002.

The vanadium foil measurement was repeated periodically as reactor conditions and detector positions were altered. Predictably, as the sample geometry was optimized and the distance between the sample and detector was minimized, prompt gamma detection efficiencies increase. Table 4.8 shows how 2200 m/s equivalent fluxes changed over a similar time period. Trends are less obvious, but for the most part can be explained.

Table 4.8. Flux Measurements with a Vanadium Foil at 950 kW

Measurement	Date	Time [s]	2200 m/s Eq Flux [n/cm^2/s]
1	7/17/2001	1800	$(10.9 \pm 0.6) \times 10^6$
2	7/19/2001	28800	$(9.28 \pm 0.55) \times 10^6$
3	10/31/2002	1800	$(6.91 \pm 0.18) \times 10^6$
4	10/31/2002	27000	$(6.54 \pm 0.15) \times 10^6$

Changes in the fluence rate over the course of this investigation were expected due to several changes in the reactor core arrangement. A detailed history of all core loadings relevant for these experiments is shown in Appendix B. Other changes can be attributed to the fission product inventory of the core do to operation schedules. The fluence rate decrease between 7/17/2001 and 7/19/2001 is typical after operating the reactor for three consecutive days. Also, the measurement on 7/17/2001 was taken over 30 minutes, while the 7/19/2001 measurement was taken over an 8 hour period. Since the fluence rate decreases steadily during operation, longer acquisitions will result in a lower average flux. On 7/30/2001, the reactor core was permanently put into the 3L configuration, which required the removal of three fuel rods (See Appendix B). The subsequent loss of reactivity, and flux titling away from BP3, accounts for the large drop off between measurement 2 and 3. Measurement 4 was performed on the same day as measurement 3, and demonstrates the slow decrease in the fluence rate that results in a lower average flux for longer acquisition periods.

Vanadium flux measurements performed in 2002 have also been used to correlate ^{3}He tube measurements to the fluence delivered to the vanadium foils. ^{3}He count rates during each irradiation are shown in Table 4.9. The best indication of flux monitor accuracy is the data from 10/31/2001. The vanadium foil was not moved during these tests and the only variables were time and the neutron flux. ^{3}He count normalization can properly account for daily variations in the neutron fluence rate.

Table 4.9. Flux Monitor Normalization during Vanadium Flux Measurements

Date	^{3}He [CPS]	[n/cm^2/^{3}He counts]
10/31/2001	456.5 ± 0.5	(1.51 ± 0.04) × 10^4
10/31/2001	444.6 ± 0.1	(1.47 ± 0.03) × 10^4

The use of vanadium for this experiment is not exclusive. Vanadium has the benefit of a short activation half-life and quickly comes to equilibrium, allowing for an efficiency calibration to be performed in a single measurement. Cobalt foils have been used by experimenters at other facilities, but require additional measurements to determine the induced activity after PGAA measurements. Cobalt experiments have been performed at the UT-NETL, but the induced activity after a full day of irradiation is only on the order of 200 Bq, a difficult activity to precisely measure in reasonable times. Vanadium foils are also reusable because induced activity quickly decays away.

4.5 Flux Mapping

The method described in section 4.4 is adequate to determine the average fluence delivered to an area or the spatial and time averaged flux over an entire irradiation. The foil was cut to be approximately 1 cm^2 in area, and is sufficient to estimate the fluence delivered to samples held in the vertical sample holder. Unfortunately, the single foil is of insufficient area to determine the total fluence delivered to the vertical samples (recall Figure 4.1). The issue is further compounded by the use of foils of different width and height. The fluence delivered to each sample will be different, but must be determined.

4.5.1 Radiography

Neutron flux profiles can be measured by neutron radiography, and equipment is in place to mount a neutron radiography camera in the cold neutron beam (shown in Figure 4.19). The radiography camera was used to acquire 100 images each at several distances from the converging guide to examine the spatial profile of the beam as it converges to the focal plane. Averaged images are shown in Figure 4.20. An indium wire was crossed on the front of the converging guide to provide a point of reference for each image. It becomes blurred and finally obscured as neutrons converge and scatter.

The acquired radiographs confirm that the intensity of the beam has a spatial component across the focal plane and show the importance of sample placement within the beam. The radiographs also highlight how samples of different geometry will be exposed to different average neutron currents. Radiographs can be used to measure profiles, but the camera is not adequately calibrated to make direct neutron flux determinations.

Figure 4.19. Radiography camera mounted in BP#3.

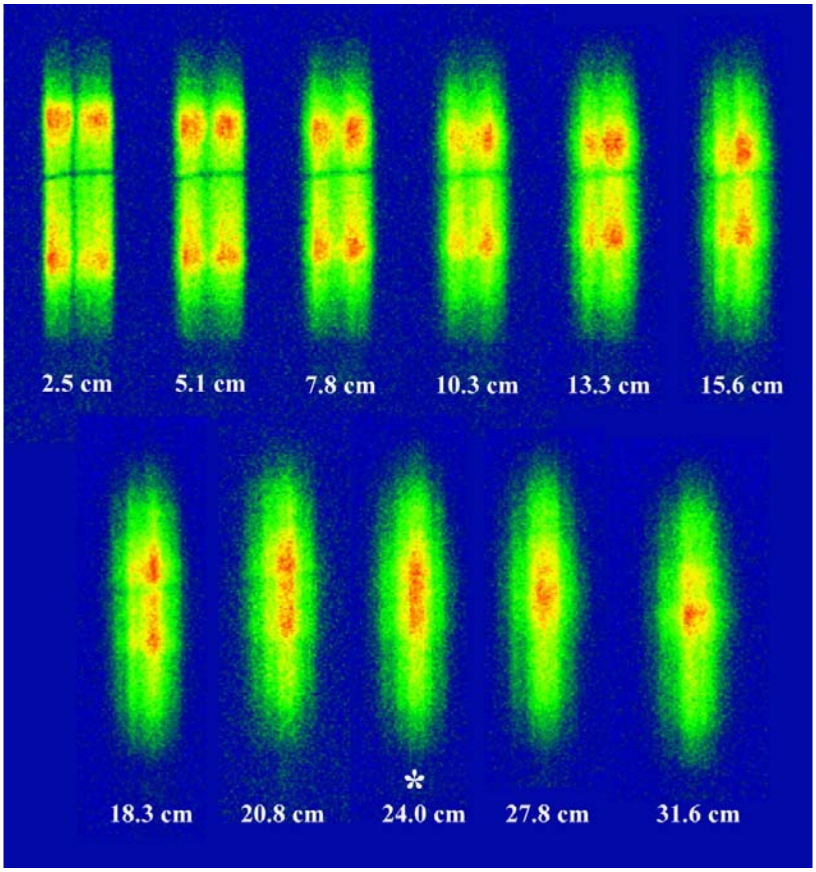

Figure 4.20. Series of radiographs at increasing distances from the end of the cold neutron converging guide at 50 kW (* indicates focal plane).

4.5.2 Prompt Gamma Mapping

A second experiment was devised to use PGAA to quantitatively map the neutron flux in a plane at a 45^{o} angle to the neutron beam and HPGe detector, the same angle at which PGAA samples are typically held. A 0.5 cm × 0.5 cm grid was printed on a sheet of paper and fixed to the frame of a sample holding apparatus. A 1.4 mg sample of cadmium metal was then irradiated for 20 minutes at several positions on the grid to map out the spatial variation in the neutron flux. A similar grid was measured for efficiency as well (see Figure 4.21). The sample size was selected to allow for reasonable counting statistics to be obtained with short irradiations, and to allow the sample to be accurately approximated as a point source. The PGAA detector was also efficiency calibrated with a NIST-traceable ^{152}Eu point source in each position where Cd data was obtained. In doing so, the 2200 m/s equivalent flux at each position was determined using Equation 3-12. Due to the very high absorption cross section for cadmium, even the tiny sample cannot be treated as thin. Thus, neutron attenuation in the sample had to be considered.

Figure 4.21. Grid used to map general neutron flux.

It was found that the magnitude of the neutron flux can change by more than an order of magnitude in 1.0 cm, and the efficiency can vary as much as 10% across a similar space. Averages of the spatial variation around the peak of the neutron flux compare well with the previous measurements with a vanadium foil. The peak 2200 m/s equivalent neutron flux was measured as $(9.2 \pm 1.3)\times10^6$ n/cm^2/s. However, the average 2200 m/s equivalent neutron flux over a 1 cm^2 area around the maximum point is only (6.7 ±

0.5)×10^6 n/cm^2/s. Large error bars are due to the imprecise measurement of the cadmium sample mass as 1.4 ± 0.2 mg, but the 1 cm^2 average flux agrees with the most recent vanadium flux measurements shown in Table 4.8.

The cadmium sample was moved to map the 2200 m/s equivalent flux for a 4 cm by 2 cm area of the beam. Measurements were made before and after the addition of fresh fuel to the reactor core, but the delivered flux did not change appreciably. The horizontal flux profile near the peak of the beam is shown in Figure 4.22. The vertical flux profile near the peak of the beam is shown in Figure 4.23.

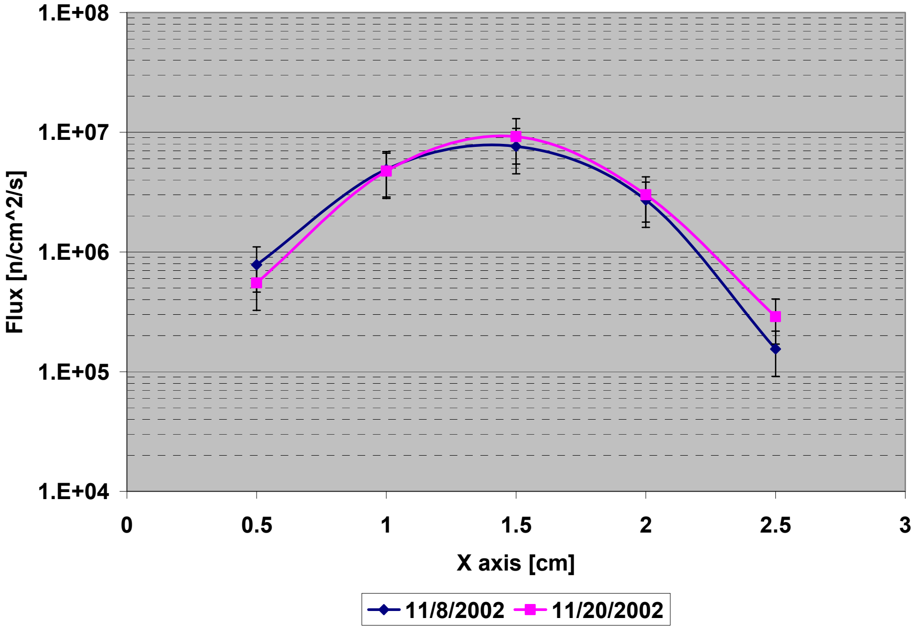

Figure 4.22. Horizontal 2200 m/s equivalent flux profile before and after fuel addition.

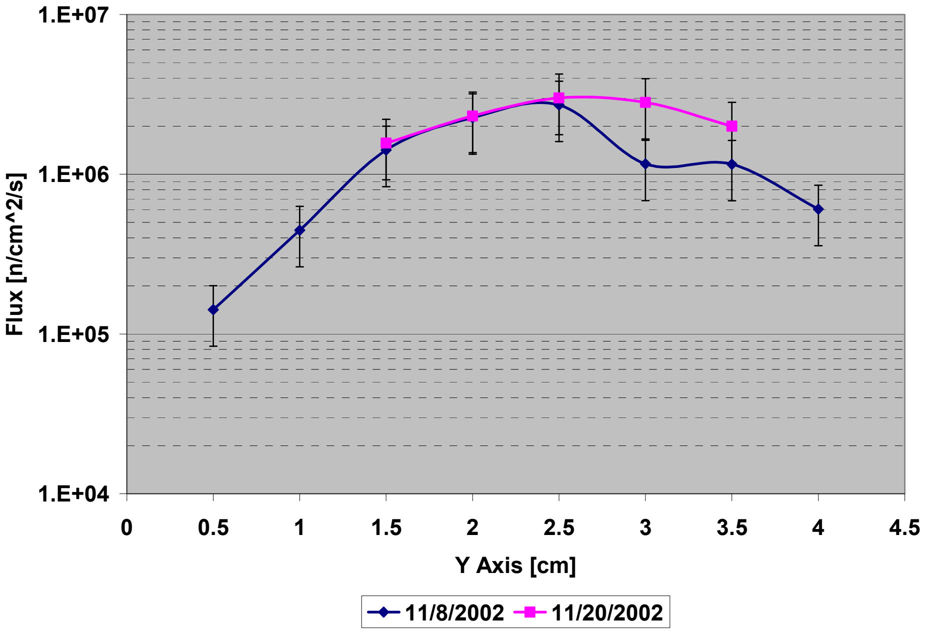

Figure 4.23. Vertical 2200 m/s equivalent flux profile before and after fuel addition.

4.5.3. Combination

It is extremely time consuming to generate a high resolution map of the entire neutron beam profile using a cadmium sample; however, by merging the cadmium and radiograph measurements, a more detailed model can be generated than by either method alone. To match cadmium measurements, 100 radiograph images of the beam focal plane at 50 kW acquired and summed to minimize random fluctuations in beam intensity (shown in Figure 4.24). The peak vertical radiography profile was then matched with the vertical profile measured by the Cd sample, as shown in Figure 4.25. Radiography pixel values range from 0 to 255. The cadmium data was used to calibrate the pixel values to determine that 1 pixel count is equal to $(7.4 \pm 1) \times 10^4$ n/cm^2/s (2200 m/s equivalent).

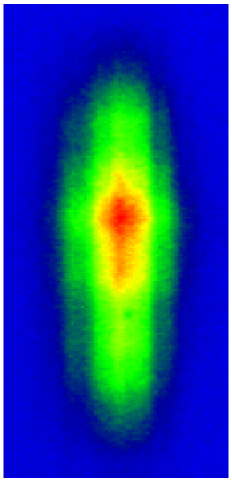

Figure 4.24. Average of 100 radiographs of the cold neutron beam focal plane at a reactor power of 50 kW.

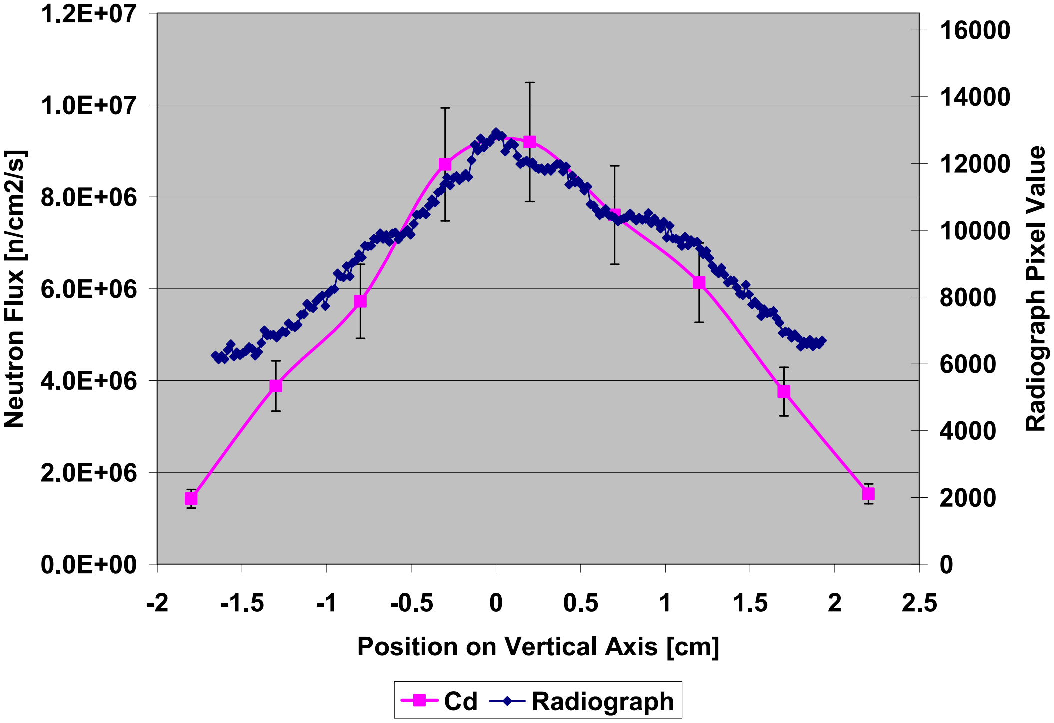

Figure 4.25. Peak flux vertical flux profile measured by Cd sample compared with peak vertical flux profile measured by radiography camera.

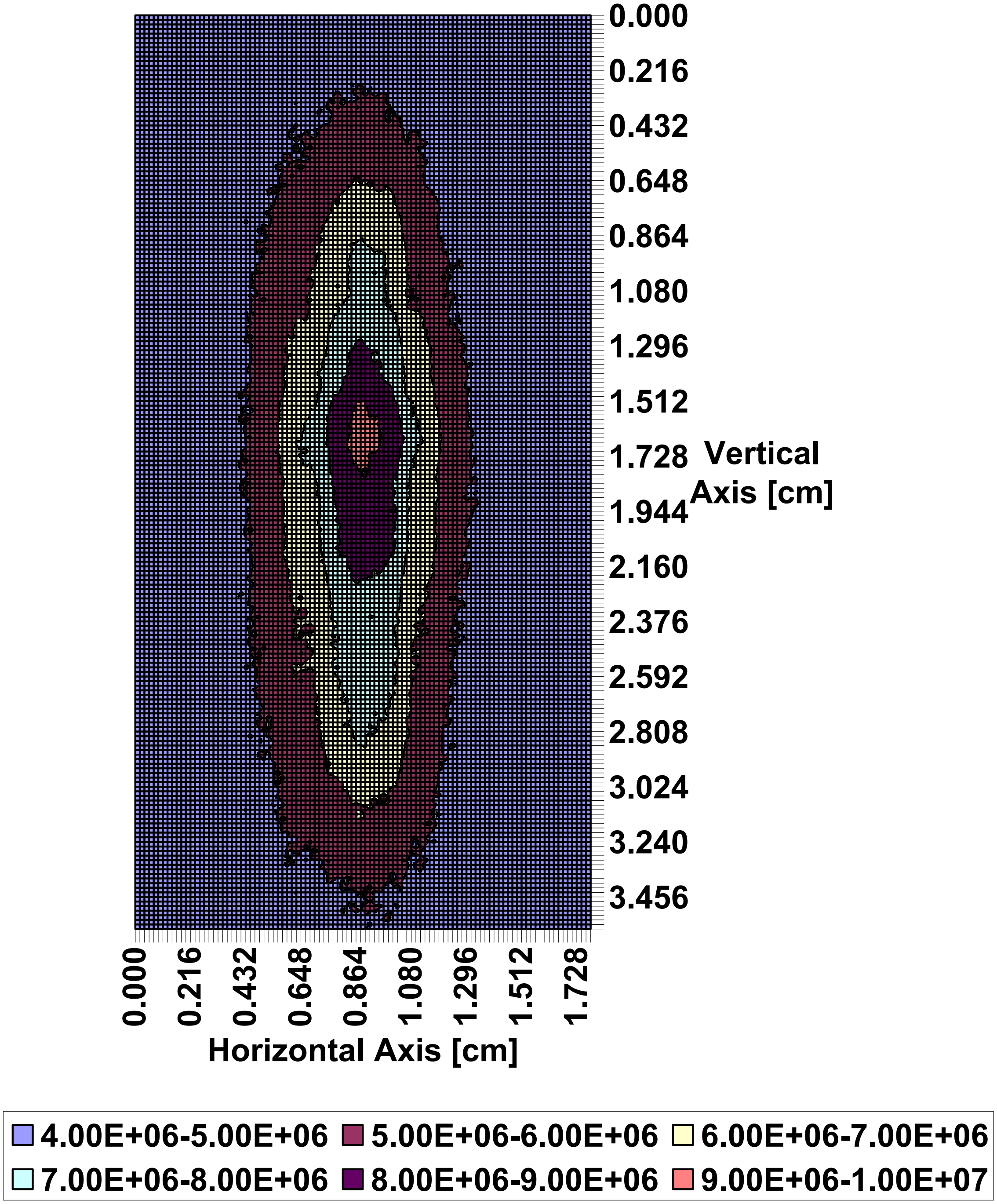

Figure 4.26. Measured 2200 m/s equivalent flux map profile after addition of reactor fuel.

CHAPTER 5. Water Uptake Measurements

5.1 Introduction

For quality assurance and materials characterization, the UT-CEM uses several nondestructive evaluation techniques (NDE), as discussed in Chapter 1. Ultrasonic techniques are of most interest to this work. Through-transmission (TT) and pulse-echo (PE) techniques have been used for flaw detection, and acousto-ultrasonics (AU) and ultrasonic spectroscopy (US) have been used for degradation and damage assessment before and after degradation and burst tests. It is a common practice in acoustic NDE to submerge the test sample and use water as a medium to conduct sound waves between the sample, transducer, and receiver. Figure 5.1 shows a flywheel ring in an acoustic testing facility at NASA's Johnson Space Center.

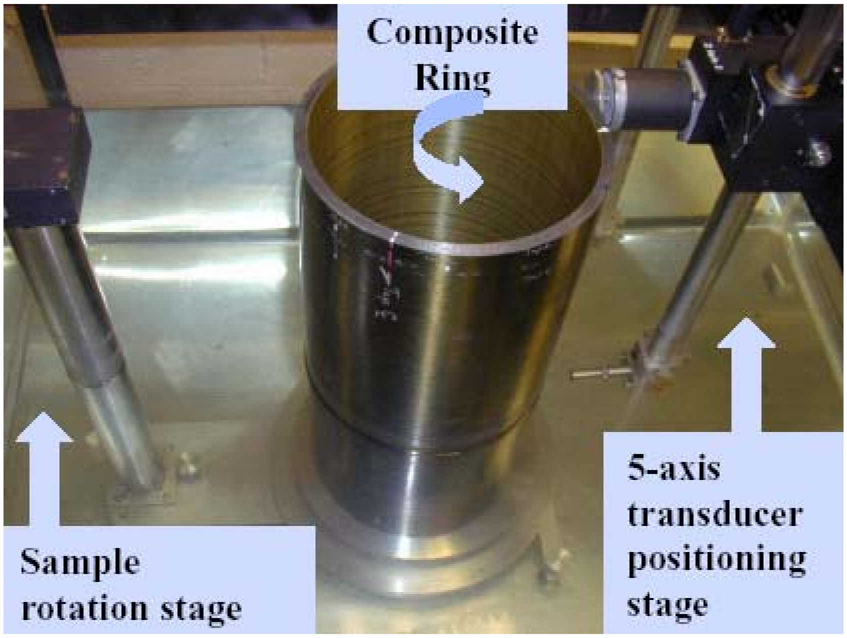

Figure 5.1 Composite ring in immersion ultrasonic scanning system.

Both the carbon fiber reinforcement and the epoxy matrix absorb water, and rotors that have undergone ultrasonic testing have qualitatively shown visible changes. Water absorption by polymer matrix composites is known to influence structural integrity by changing hydrogen bonds within the material [96]. A non-uniform addition of mass could also affect rotor balance. Current ASTM standards for the determination of water content in composite materials call for gravimetric techniques. PGAA is commonly used as a method for low level hydrogen measurements, and may be a more sensitive tool for the investigation of water content of the polymer matrix composite materials in question.

5.2 Sensitivity

Mass measurements are an indirect measurement of changes in water content. ASTM standards require the assumption that all mass change is due to the transport of water in or out of a sample and do not thoroughly address other mechanisms for mass change. PGAA can directly track ^{1}H, which accounts for nearly 100% of the radiative capture cross section for the water molecule, and the need to account for the transport of other molecules in or out of the test sample is eliminated. The percentage change in ^{1}H concentration is also likely to be greater than the percentage change in the mass of the test sample. The combination of these two factors may lead to increased sensitivity and reduced interference.

Consider the example of a composite sample with a mass of 1 g that is initially 3% ^{1}H by mass. As water is absorbed into this sample, the relative change in ^{1}H mass will be greater than the relative change in total sample mass, as shown in Figure 5.2. The absorption of 60 mg of water will increase the total sample mass by 6%, but will increase the ^{1}H mass by over 13%. For any sample where the initial ^{1}H concentration is less than that of water, percent changes in ^{1}H concentration will be greater than percent changes in total mass. The ^{1}H content of water, approximately 11% by mass, is exceeded by few structural materials.

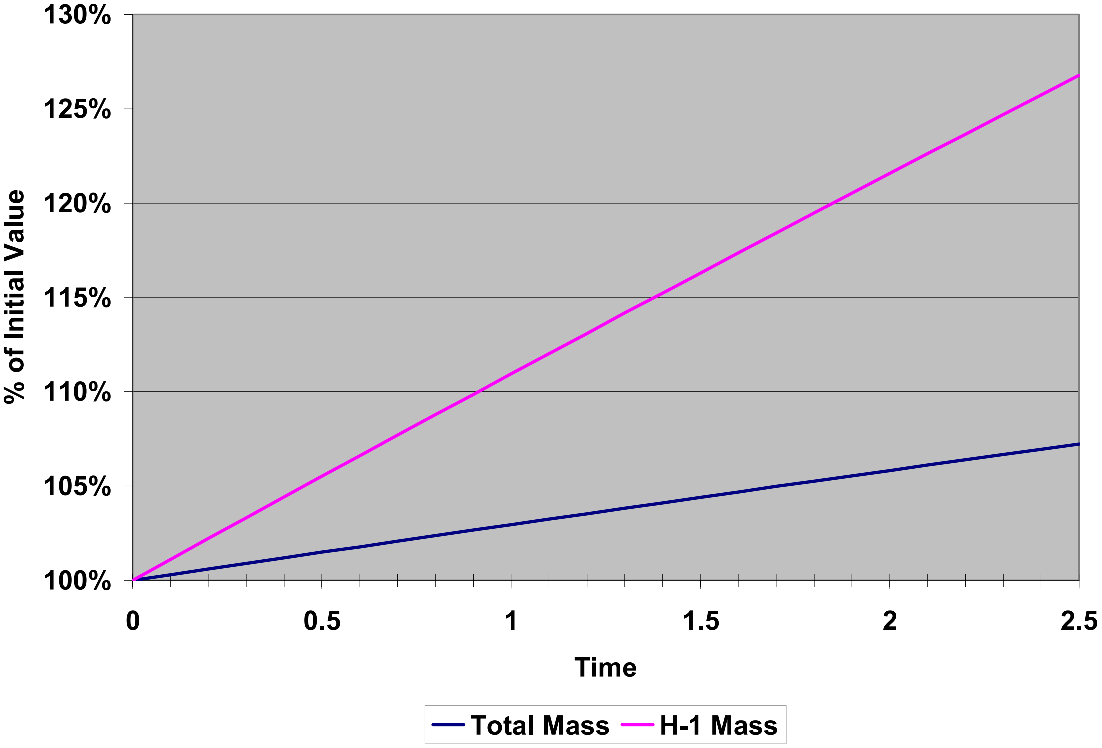

Figure 5.2. Relative change in total mass and ^{1}H mass for a simple initial 3% ^{1}H by mass.

5.3 Calculations and Theory

A long term experiment was performed to characterize the ability of the UT PGAA system to measure changes in the water concentration of a composite sample. A sample was dried and placed in a heated water bath. Sample mass was tracked gravimetrically as a function of time, and ^{1}H content was periodically measured using PGAA. The results were compared to show the effectiveness of each technique. A combination of gravimetric data and PGAA data were used to predict expected ^{1}H count rates for later measurements.

Data analysis begins with a variation of equation 3-8,

$$N_{H\text{-}1}=\frac{\dot{C}_{H\text{-}1}}{y_{2223\ keV\ H-1}V_{Beam}\sigma_{n,\gamma\ H-1\,0}\sqrt{E_0}\int\limits_E\int\limits_V\varepsilon_{2223\ keV}\left(x,y,z\right)\frac{\phi\left(x,y,z,E\right)}{\sqrt{E}}dVdE}\ . \qquad 5\text{-}1$$

The neutron flux distribution within the sample, and to a lesser extent the detection efficiency distribution, is not well known. To increase accuracy the neutron flux can be eliminated by ratio with other prompt gammas to obtain more precise results. Consider the boron peak at 477 keV,

$$\frac{N_{H\text{-}1}}{N_{B\text{-}10}}=\frac{\dfrac{\dot{C}_{H\text{-}1}}{y_{2223\ keV\ H-1}V_{Beam}\sigma_{n,\gamma\ H-1\,0}\sqrt{E_0}\int\limits_V\varepsilon_{2223\ keV}\left(x,y,z\right)\int\limits_E\frac{\phi\left(x,y,z,E\right)}{\sqrt{E}}dEdV}}{\dfrac{\dot{C}_{B\text{-}10}}{y_{477\ keV\ B-10}V_{Beam}\sigma_{n,\alpha\ B-10\,0}\sqrt{E_0}\int\limits_V\varepsilon_{477\ keV}\left(x,y,z\right)\int\limits_E\frac{\phi\left(x,y,z,E\right)}{\sqrt{E}}dEdV}}\ . \qquad 5\text{-}2$$

Detection efficiency varies only slightly throughout the sample volume, and acts to spatially weight the neutron flux in the integrals in equation 5-2. A spatially averaged efficiency can be treated as a constant and removed from the integral. Since the efficiency does not change significantly through the sample volume, this approximation will not introduce significant error. By removing the efficiency term from the integral, the neutron flux can be cancelled to yield

$$\frac{N_{H\text{-}1}}{N_{B\text{-}10}}=\frac{\dfrac{\dot{C}_{H\text{-}1}}{y_{2223\ keV\ H-1}V_{Beam}\sigma_{n,\gamma\ H-1\,0}\sqrt{E_0}\,\overline{\varepsilon_{2223\ keV}}\left(\int\limits_E\int\limits_V\frac{\phi\left(x,y,z,E\right)}{\sqrt{E}}dVdE\right)}}{\dfrac{\dot{C}_{B\text{-}10}}{y_{477\ keV\ B-10}V_{Beam}\sigma_{n,\alpha\ B-10\,0}\sqrt{E_0}\,\overline{\varepsilon_{477\ keV}}\left(\int\limits_E\int\limits_V\frac{\phi\left(x,y,z,E\right)}{\sqrt{E}}dVdE\right)}}$$

$$\frac{N_{H\text{-}1}}{N_{B\text{-}10}} = \frac{\dot{C}_{H\text{-}1} y_{477\ keV\ B-10} \sigma_{n,\alpha\ B-10 0} \overline{\varepsilon_{477\ keV}}}{\dot{C}_{B\text{-}10} y_{2223\ keV\ H-1} \sigma_{n,\gamma\ H-10} \overline{\varepsilon_{2223\ keV}}} \tag{5-3}$$

Relative comparisons between different irradiations at different water contents can be made by comparing $^{1}H/^{10}B$ ratios for each irradiation. All terms will cancel out except for the measured count rates, and error propagation will be minimized. The approximation to separate the flux and efficiency integral will also be removed.

To determine actual number densities, however, we will need to measure the flux and efficiency. This requires a sample with known concentrations of ^{1}H and ^{10}B. For estimates of actual number density, flux and efficiency were determined using an atomic absorption spectroscopy (AAS) standard solution of aqueous H_3BO_3 with a boron concentration of 1000 ± 10 μg/mL contained in a Teflon pocket designed to mimic composite sample geometry. The product of efficiency and flux for the ^{1}H and ^{10}B prompt gammas were determined through the following series of equations:

$$\dot{C}_{\text{H-1}_{\text{AAS}}} = V_{\text{AAS}} N_{\text{H-1}_{\text{AAS}}} \sigma_{\text{n},\gamma_{\text{H-1}}}\ y_{2223\,\text{keV}} (\varepsilon\varphi)_{\text{H}-1\text{AAS}}$$

$$(\varepsilon\varphi V)_{\text{H}-1\text{AAS}} = \frac{\dot{C}_{\text{H-1}_{\text{AAS}}}}{N_{\text{H-1}_{\text{AAS}}} \sigma_{\text{n},\gamma_{\text{H-1}}}\ y_{2223\,\text{keV}}} \tag{5-4}$$

$$(\varepsilon\varphi V)_{\text{B}-10\text{AAS}} = \frac{\dot{C}_{\text{B-10}_{\text{AAS}}}}{N_{\text{B-10}_{\text{AAS}}} \sigma_{\text{n},\alpha_{\text{B-10}}}\ y_{477\,\text{keV}}} \tag{5-5}$$

To apply equations 5-4 and 5-5 to the analysis of the composite coupons, the geometries and fluxes must be identical. This assumption is not entirely accurate, but will be sufficient to estimate ^{1}H density and gauge when discernable differences in PGAA measurements can be seen.

5.4 Experiment and Data

For these experiments, a composite sample cut from a hydrobust ring fabricated with YLA epoxy and Toray fibers was used. A sample with an initial mass of 3.0493 g as received from the UT-CEM was selected and designated CC4. The sample was baked at 105°C to remove all water absorbed from the ambient environment. Equilibrium was declared after the mass change was statistically insignificant over a 15 day period. The "dry equilibrium" mass was measured as 3.0406 g. While at dry equilibrium, a baseline PGAA measurement was taken for a 4 hour period.

ASTM standards for gravimetric measurements of water mass limit the time a sample can be removed from a controlled environment to five minutes, which is insufficient to obtain useful statistics for the ^{1}H radiative capture gamma. Four hours was chosen as a middle ground between a full day irradiation of eight hours and a five minute irradiation. As the gravimetric data will show, there are minimal mass changes during a four hour irradiation period and that the five minute ASTM time limit is somewhat arbitrary. Table 5.1 shows data for the baseline measurement. Upon completion of the baseline measurement, CC4 was placed in a water bath at 70°C.

Table 5.1. Data for Baseline Absorption Irradiation of CC4

^{10}B n,α (477.6 keV) area	694,000 ± 1000 counts
^{1}H n,γ (2223.3 keV) area	48,200 ± 200 counts
Measured ^{1}H/^{10}B ratio	0.0695 ± 0.0004
Mass Before Irradiation	3.0409 ± 0.0005 g
Mass After Irradiation	3.0413 ± 0.0005 g

Data from the baseline mass and irradiation was used to calculate the amount of water that must be absorbed to yield a statistically significant change in the PGAA measurements. To definitively detect a difference in water concentration, the $^{1}H/^{10}B$ ratio must increase several standard deviations [123]. The desired $^{1}H/^{10}B$ ratio on the second measurement is 0.0714. The developed equations were used to determine that the ^{1}H density must be increased by 5.7×10^{20} atoms/cm^{3} to increase the $^{1}H/^{10}B$ ratio to the desired value. Factoring in sample volume, and assuming a uniform distribution of absorbed water, it was estimated that the sample must absorb 13 mg of H_2O to achieve a confident change in the $^{1}H/^{10}B$ ratio. Figure 5.3 shows the mass history as measured while CC4 was absorbing water in the 70°C water bath.

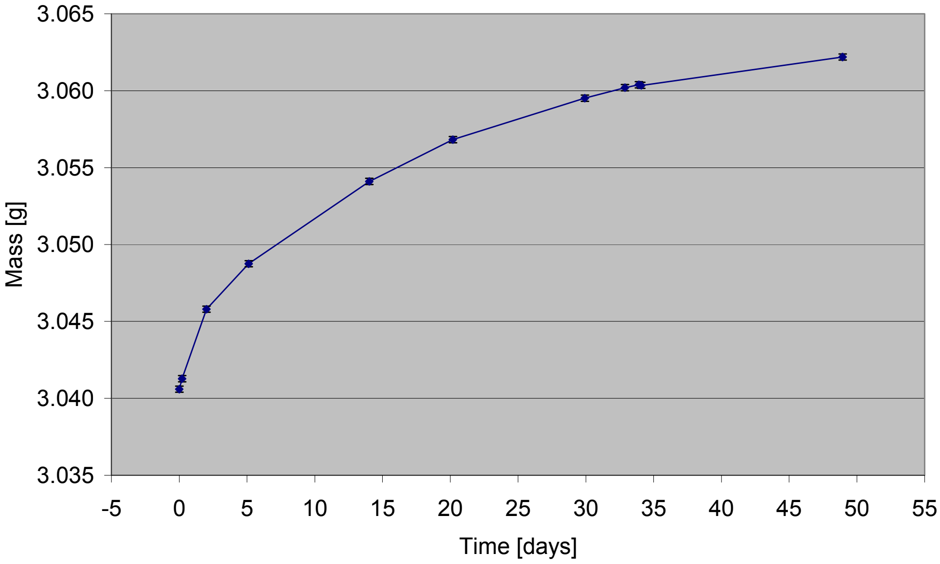

Figure 5.3. Sample mass as a function of time while immersed in 70° C water bath.

After 34 days, sample CC4 had absorbed 19.8 mg of H_2O, and a second PGAA irradiation was performed. Data for the irradiation is presented in Table 5.2. The addition of 19.8 mg of H_2O was expected to increase the $^{1}H/^{10}B$ ratio to 0.0720, which is excellent agreement with the newly measured ratio. The result serves to verify the calculation methods. It is also important to note that the raw number of counts for each prompt gamma are actually less during the second irradiation than for the first baseline irradiation. This emphasizes the need to remove the neutron flux from calculations based on different measurements. Figure 5.4 shows the relative change in sample mass and ^{1}H mass compared to the relative change in the ^{1}H/^{10}B ratio. ^{1}H mass is initially determined by PGAA measurements, but subsequent changes are calculated based on the measured mass change of the sample. Figure 5.4 shows close agreement between the measured and calculated ^{1}H/^{10}B ratio, as well as the ^{1}H mass measurements.

Table 5.2. Data for Second Absorption Irradiation of CC4

^{10}B (n,α) (477.6 keV) area	666,000 ± 1000 counts
^{1}H (n,γ) (2223.3 keV) area	48,000 ± 200 counts
Measured ^{1}H/^{10}B ratio	0.0721 ± 0.0004
Expected ^{1}H/^{10}B ratio	0.0720
Mass Before Irradiation	3.0604 ± 0.0005 g
Mass After Irradiation	3.0604 ± 0.0005 g

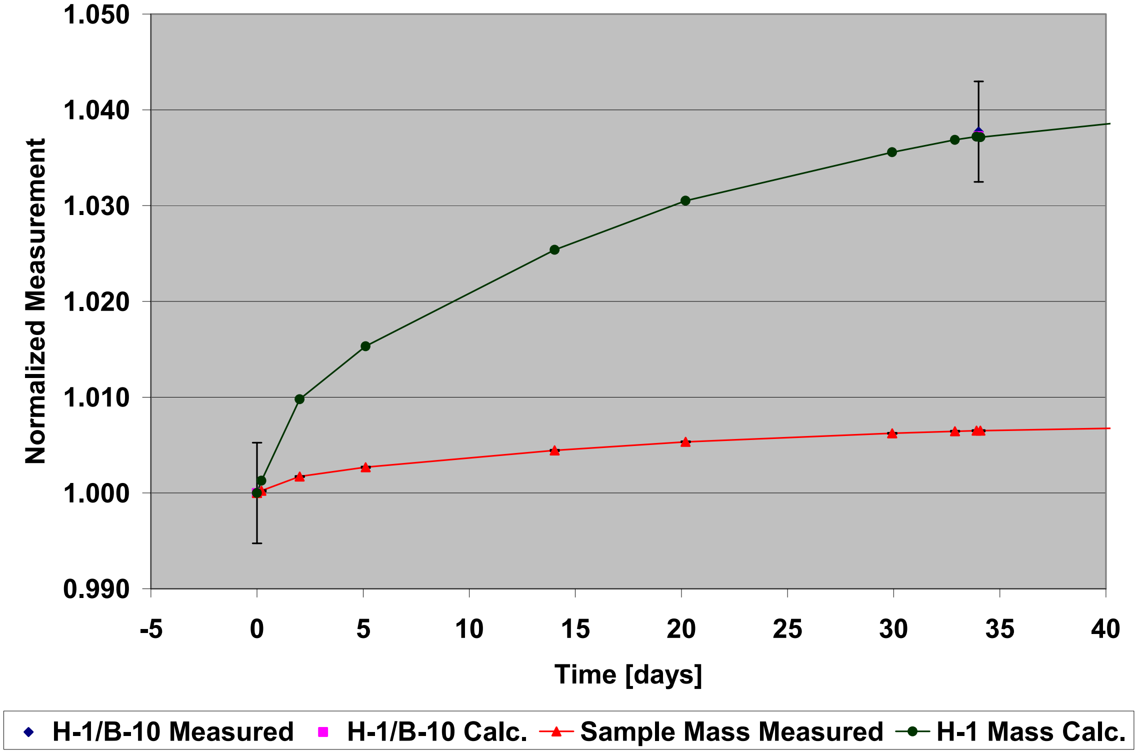

Figure 5.4. Relative mass compared to measured and calculated $^{1}H/^{10}B$ ratios as a function of time.

The water absorption experiment could not be continued due to the approaching saturation of sample CC4. Measurements were also delayed by equipment failures that resulted in the modifications to the detector crystal, detector position, and shielding configuration. Nearly 258 days elapsed between the initial baseline PGAA measurement and the start of desorption portion of the experiment.

The desorption experiment was performed after the detector was returned from service. The sample was removed from the 60°C water bath and a baseline PGAA measurement was taken. After the PGAA measurement, the sample was placed in an oven and baked at 70°C. Data from the desorption experiment is shown in Figure 5.5, Table 5.3, and Table 5.4. Measurements are normalized to the sample state at the start of desorption. The boron atomic absorption spectroscopy standard was irradiated to obtain a new efficiency flux value. Good agreement between the calculated changes in the ^{1}H

mass and $^{1}H/^{10}B$ ratio are found (better than 1%), although the measured $^{1}H/^{10}B$ ratio is slightly more than one standard deviation away from the expected value.

Table 5.3. Data for Baseline Desorption Irradiation of CC4

^{10}B n,α (477.6 keV) area	1,370,000 ± 1400 counts
^{1}H n,γ (2223.3 keV) area	103,000 ± 370 counts
Measured $^{1}H/^{10}B$ ratio	0.0749 ± 0.0004
Mass Before Irradiation	3.0657 ± 0.0005 g
Mass After Irradiation	3.0657 ± 0.0005 g

Table 5.4. Data for Second Desorption Irradiation of CC4

^{10}B n,α (477.6 keV) area	1,380,000 ± 1400 counts
^{1}H n,γ (2223.3 keV) area	101,000 ± 370 counts
Measured $^{1}H/^{10}B$ ratio	0.0732 ± 0.0003
Expected $^{1}H/^{10}B$ ratio	0.0736
Mass Before Irradiation	3.0537 ± 0.0005 g
Mass After Irradiation	3.0546 ± 0.0005 g

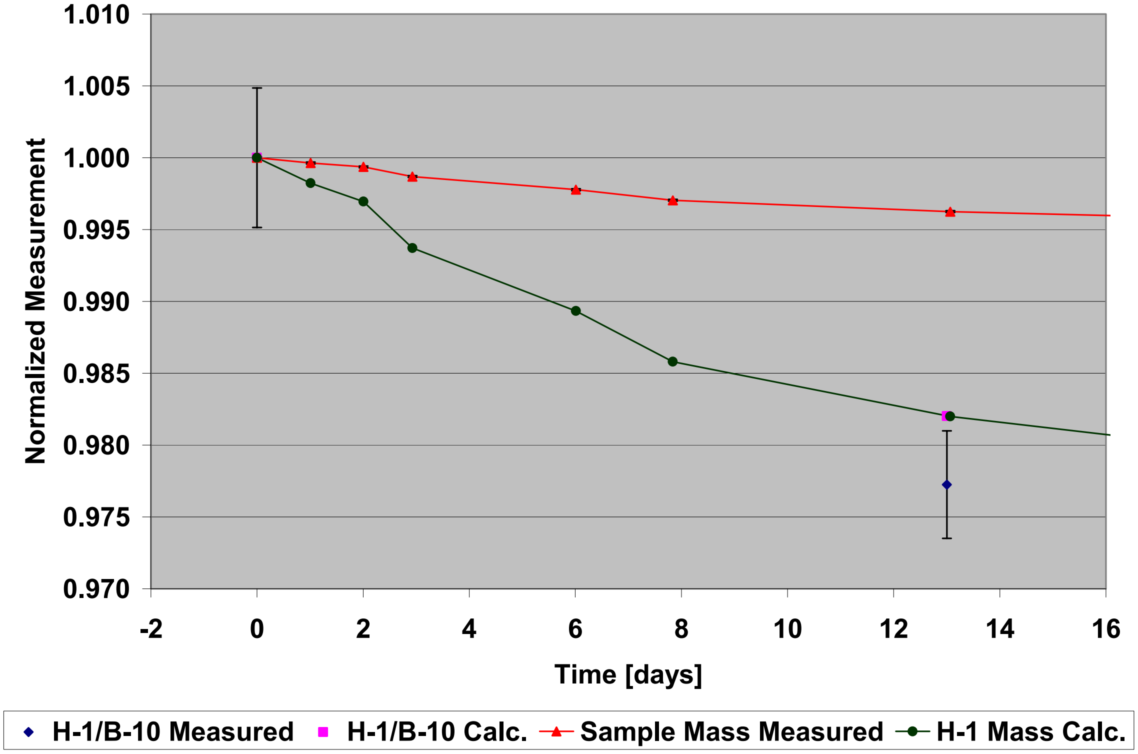

Figure 5.5. Normalized mass and ratio desorption curve.

5.5 Discussion

The measurement of small changes in the ^{1}H levels in the composite material is difficult due to the high ^{1}H background in the epoxy matrix; however, the measurements have shown that 1H mass can be determined with PGAA and it is expected that even better results would be determined using a higher flux system (like that available at NIST). Some discussion here will also be given to show other factors which could be altered to improve these measurements at even lower flux facilities. The measured ^{1}H peak area is actually the sum shown in equation 5-6,

$$C_{\mathrm{H-1\,measured}} = \left(C_{\mathrm{H-1\,epoxy}} + C_{\mathrm{H-1\,water}}\right)_{\mathrm{Sample}} + \left(C_{\mathrm{H-1\,shielding}} + C_{\mathrm{H-1\,humidity}} + C_{\mathrm{H-1\,misc}}\right)_{\mathrm{Background}} \quad 5\text{-}6$$

The difference between $C_{H\text{-}1,epoxy}$ and $C_{H\text{-}1,water}$ within the sample will ultimately limit the sensitivity of PGAA as a technique for the determination of water content within the sample. Sensitivity will decrease for a given irradiation time as the ^{1}H concentration in the epoxy increase, or as the epoxy volume itself increases. Background control is also a significant issue. Irradiations with no sample in place have shown minimal ^{1}H counts, and this data has been interpreted to mean that there is an insufficient amount of ^{1}H in the air to influence measurements on the composite samples. Of particular concern is the effect of ^{1}H in shielding materials and the scattering of neutrons into the shielding when samples are present.

PGAA measurements during the water absorption experiment yielded excellent agreement with changes in sample mass. This indicates that interference from the ^{1}H in the shielding is negligible as long as it is valid to assume that the absorbed water is distributed uniformly throughout the sample. PGAA measurements during the desorption experiment did not yield as good agreement, but the detector and detector shielding had been moved closer to the beam. It is expected that interference from ^{1}H in the shielding has become significant enough to influence ^{1}H measurements in the composite sample. This increased interference from shielding is only of minor significance since the calculation is still within the 95% confidence level of the measurement.

It is suspected that this technique will be more desirable when PGAA measurements are more precise than mass measurements, which is a difficult task considering the error on mass measurements can often be reduced to less than a milligram. Consider the mass of the sample, $3.0409 \pm 0.007\%$, during the baseline absorption measurement. The area of the ^{1}H peak was $4.8\times10^4 \pm 0.5\%$. To decrease the measured error to 0.007%, the area must increase by almost 4 orders of magnitude to 2.3×10^8 counts. The most practical way to increase the ^{1}H count rate is to perform the experiment at a facility with a higher neutron flux. To achieve 0.007% error in the ^{1}H peak area in a 4 hour time period, the flux must be increased by a factor of 4.8×10^3. For these experiments the 2200 m/s equivalent neutron flux averaged approximately 8.3×10^6 n/cm^2/s, as measured by the vanadium foil technique. The necessary flux to achieve the desired ^{1}H peak area with the current detection setup is 4×10^{10} n/cm^2/s. This can only be achieved using focused cold neutron beams at the NIST reactor, which can deliver peak fluxes of 5×10^{10} n/cm^2/s at focal points near 0.5 mm. With this flux, ^{1}H peak errors on the order of 0.006% could be obtained in 4 hours. After 30 minutes of irradiation time the peak error would be 0.02%, and after 5 minutes the peak error would be 0.04%. Such a neutron flux would make PGAA vastly superior to mass measurements on any sample less massive than 500 mg, while still meeting ASTM standards for sample treatment.

5.6 Conclusions

The measurement of water content in carbon fiber polymer matrix materials using PGAA is difficult at the UT-NETL in its current configuration. ASTM standards for sample treatment during gravimetric measurements could not be met while performing PGAA, although it has been shown that ASTM time limits are somewhat arbitrary and sample mass did not measurably change during PGAA irradiations. Measurements at the UT-NETL did not approach the sensitivity of gravimetric measurements, although PGAA was successfully shown to detect differences in ^{1}H content in a sample over time.

The potential advantages of PGAA technique for water content measurement have been verified. The data has shown that relative changes in the ^{1}H concentration are greater than relative changes in mass, so the potential for greater sensitivity using PGAA over gravimetric techniques still exists. Gravimetric measurements are also strictly bulk measurements, while PGAA using a well characterized, focused beam can be used to scan a material and potentially aid in observing diffusion of water into or out of a sample.

The ultimate conclusion of this experiment is that the UT-NETL PGAA system, in its current configuration, is well suited for performing water content measurements in carbon fiber polymer matrix composite materials. The primary difficultly is the control of background interference and the low flux nature of the 1 MW TRIGA reactor. Counting statistics could be improved by characterizing shielding materials and choosing those with minimal interference. Upgrading the TCNS will also enhance PGAA sensitivities, but the effective increase in neutron flux may still not allow the UT-NETL PGAA system to provide water content measurements of hydrogenous materials on a useful scale. It should however be noted that the UT-PGAA facility can be successfully used to detect water content in naturally non-hydrogenous materials with exceptional sensitivity (less than 0.5%).

CHAPTER 6. Fiber Volume Measurements

6.1 Introduction

Fibrous composite materials derive much of their strength from internal fibers. To accurately calculate the ultimate strength of a fibrous composite, the fiber volume must be determined. Standard methods for determining fiber volume are destructive. Acid digestion is the preferred method by ASTM [91], and the application of digital imagery to the examination of a cross sectional slice has also been reported [99]. Both methods require samples to be destroyed and cannot account for non-uniformities in manufactured materials. A non-destructive tool for fiber volume measurements would allow ultimate strength and fiber volume determination for a single ring, which is currently impossible due to the destructive nature of present test methods.

The UT-CEM uses acid digestion to determine fiber volume of hydroburst rings. A thin composite shell similar to a large pipe section is fabricated, and cut into approximately eleven rings for hydroburst testing. Typically, the center ring is set aside for acid digestion testing, and the determined fiber volume is assumed to be constant for all hydroburst rings. This assumption may not be valid. Consider Table 6.1 and Table 6.2, which contain the results of a series of hydroburst tests for two composite shells. Ultimate strengths predicted on the basis of fiber volume are generally accurate to within a few percent or better, but occasional rings deviate substantially from the calculated strengths. Deviations could be due to variations in the fiber volume. The development of a non-destructive tool for fiber volume measurement would allow the determination of fiber volume prior to destructive hydroburst testing on individual hoops.

Table 6.1. NRA HFHB1 Hydroburst Ring Data Provided by UT-CEM

Fibers	Toray T1000G
Tensile Modulus [GPa]	240
Tensile Strength [MPa]	6,370
Fiber Volume [Hoop 5]	72.66%
Hoop Modulus [GPa]	174

Hoop	Measured Strain	Calculated Ultimate Strength [MPa]	Measured Ultimate Strength [MPa]	% diff
2	0.016237	3469	3341	3.82%
4	0.013980	2986	3104	-3.78%
6	0.016089	3437	3314	3.70%
7	0.014559	3110	3167	-1.79%
8	0.017866	3817	3326	14.73%
9	0.014581	3115	3204	-2.78%
10	0.016168	3454	3379	2.22%
11	0.013468	2877	3184	-9.64%

Table 6.2. NRA HFHB2 Hydroburst Ring Data Provided by UT-CEM

Fibers	Toray T1000G
Tensile Modulus [GPa]	240
Tensile Strength [MPa]	6,370
Fiber Volume [Hoop 5]	72.76%
Hoop Modulus [GPa]	175

Hoop	Measured Strain	Calculated Ultimate Strength [MPa]	Measured Ultimate Strength [MPa]	% diff
1	0.016102	3444	3467	-0.66%
2	0.015599	3337	3429	-2.68%
3	0.016020	3427	3599	-4.79%
4	0.015656	3349	3378	-0.86%
6	0.016062	3436	3417	0.57%
7	0.016089	3442	3475	-0.95%
8	0.016339	3495	3304	5.80%
9	0.014915	3191	3435	-7.12%

Prompt gamma activation analysis can be used to non-destructively identify isotopes and elements within a sample. In a properly calibrated system, PGAA can be used to determine absolute quantities of isotopes and elements. The ratios of the constituents of a sample can be determined even more accurately. PGAA could be used to measure the constituents of polymer matrix carbon fiber composite samples. The ratios of isotopes contained only in the epoxy could be taken with isotopes that only appear in the carbon fibers. Changing ratios between different samples would be indicative of differences in fiber volume.

6.2 Calculations and Theory

6.2.1 Fiber Volume

Carbon fiber composites are heterogeneous materials. A typical unit cell is shown in Figure 6.1.

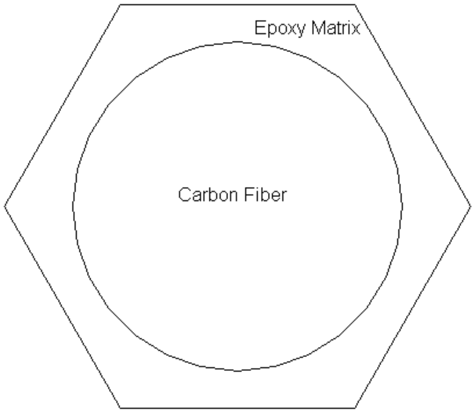

Figure 6.1. A typical unit cell for a carbon fiber in an epoxy matrix.

The carbon fibers are presumed to be pure graphite. Toray lists their T1000G fibers at a density of 1.80 g/cc. The composition of the epoxy matrix is unknown, but previous measurements and discussions with material suppliers have indicated the presence of carbon, hydrogen, oxygen, nitrogen, and sulfur. All can be detected with PGAA to some extent, but hydrogen, sulfur, and carbon are generally the simplest.

The number density of carbon in the fibers, $N_{C\,F}$, can be determined from the manufacturer supplied density of the fiber material. There will also be some number density of carbon in the epoxy, $N_{C\,E}$, as well as sulfur, $N_{H\,E}$, and hydrogen, $N_{S\,E}$. PGAA can be used to measure number densities of elements and isotopes within a composite sample. Because the epoxy contains different isotopes than the fiber, the bulk measurements can be unfolded to determine the heterogeneity of the material. The inherent relation of the bulk PGAA measurements to the fiber volume makes PGAA useful for non-destructive fiber volume measurement. The PGAA measurement of carbon, sulfur, and hydrogen density will be related to the fiber and epoxy volumes as

$$N_{C\,PGAA}\left(V_F + V_E\right) = N_{C_F} V_F + N_{C\,E} V_E\,, \tag{6-1}$$

$$N_{S\,PGAA}\left(V_F + V_E\right) = N_{S\,E} V_E\,, \tag{6-2}$$

$$N_{H\,PGAA}\left(V_F + V_E\right) = N_{H\,E} V_E\,, \tag{6-3}$$

where $N_{C\,PGAA}$, $N_{S\,PGAA}$, and $N_{H\,PGAA}$ are the bulk atomic densities for carbon, sulfur, and hydrogen, respectively, V_F is the fiber volume, and V_E is the epoxy volume. $V_F + V_E$ is equal to the total sample volume.

Given a perfect material with no voids, the total sample volume is just the sum of the fiber volume and epoxy volume. We can rearrange the equations in terms of percent fiber volume, v_F, and percent epoxy volume, v_E,

$$v_F = \frac{V_F}{V_F + V_E}\,,$$

$$v_E = \frac{V_E}{V_F + V_E},$$

$$v_E + v_F = 1.$$

$$N_{C\,PGAA} = N_{C_F} v_F + N_{C\,E}\left(1 - v_F\right) \qquad 6\text{-}4$$

$$N_{S\,PGAA} = N_{S\,E}\left(1 - v_F\right) \qquad 6\text{-}5$$

$$N_{H\,PGAA} = N_{H\,E}\left(1 - v_F\right) \qquad 6\text{-}6$$

The left hand side of each equation will be measured, but there are potentially 5 unknowns on the right hand side. The atomic density of carbon in the fibers, $N_{C\,F}$, can be determined from the density of the fibers, which is a known quantity, leaving us with 4 unknowns on the right hand side. If the epoxy matrix contained no ^{12}C, equation 6-4 could be directly solved for the fiber content. To account for the ^{12}C content in the epoxy, a calibration point is required. Either the number density of ^{1}H or ^{32}S in the epoxy must be determined independently, or the percent volume of the matrix or reinforcement must be measured. For this experiment, we will acid digest the samples after irradiation to determine the volumes. By rearranging the equations, we can calculate the concentration of the constituents of the epoxy according to

$$N_{C\,E} = \frac{N_{C_F} v_F - N_{C\,PGAA}}{v_E}, \qquad 6\text{-}7$$

$$N_{S\,E} = \frac{N_{S\,PGAA}}{v_E}, \qquad 6\text{-}8$$

$$N_{H\,E} = \frac{N_{H\,PGAA}}{v_E}. \qquad 6\text{-}9$$

Once the ^{1}H, ^{32}S, and ^{12}C concentrations are determined for a given epoxy and fiber, epoxy and fiber volumes can be calculated for other samples fabricated from the same materials.

6.2.2 PGAA Analysis

The first step towards determining sample fiber volumes will be to determine bulk sample isotopic number densities. The procedure described in Chapter 3 for a planar source will be used. Recall equation 3-21, rearranged to determine number density,

$$N = \frac{c(E_\gamma)}{y(E_\gamma)\left[\sum_{i=1}^{I} \Delta V_i \varepsilon_i(E_\gamma)\sigma_{\gamma 2200}\Phi_{i2200_{EQ}}\right]}. \qquad 6\text{-}10$$

The spatial flux for each composite coupon sample was mapped with a cadmium sample to determine the fluence delivered to each flux channel according to equation 3-22. Equation 5-10 can be further simplified, performing the summation, to

$$N = \frac{c(E_\gamma)}{y(E_\gamma)\sigma_{\gamma 2200} V_\Sigma \overline{\varepsilon_i(E_\gamma)}\,\overline{\Phi}_{i2200_{EQ}}}, \qquad 6\text{-}11$$

where ε and Φ are average values, and V_Σ is the volume over which the summation was made. All the terms on the right hand side of equation 6-11 are known or measured, with different degrees of accuracy. If number densities of ^{1}H, ^{32}S, and ^{12}C were known within the epoxy, equation 6-11 in combination with equation 6-4, 6-5, or 6-6, would be sufficient to determine the fiber volume of unknown samples (provided they were fabricated from known materials). This information can only be acquired through measurements on a sample of known fiber volume. Alternatively, the ratio method discussed in 3.4 can be used to make relative determinations about differences in fiber volumes between samples.

Let us consider a case for samples fabricated from carbon fibers and an epoxy matrix that contains ^{1}H, but no ^{12}C. For this sample, the atomic density of carbon could be determined using equation 6-11 and the fiber volume could be determined from equation 6-4 (since there is no ^{12}C in this epoxy, $N_{C_E} = 0$). Alternatively, ratios can be applied to remove quantities that are not well known and reduce error. Let us consider the case of ^{1}H and ^{12}C in ratio,

$$\frac{N_{H\,PGAA}}{N_{C\,PGAA}} = \frac{\dfrac{\dot{C}_{2223.3}}{y_{2223.3} V_{beam} \sigma_{n,\gamma H0} \overline{\varepsilon\Phi}}}{\dfrac{\dot{C}_{1261.7}}{y_{1261.7} V_{beam} \sigma_{n,\gamma C0} \overline{\varepsilon\Phi}}},$$

$$\frac{N_{C_F} v_F}{N_{H_E} v_E} = \frac{\dfrac{\dot{C}_{1261.7}}{y_{1261.7} \sigma_{n,\gamma C0} \overline{\varepsilon_{1261.7}}}}{\dfrac{\dot{C}_{2223.3}}{y_{2223.3} \sigma_{n,\gamma H0} \overline{\varepsilon_{2223.3}}}},$$

$$\frac{N_{C_F} v_F}{N_{H_E}(1 - v_F)} = \frac{\dot{C}_{1261.7} y_{2223.3} \sigma_{n,\gamma H0} \overline{\varepsilon_{2223.3}}}{\dot{C}_{2223.3} y_{1261.7} \sigma_{n,\gamma C0} \overline{\varepsilon_{1261.7}}},$$

$$\frac{N_{C_F} v_F}{N_{H_E}(1 - v_F)} = \frac{\dot{C}_{1261.7} y_{2223.3} \sigma_{n,\gamma H0} \overline{\varepsilon_{2223.3}}}{\dot{C}_{2223.3} y_{1261.7} \sigma_{n,\gamma C0} \overline{\varepsilon_{1261.7}}}. \qquad \text{6-12}$$

The ^{1}H content of the epoxy must be known to solve equation 6-12 for fiber volume. For the samples analyzed in this investigation, such information is unavailable and further ratios must be taken to remove the ^{1}H density from calculations. Consider the ratio of equation 6-12 with itself using measurements from two composite samples of the same geometry and materials, A and B,

$$\frac{\dfrac{N_{C_F} v_{F\,A}}{N_{H\,E}\left(1-v_{F\,A}\right)}}{\dfrac{N_{C_F} v_{F\,B}}{N_{H\,E}\left(1-v_{F\,B}\right)}}=\frac{\dfrac{\dot{C}_{1261.7\,A}\,y_{2223.3}\,\sigma_{n,\gamma\,H\,0}\,\overline{\varepsilon_{2223.3\,A}}}{\dot{C}_{2223.3\,A}\,y_{1261.7}\,\sigma_{n,\gamma\,C\,0}\,\overline{\varepsilon_{1261.7\,A}}}}{\dfrac{\dot{C}_{1261.7\,B}\,y_{2223.3}\,\sigma_{n,\gamma\,H\,0}\,\overline{\varepsilon_{2223.3\,B}}}{\dot{C}_{2223.3\,B}\,y_{1261.7}\,\sigma_{n,\gamma\,C\,0}\,\overline{\varepsilon_{1261.7\,B}}}},$$

$$\frac{N_{C_F} v_{F\,A} N_{H\,E}\left(1-v_{F\,B}\right)}{N_{H\,E}\left(1-v_{F\,A}\right) N_{C_F} v_{F\,B}}=\frac{\dot{C}_{1261.7\,A}\,y_{2223.3}\,\sigma_{n,\gamma\,H\,0}\,\overline{\varepsilon_{2223.3\,A}}\,\dot{C}_{2223.3\,B}\,y_{1261.7}\,\sigma_{n,\gamma\,C\,0}\,\overline{\varepsilon_{1261.7\,B}}}{\dot{C}_{2223.3\,A}\,y_{1261.7}\,\sigma_{n,\gamma\,C\,0}\,\overline{\varepsilon_{1261.7\,A}}\,\dot{C}_{1261.7\,B}\,y_{2223.3}\,\sigma_{n,\gamma\,H\,0}\,\overline{\varepsilon_{2223.3\,B}}}. \qquad \text{6-13}$$

Since both samples are of the geometry and material, efficiencies and number densities will cancel, leaving

$$\frac{v_{F\,A}\left(1-v_{F\,B}\right)}{v_{F\,B}\left(1-v_{F\,A}\right)}=\frac{\dot{C}_{1261.7\,A}\dot{C}_{2223.3\,B}}{\dot{C}_{2223.3\,A}\dot{C}_{1261.7\,B}},$$

$$\frac{\dfrac{v_{F\,A}}{1-v_{F\,A}}}{\dfrac{v_{F\,B}}{1-v_{F\,B}}}=\frac{\dot{C}_{1261.7\,A}\dot{C}_{2223.3\,B}}{\dot{C}_{2223.3\,A}\dot{C}_{1261.7\,B}}. \qquad \text{6-14}$$

Equation 6-14 is still under-defined, although a relative comparison of sample fiber volumes is possible. A more useful implication of equation 6-14 is that if the fiber volume of any sample is known, it can be used as a standard comparator to determine the fiber volume of other samples using

$$v_{F\,A}=\frac{\dfrac{\dot{C}_{1261.7\,A}\dot{C}_{2223.3\,B}}{\dot{C}_{2223.3\,A}\dot{C}_{1261.7\,B}}\,\dfrac{v_{F\,B}}{1-v_{F\,B}}}{\left(\dfrac{\dot{C}_{1261.7\,A}\dot{C}_{2223.3\,B}}{\dot{C}_{2223.3\,A}\dot{C}_{1261.7\,B}}\,\dfrac{v_{F\,B}}{1-v_{F\,B}}+1\right)}. \qquad \text{6-15}$$

For the composite samples under investigation, the matrix and reinforcement share a common element, carbon. Although the composition of the carbon fibers is well known, there is no quantitative data available for the epoxy matrix and equation 6-4 cannot be solved directly for fiber volume; however, ratios of PGAA measurements can still be used to determine sample fiber volume. Consider the ratio of equation 6-11 for the case where the epoxy matrix contains ^{12}C

$$\frac{N_{H\,PGAA}}{N_{C\,PGAA}}=\frac{\dfrac{\dot{C}_{2223.3}}{y_{2223.3}V_{beam}\sigma_{n,\gamma\,H\,0}\overline{\varepsilon\Phi}}}{\dfrac{\dot{C}_{1261.7}}{y_{1261.7}V_{beam}\sigma_{n,\gamma\,C\,0}\overline{\varepsilon\Phi}}},$$

$$\frac{N_{C_F}v_F+N_{C\,E}v_E}{N_{H\,E}v_E}=\frac{\dfrac{\dot{C}_{1261.7}}{y_{1261.7}\sigma_{n,\gamma\,C\,0}\overline{\varepsilon_{1261.7}}}}{\dfrac{\dot{C}_{2223.3}}{y_{2223.3}\sigma_{n,\gamma\,H\,0}\overline{\varepsilon_{2223.3}}}},$$

$$\frac{N_{C_F}v_F}{N_{H\,E}\left(1-v_F\right)}+\frac{N_{C\,E}}{N_{H\,E}}=\frac{\dot{C}_{1261.7}y_{2223.3}\sigma_{n,\gamma\,H\,0}\overline{\varepsilon_{2223.3}}}{\dot{C}_{2223.3}y_{1261.7}\sigma_{n,\gamma\,C\,0}\overline{\varepsilon_{1261.7}}}. \qquad 6\text{-}16$$

Again, as for equation 6-12, if the characteristics of the epoxy were well known, equation 6-16 could be solved for fiber volume. If a solid block of epoxy was obtained and the ratio of ^{12}C to ^{1}H within the epoxy was determined, equation 6-16 could be manipulated just as easily as 6-12. Unfortunately, such a sample is not available. Equation 6-16 can be taken in ratio for two samples, *A* and *B*, to remove unknown terms and make a relative comparison of fiber volumes.

$$\frac{\dfrac{N_{C_F}v_{F\,A}+N_{C\,E}v_{E\,A}}{N_{H\,E}v_{E\,A}}}{\dfrac{N_{C_F}v_{F\,B}+N_{C\,E}v_{E\,B}}{N_{H\,E}v_{E\,B}}}=\frac{\dfrac{\dot{C}_{1261.7\,A}y_{2223.3}\sigma_{n,\gamma\,H\,0}\overline{\varepsilon_{2223.3\,A}}}{\dot{C}_{2223.3\,A}y_{1261.7}\sigma_{n,\gamma\,C\,0}\overline{\varepsilon_{1261.7\,A}}}}{\dfrac{\dot{C}_{1261.7\,B}y_{2223.3}\sigma_{n,\gamma\,H\,0}\overline{\varepsilon_{2223.3\,B}}}{\dot{C}_{2223.3\,B}y_{1261.7}\sigma_{n,\gamma\,C\,0}\overline{\varepsilon_{1261.7\,B}}}},$$

$$v_{FA} = \frac{\frac{N_{CE}}{N_{C_F}}\left(1-\frac{\dot{C}_{1261.7B}\dot{C}_{2223.3A}}{\dot{C}_{2223.3B}\dot{C}_{1261.7A}}\right)+\frac{v_{FB}}{(1-v_{FB})}}{\frac{\dot{C}_{1261.7B}\dot{C}_{2223.3A}}{\dot{C}_{2223.3B}\dot{C}_{1261.7A}}+\frac{N_{CE}}{N_{C_F}}\left(1-\frac{\dot{C}_{1261.7B}\dot{C}_{2223.3A}}{\dot{C}_{2223.3B}\dot{C}_{1261.7A}}\right)+\frac{v_{FB}}{(1-v_{FB})}}\,. \qquad 6\text{-}17$$

Equation 6-17 can be used to calculate the fiber volume of a sample provided that the fiber volume of another sample and the carbon content of the epoxy are known. For the case where $N_{CE} = 0$, equation 6-17 reduces to equation 6-15. Although equation 6-17 contains two unknowns, a fiber volume range can be calculated based on the possible range of N_{CE}. Also, given two samples of known fiber volume, equation 6-17 can be rearranged to solve for the ^{12}C content of the epoxy, as shown by

$$N_{CE} = \frac{N_{C_F}\left[\frac{\dot{C}_{1261.7A}\dot{C}_{2223.3B}}{\dot{C}_{2223.3A}\dot{C}_{1261.7B}}\frac{v_{FB}}{(1-v_{FB})}-\frac{v_{FA}}{(1-v_{FA})}\right]}{1-\frac{\dot{C}_{1261.7A}\dot{C}_{2223.3B}}{\dot{C}_{2223.3A}\dot{C}_{1261.7B}}}\,. \qquad 6\text{-}18$$

PGAA analysis of composite samples to determine fiber volume is complex, and requires known standards. Although initial fiber volume measurements have been provided by the UT-CEM for hydroburst samples (see Table 6.1 and Table 6.2), true standards do not currently exist.

6.3 Relative Comparison of Hydroburst Rings

The fiber volume experiment was initially performed with two hydroburst rings obtained from the UT-CEM, labeled NRA HFHB1 #1 and NRA HFHB2 #11. These rings will be referred to as hoop *A* and hoop *B*, respectively. Each hoop was cut into 16 arcs approximately 10 cm in length. PGAA irradiations were performed to analyze the ^{12}C, ^{1}H, and ^{32}S content. Carbon is clearly important, because we are concerned about the volume of carbon fibers. Hydrogen will be found primarily in the epoxy, but interferences due to water absorption, humidity, and the presence of hydrogenous shielding may influence the results. Sulfur, on the other hand, is also present in the epoxy and is not subject to potential interference.

Irradiation times were based on the desire to obtain better than 1% accuracy in ^{12}C peak areas. After a baseline irradiation was performed, it was estimated that approximately 40 hours of integrated irradiation time would be required to achieve the desired statistical precision. To reduce the irradiation time, it was decided that 3 test coupons would be clamped together to increase the volume of the sample, and total number of atoms within the sample, exposed to the beam. The goal of clamping samples together was to effectively triple the radiative capture reaction rate and reduce the required counting time by the square root of 3, to roughly 23 hours. Samples were also held vertically, to maximize beam usage.

Table 6.3 contains the coupon characteristics for samples A2-A4, and B1-B3. Coupons from hoop A were irradiated in the clamped position first. The selected samples were designated A2, A3, and A4, respectively. Sample A1 was used for the baseline irradiation time estimates. The clamped sample, dubbed A234, was irradiated for a total of just over 22.5 hours during three separate irradiations at 950 kW spread over 3 consecutive days. Table 6.4 contains peak area data for each irradiation. For comparison, 3 coupon samples from hoop B were clamped and irradiated in the same position (data shown in Table 6.5). As for sample A234, sample B123 was irradiated for a combined 23 hours at 950 kW over 3 consecutive days.

Table 6.3. Hydroburst Ring Sample Characteristics

Sample	Length [mm]	Width [mm]	Thickness [mm]	Mass [g]
A2	96 ± 0.5	12.40 ± 0.005	2.10 ± 0.005	4.03256 ± 0.0002
A3	95 ± 0.5	12.40 ± 0.005	2.10 ± 0.005	4.07247 ± 0.0002
A4	95 ± 0.5	12.39 ± 0.005	2.09 ± 0.005	4.01715 ± 0.0002
B1	95 ± 0.5	12.39 ± 0.005	2.03 ± 0.005	3.84381 ± 0.0002
B2	98 ± 0.5	12.34 ± 0.005	2.01 ± 0.005	3.90770 ± 0.0002
B3	95 ± 0.5	12.36 ± 0.005	2.04 ± 0.005	3.83939 ± 0.0002
	Fiber Density	1.80 g/cm^3	Epoxy Density	1.30 g/cm^3

Table 6.4. Data for A234 Irradiations.

	Day 1	Day 2	Day 3
HPGe Live Time	27312.98 s	39600.00 s	14400.00 s
^{3}He CPS	491.14 ± 0.03%	477.92 ± 0.02%	465.66 ± 0.04%
Peak [keV]	Peak Area		
^{32}S (n,γ) 840.993(13)	26472 ± 378	36623 ± 256	12584 ± 152
^{12}C (n,γ) 1261.765(9)	12265 ± 297	17395 ± 203	5886 ± 120
^{1}H (n,γ) 2223.25	353167 ± 674	493019 ± 728	176480 ± 434

Table 6.5. Data for B123 Irradiations.

	Day 1	Day 2	Day 3
HPGe Live Time	14400.00 s	39600.00 s	28800.00 s
^{3}He CPS	510.77 ± 0.04%	473.99 ± 0.02%	456.94 ± 0.03%
Peak [keV]	Peak Area		
^{32}S (n,γ) 840.993(13)	15398 ± 167	40555 ± 272	29654 ± 230
^{12}C (n,γ) 1261.765(9)	7393 ± 133	18560 ± 214	13664 ± 180
^{1}H (n,γ) 2223.25	215132 ± 482	573354 ± 786	406090 ± 661

Table 6.6. Summed Hydroburst Ring Measurements Corrected for Flux Variations

	Hoop A	Hoop B
^{32}S n,γ (841 keV)	0.862 ± 0.007 CPS	1.072 ± 0.007 CPS
^{12}C n, γ (1262 keV)	0.404 ± 0.006 CPS	0.473 ± 0.006 CPS
^{1}H n, γ (2223.3 keV)	12.11 ± 0.01 CPS	14.65 ± 0.01 CPS
$^{12}C/^{32}S$	0.469 ± 0.008	0.441 ± 0.004
$^{12}C/^{1}H$	0.033 ± 0.000	0.032 ± 0.000
$[^{12}C/^{32}S]/[^{12}C/^{32}S]_A$	1	0.94 ± 0.02
$[^{12}C/^{1}H]/[^{12}C/^{1}H]_A$	1	0.97 ± 0.02
UT-CEM Fiber Volume	72.6%	72.7%

Table 6.6 shows summed measurements corrected for flux variations. The relative comparison of count rates shows that the ^{12}C to ^{32}S and ^{12}C to ^{1}H ratios are only slightly different between the samples. This is generally consistent with the UT-CEM fiber volume measurements, which show the samples to have almost identical fiber volumes. The PGAA data shows that there is slightly more ^{12}C per ^{32}S and ^{1}H in sample A234 than in sample B123, indicating a slightly higher fiber volume in sample A234.

To gauge the effectiveness of PGAA for fiber volume determination, sample A234 was treated as a standard and used with equation 5-17 to calculate the fiber volume of sample B123. Using the epoxy density of 1.30 g/cm^3, a range of potential ^{12}C densities for the epoxy can be calculated. The maximum ^{12}C atomic density physically possible in the epoxy is 6.52×10^{23} atoms/cm^3, for the case where the epoxy is composed entirely of ^{12}C. If the epoxy were composed entirely of ^{12}C, the fiber volume of sample B123 is calculated as 71.1% ± 0.5%. The minimum concentration of ^{12}C physically possible in the epoxy is simply zero atoms/cm^3. For the case of no ^{12}C in the epoxy, the fiber volume of sample B123 is calculated to be 71.5% ± 0.2%. Even though the ^{12}C content of the epoxy is unknown, the calculated range of potential fiber volumes is reasonably precise. Figure 6.2 shows the atomic density of ^{12}C in the epoxy plotted using equation 5-18 versus the fiber volume of sample B123. The allowable fiber volume range is indicated on the plot.

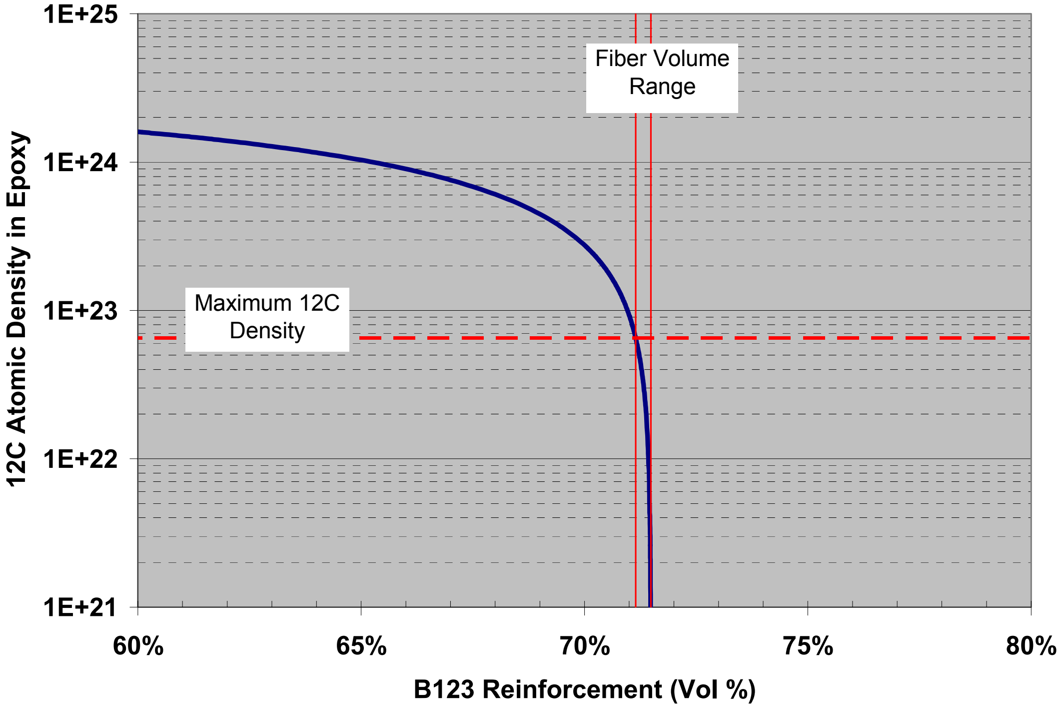

Figure 6.2. Range of possible fiber volumes for sample B123.

The fiber volume for B123 determined with PGAA, approximately 71.3%, matches reasonably well with the UT-CEM measurement of 72.7% listed in Table 6.6. PGAA measurements also call into question the accuracy of the UT-CEM measurement and indicate that hoop *B* has a lower fiber volume than hoop *A*. The UT-CEM fiber volumes for hoop *A* and hoop *B* inserted into equation 5-18 yield an atomic density of ^{12}C in the epoxy as $N_{CE} = (-2.6 \pm 0.7)\times10^{23}$ atoms/cm^3. The negative calculation indicates the data input into the equation is incorrect. This supports the PGAA measurement that the fiber volume of hoop *A* is greater than the fiber volume of hoop *B*.

6.4 Comparison of Hydroburst Ring and Flat Panel

The UT-CEM provided a third set of samples for fiber volume testing that were fabricated from Toray T1000G fibers and Cytec 977-2 resin, and believed to be in the range of 60% - 65% fiber volume. Unfortunately, the only samples available of the same material were flat panel samples, with the properties listed in Table 6.7. The flat samples are roughly half the thickness and twice the width of the hydroburst coupons. Six samples were stacked together to approximate the same thickness as three of the stacked hydroburst coupons.

Table 6.7. Flat Sample Properties

Sample	Length [mm]	Width [mm]	Thickness [mm]	Mass [g]
F1	101.61 ± 0.005	25.57 ± 0.005	1.05 ± 0.005	4.35 ± 0.0002
F2	101.67 ± 0.005	25.41 ± 0.005	1.15 ± 0.005	4.54 ± 0.0002
F3	101.52 ± 0.005	25.25 ± 0.005	1.17 ± 0.005	4.60 ± 0.0002
F4	101.42 ± 0.005	25.37 ± 0.005	1.15 ± 0.005	4.54 ± 0.0002
F5	101.40 ± 0.005	25.35 ± 0.005	1.08 ± 0.005	4.54 ± 0.0002
F6	101.38 ± 0.005	25.30 ± 0.005	1.10 ± 0.005	4.54 ± 0.0002

Samples A234 and sample FS1-6 were each irradiated over the course of 6 days for 23 hours each. The summed results are shown in Table 6.8. A relative comparison with ratios to eliminate flux variation indicates a significant difference in fiber volume, as expected by the estimated fiber volume for the flat samples.

The extra width and lack of sample curvature present a significant difference in geometry between the panel and hydroburst coupons. The average prompt gamma detection efficiencies will be different for each sample, as will the total neutron exposure. For quantitative calculations to be possible, the variations individual to each sample must be determined.

Table 6.8. Summed Measurements Corrected for Flux Varitions

	Hoop A	Flat Samples
^{32}S n,γ (841 keV)	0.862 ± 0.007 CPS	1.560 ± 0.006 CPS
^{12}C n, γ (1262 keV)	0.404 ± 0.006 CPS	0.584 ± 0.008 CPS
^{1}H n, γ (2223.3 keV)	12.11 ± 0.01 CPS	23.46 ± 0.02 CPS
$^{12}C/^{32}S$	0.469 ± 0.008	0.374 ± 0.005
$^{12}C/^{1}H$	0.0334 ± 0.0005	0.0249 ± 0.0004
$[^{12}C/^{32}S]/[^{12}C/^{32}S]_A$	1	0.80 ± 0.02
$[^{12}C/^{1}H]/[^{12}C/^{1}H]_A$	1	0.74 ± 0.02
Estimated Fiber Volume	72.6%	~ 60% – 65%

6.4.1 Efficiency and Flux Mapping

To make quantitative calculations, the spatial variations of the flux and detection efficiency were determined. As in the previous flux mapping experiment described in section 4.5, a Cd sample was irradiated at different locations on the grid to determine a flux profile. The ^{152}Eu source was also counted at several locations to determine an efficiency profile. The grid was set up with 0.25 cm × 0.25 cm resolution on each sample, as shown in Figure 6.3.

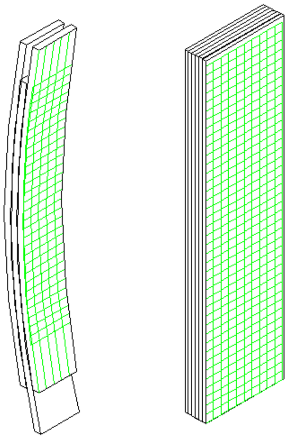

Figure 6.3. Flux and efficiency profiling grids for flat and curved samples.

The atomic densities for ^{12}C, and ^{1}H and ^{32}S were calculated based on PGAA measurements coupled with Cd data using equation 5-10. Atomic densities are shown in Table 6.9. The atomic density for ^{12}C in the epoxy was calculated based on the UT-CEM fiber volume of A234 according to

$$N_{CE} = \frac{N_{C\,PGAA} - N_{CF} v_f}{1 - v_f}. \qquad 6\text{-}19$$

The fiber volume for sample FS1-6 was then calculated as

$$v_f = \frac{N_{C\,PGAA} - N_{CE}}{N_{CF} - N_{CE}}. \qquad 6\text{-}20$$

The high fiber volume of sample A234 also leads to the propagation of substantial error in the numerator of equation 6-19. A low fiber volume sample is required to obtain better statistics for the ^{12}C content of the epoxy. Propagation of error issues underscore the need for ratios to eliminate poorly known quantities, and the proper selection of test coupon fiber volumes.

Table 6.9. Calculated Atomic Densities and Fiber Volume

	FS1-6	A234
$N_{C\,PGAA}$ ^{12}C [atoms/cm^3]	$(5.5 \pm 0.2)\times10^{22}$	$(7.6 \pm 0.3)\times10^{22}$
$N_{H\,PGAA}$ ^{1}H [atoms/cm^3]	$(1.35 \pm 0.05)\times10^{22}$	$(1.38 \pm 0.05)\times10^{22}$
$N_{S\,PGAA}$ ^{32}S [atoms/cm^3]	$(3.9 \pm 0.1)\times10^{20}$	$(4.2 \pm 0.2)\times10^{20}$
$N_{C\,F}$ ^{12}C [atoms/cm^3]	$(9.03 \pm 0.03)\times10^{22}$	$(9.03 \pm 0.03)\times10^{22}$
$N_{C\,E}$ ^{12}C [atoms/cm^3]	$(3.8 \pm 1.1)\times10^{22}$	$(3.8 \pm 1.1)\times10^{22}$

6.4.2. Relative Comparison

The direct calculations in section 5.4.1 lead to values with error bars too large to be useful. The ratio technique used to compare the hydroburst rings can also be applied to the comparison of a ring and the flat panels. Because of different geometries, the efficiencies will not necessarily cancel out, as for equation 6-18. The atomic density of ^{12}C in the epoxy for the flat samples is calculated as a function of the flat sample fiber volume according to equation 5-23, and plotted in Figure 6.4.

$$N_{C\,E} = \frac{\dfrac{\dot{C}_{1261.7\,A}\overline{\varepsilon_{2223.3\,A}}\dot{C}_{2223.3\,FS}\overline{\varepsilon_{1261.7\,FS}}}{\dot{C}_{2223.3\,A}\overline{\varepsilon_{1261.7\,A}}\dot{C}_{1261.7\,FS}\overline{\varepsilon_{2223.3\,FS}}} N_{C_F} v_{F\,FS} v_{E\,A} - N_{C_F} v_{F\,A} v_{E\,FS}}{v_{E\,A} v_{E\,FS} - \dfrac{\dot{C}_{1261.7\,A}\overline{\varepsilon_{2223.3\,A}}\dot{C}_{2223.3\,FS}\overline{\varepsilon_{1261.7\,FS}}}{\dot{C}_{2223.3\,A}\overline{\varepsilon_{1261.7\,A}}\dot{C}_{1261.7\,FS}\overline{\varepsilon_{2223.3\,FS}}} v_{E\,FS} v_{E\,A}} \qquad \text{6-21}$$

The limits for the range of possible fiber volumes for FS1-6 can be calculated analytically using a modified version of equation 6-17,

$$v_{F\,FS} = \frac{\dfrac{N_{C\,E}}{N_{C_F}}\left(1 - \dfrac{\dot{C}_{1261.7\,A}\overline{\varepsilon_{2223.3\,A}}\dot{C}_{2223.3\,FS}\overline{\varepsilon_{1261.7\,FS}}}{\dot{C}_{2223.3\,A}\overline{\varepsilon_{1261.7\,A}}\dot{C}_{1261.7\,FS}\overline{\varepsilon_{2223.3\,FS}}}\right) + \dfrac{v_{F\,A}}{v_{E\,A}}}{\dfrac{\dot{C}_{1261.7\,A}\overline{\varepsilon_{2223.3\,A}}\dot{C}_{2223.3\,FS}\overline{\varepsilon_{1261.7\,FS}}}{\dot{C}_{2223.3\,A}\overline{\varepsilon_{1261.7\,A}}\dot{C}_{1261.7\,FS}\overline{\varepsilon_{2223.3\,FS}}} + \dfrac{N_{C\,E}}{N_{C_F}}\left(1 - \dfrac{\dot{C}_{1261.7\,A}\overline{\varepsilon_{2223.3\,A}}\dot{C}_{2223.3\,FS}\overline{\varepsilon_{1261.7\,FS}}}{\dot{C}_{2223.3\,A}\overline{\varepsilon_{1261.7\,A}}\dot{C}_{1261.7\,FS}\overline{\varepsilon_{2223.3\,FS}}}\right) + \dfrac{v_{F\,A}}{v_{E\,A}}} . \qquad \text{6-22}$$

The fiber volume of FS1-6 is in the range of 66.5% ± 0.5% and 64% ± 1% with a best estimate value of 65.2 ± 1.4%. This matches well with the UT-CEM estimate of ~60% - 65%.

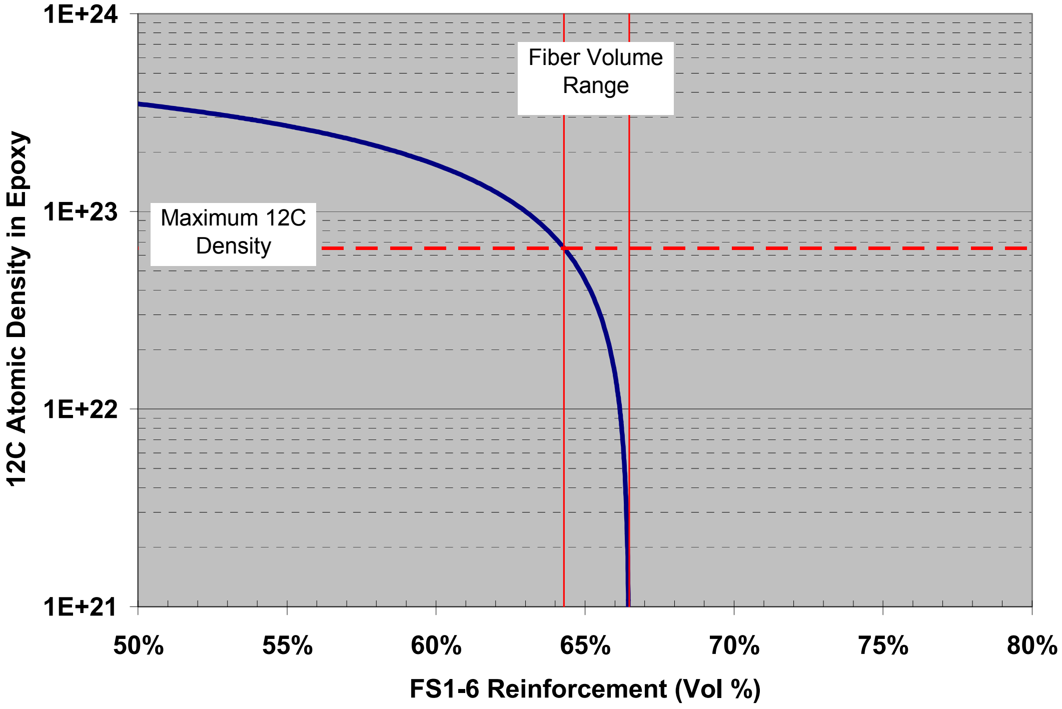

Figure 6.4. Range of fiber volumes for FS1-6.

6.5 Discussion and Conclusions

Although the test coupons were not ideally suited for this fiber volume investigation, prompt gamma measurements were used to estimate the fiber volume of two samples relative to the fiber volume of a third. The fiber volume ranges calculated for B123 and FS1-6 yielded excellent agreement with UT-CEM measurements and estimates. This is the first nondestructive measurement of carbon fiber volume ever performed. The atomic density of the ^{12}C in the epoxy was calculated to be $(3.8 \pm 1.1)\times10^{22}$ atoms/cm^3 after flux and efficiency mapping was used to compare sample A234 and FS1-6. The large error bars are due to the relatively low epoxy content of the samples. By inserting the ^{12}C epoxy content into the appropriate equations, the fiber volumes of sample B123 and FS1-6 are calculated to be 71.3% ± 0.3% and 65.2% ± 1.4%, respectively. Because of the high fiber volume of each sample, the atomic density of ^{12}C in the epoxy could not be distinguished from the ^{12}C atomic density in the fibers with high accuracy. This implies that the ^{12}C content in Cytec 977-2 epoxy is small and could be neglected without significant loses in accuracy for high fiber volume samples.

PGAA measurements of fiber volume do indicate a slight discrepancy in the fiber volume of sample B123, which was initially reported by the UT-CEM to have a slightly greater fiber volume than sample A234. This is likely just due to slightly larger uncertainties in the UT-CEM measurements than was reported. To determine the actual fiber volumes of all samples measured, acid digestion tests were planned. Each individual sample within the clamped samples was cut into thirds. TRI-Austin was contracted to perform acid digestion analysis on a portion of each sample. Current results are shown in Table 6.10.

Technicians at TRI-Austin had difficulty processing the samples according to ASTM standards for acid digestion, and fiber volumes calculated from their data are inconsistent with previous measurements at the UT-CEM using materials from the same fabrication. Given that TRI-Austin values show a significant range in fiber volume for samples from the same hoop, they are considered unreliable. The samples sent to TRI-Austin are also completely lost, since acid digestion is a destructive test. The inability of industry to accurately perform acid digestion for composite sample constituent determination underscores the need for this new non-destructive tool.

Table 6.10. Fiber Volume Data Reported by TRI-Austin

Sample ID	Sample Mass [g]	Sample Density [g/cm^3]	Reinforcement Content [% wt]	Reinforcement Content [% vol]*	Matrix Content [% wt]	Matrix Content [% vol]*
A1.3	1.4230	1.629	93.6	84.7	6.4	7.96
A2.2	1.5434	1.657	79.8	73.5	20.2	25.55
A3.3	1.4525	1.614	91.8	82.3	8.2	10.10
B1.3	1.4575	1.695	78.4	73.8	21.6	27.95
B2.3	1.5870	1.647	89.6	82.0	10.4	13.08
B3.2	1.3776	1.650	91.8	84.2	8.2	10.33
FS1.1	1.4750	1.656	83.0	76.4	17.0	21.49
FS2.2	1.5775	1.614	80.0	71.7	19.9	24.52
FS3.1	1.6612	1.664	90.8	83.9	9.2	11.69
FS4.3	1.5750	1.657	80.0	73.6	20.2	25.55
FS5.1	1.5977	1.610	87.1	77.9	12.8	15.73
FS6.3	1.5907	1.631	83.9	76.0	16.1	20.05

*TRI-Austin reported weight percents only. Volume percents were calculated using TRI-Austin weight percents and UT-CEM densities for fibers and epoxy.

Counting statistics of better than 1% error for fiber volume measurements on clamped samples can be obtained in approximately 24 hours of integrated irradiation at a reactor power of 950 kW. For single samples approximately 2 mm thick, counting time is increased to approximately 40 hours to achieve counting statistics better than 1% for all relevant peaks. Counting times are dictated by the low radiative capture cross section for ^{12}C (1.24 mb at 2200 m/s) and the amount of sample in the beam. The UT-CEM requires approximately 24 hours to process a sample, and has the facilities to test 2 samples simultaneously. Typically, 4 samples from a single ring are acid digested and the average fiber volume measurement is applied to the entire batch. PGAA can compare the bulk fiber volume of a similar amount of material in a comparable amount of irradiation time. Prompt gamma fiber volume measurements at the UT-NETL have the potential to be performed on time scales competitive with UT-CEM measurements.

CHAPTER 7. Conclusions and Future Work

Prompt gamma activation analysis is a powerful nuclear analytical technique and several dedicated facilities have been installed in the past decade as new research reactors and spallation neutron sources are constructed. PGAA has also been applied outside of laboratory settings with isotopic neutron sources for environmental, geological, medical, and industrial uses. The use of cold neutrons for PGAA allows the neutron beam to be guided to low gamma background locations, and focused to increase the maximum neutron flux. The radiative capture cross section for all isotopes also increases as neutron energy decreases.

The acquisition of prompt gamma spectra is straightforward, given a sufficient neutron source. Prompt gamma peaks can be readily attributed to the target isotope and used to identify the isotopic constituents of the sample material. Quantitative analysis of a single prompt gamma spectrum was shown to be complicated. The measurement of efficiencies at high energy, as well as spatial and temporal variations in the detection efficiency and neutron flux is not straightforward. For the case of cold neutrons, changing neutron energy spectra due to scattering within a sample can have significant effects.

This dissertation has described the development of prompt gamma activation analysis techniques for measurements on carbon fiber reinforced, polymer matrix composites. Neutron and gamma shielding for the HPGe detector was redesigned to minimize interference gamma rays and their associated prompt gamma continuum, particular for lead. Sample holders were designed to allow reproducible sample placement within the neutron beam. Different sample holders were designed to hold different sized samples in several orientations to the beam. A neutron fluence monitor was installed to aid in the comparison of spectra acquired from irradiation to irradiation.

A new technique was developed to perform neutron flux measurements concurrent with high energy efficiency calibrations. Experimenters at facilities world-wide have relied on the combination of decay sources and on-line prompt gamma measurements to generate and combine absolute and relative efficiency curves energy ranges above a few MeV. By using a sample with a short activation half-life, a simple low energy calibration can be extended to high energies based on the measured reaction rate and prompt gamma yields. Since a single measurement can be used, the potential introduction of human error due to sample handling is minimized. The use of vanadium for this technique is not exclusive. It may also be useful to use a molecular compound such as vanadium nitride to take advantage of the short vanadium activation half-life and the extensive prompt gamma spectrum of nitrogen.

The new PGAA characterization techniques were used to develop the first non-destructive tool to analyze the fiber volume of carbon fiber composite coupons of several geometries. The ultimate strength of fibrous composite materials is primarily dependent on the fiber volume, and knowledge of this property is required to perform failure calculations. Current ASTM standards for the determination of composite fiber volume require destructive acid digestion. The procedures for acid digestion of composite samples are also vague, and given the inability of contracted laboratories to obtain consistent results, the process could be described as more art than science. PGAA measurements made as part of the investigation described in this dissertation were able to identify differences in fiber volume for three samples. Using a reference sample, fiber volumes were calculated to within approximately 1%. Measurements matched well with expected values. Prior to this investigation, a non-destructive tool for composite fiber volume measurement did not exist. The development of PGAA as a new tool for fiber volume determination is expected to enhance the performance and analysis of destructive tests, and ultimately, allow more accurate prediction of composite failure stress.

Prompt gamma measurements were also applied to detect water absorption and desorption by a composite coupon sample. The presence of water within composite sample matrices can alter hydrogen bonding and potentially weaken the material. Current ASTM methods to monitor water content are gravimetric and rely on an indirect measurement to infer bulk water content. It may also be impractical to weigh some samples, such as helicopter rotors. PGAA can be used to detect the ^{1}H content in the sample volume exposed to the beam. By measuring changes in the ^{1}H concentration within a sample volume, changes in the water content can be directly determined. A composite coupon was tested during absorption and desorption phases to determine the sensitivity for water detection at the UT-NETL PGAA facility. Tests were successful, but of limited sensitivity due to the low flux available at the UT-NETL. The application of this technique was extrapolated to higher flux facilities, and it was shown that this could prove a powerful technique at a facility like NIST.

During the course of this study, several areas of interest have been identified for future work. These break down into general ideas for improvements to the UT-NETL PGAA facility, steps that can be taken to extend the experiments performed during this study, and additional investigations to answer questions generated as part of this study.

Additional experiments are suggested to determine the cold neutron beam energy spectrum. The spectrum could be unfolded using foil irradiations, or measured directly using time of flight and a chopper. Increased knowledge of the beam will improve MCNP models for the facility. An accurate MCNP model for the HPGe detector should also be developed so Monte Carlo Library Least Squares techniques can be investigated for complex samples. Flux monitoring investigations showed that the neutron flux delivered by the TCNS decreased steadily during the course of a day, but the cause of this phenomenon has not been identified. The cause of this transient, possibly changing neutron energy spectrum, or buildup of fission products, should be determined to identify the effects on PGAA reproducibility.

Several additions to the existing PGAA facility at the UT-NETL would significantly enhance the facility's capabilities. These include:

- The addition of a capillary focusing lens could significantly increase the neutron flux delivered to a sample.
- The addition of Compton suppression equipment to the PGAA spectrometer will further improve the signal-to-noise ratio. The use of Compton suppression is nearly universal for cold neutron PGAA facilities world-wide.
- The elimination of hydrogenous materials from neutron shielding will minimize ^{1}H interference.

The PGAA facility at the UT-NETL is a unique facility, both within the United States and worldwide. The TCNS is the only university cold neutron source in the United States, and given the reactor size, delivers a very intense and well-collimated beam to the PGAA sample area. The PGAA facility at the UT-NETL has been shown to be a powerful tool for the non-destructive analysis of composite material properties.

Appendix A. Detector Quality Assurance Data from Manufacturer

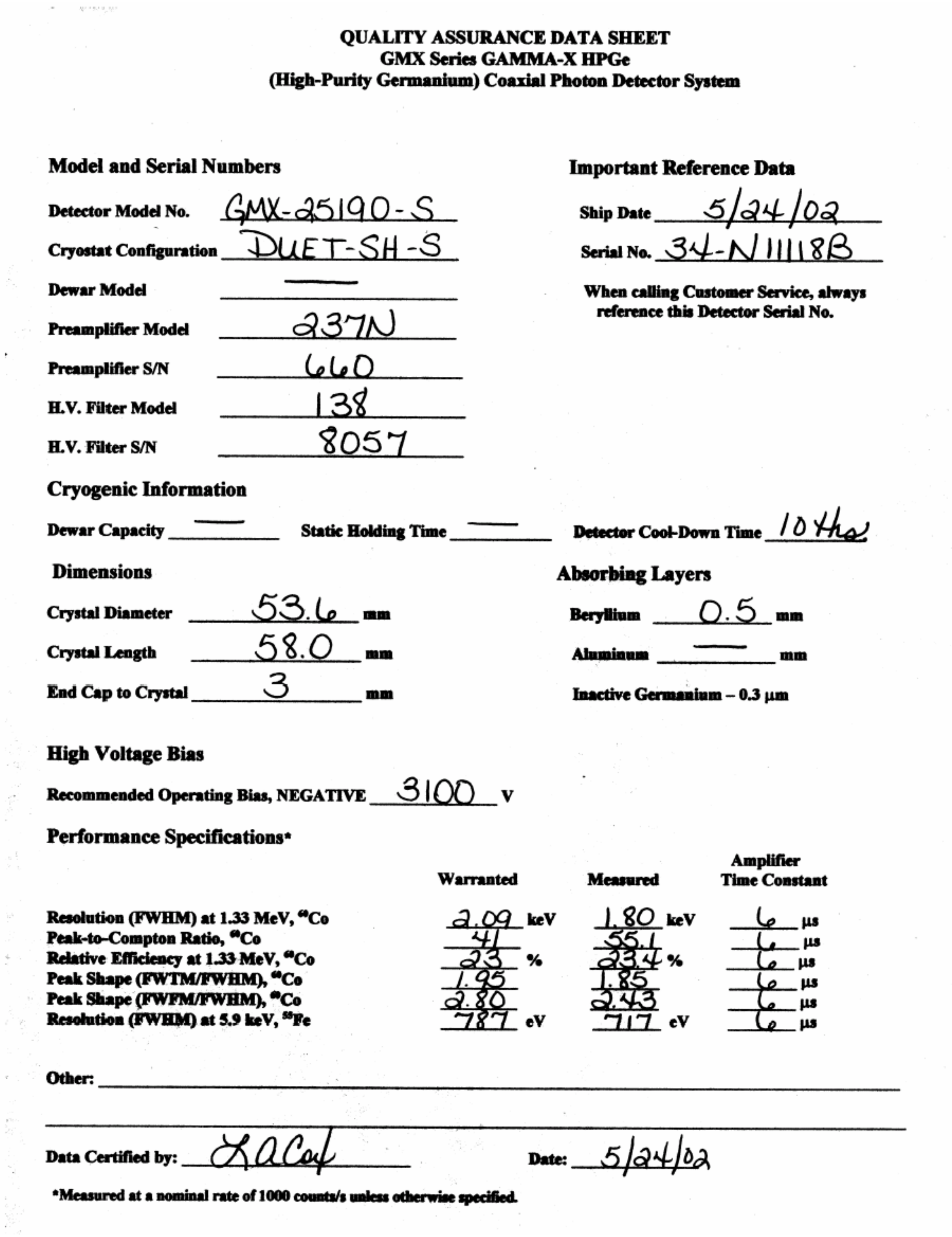

QUALITY ASSURANCE DATA SHEET
GMX Series GAMMA-X HPGe
(High-Purity Germanium) Coaxial Photon Detector System

Model and Serial Numbers

Detector Model No. GMX-25190-S

Cryostat Configuration DUET-SH-S

Dewar Model —

Preamplifier Model 237N

Preamplifier S/N 660

H.V. Filter Model 138

H.V. Filter S/N 8057

Important Reference Data

Ship Date 5/24/02

Serial No. 34-N11118B

When calling Customer Service, always reference this Detector Serial No.

Cryogenic Information

Dewar Capacity — **Static Holding Time** — **Detector Cool-Down Time** 10 hrs

Dimensions

Crystal Diameter 53.6 **mm**

Crystal Length 58.0 **mm**

End Cap to Crystal 3 **mm**

Absorbing Layers

Beryllium 0.5 **mm**

Aluminum — **mm**

Inactive Germanium – 0.3 µm

High Voltage Bias

Recommended Operating Bias, NEGATIVE 3100 **V**

Performance Specifications*

	Warranted	Measured	Amplifier Time Constant
Resolution (FWHM) at 1.33 MeV, ^{60}Co	2.09 keV	1.80 keV	6 µs
Peak-to-Compton Ratio, ^{60}Co	41	55.1	6 µs
Relative Efficiency at 1.33 MeV, ^{60}Co	23 %	23.4 %	6 µs
Peak Shape (FWTM/FWHM), ^{60}Co	1.95	1.85	6 µs
Peak Shape (FWFM/FWHM), ^{60}Co	2.80	2.43	6 µs
Resolution (FWHM) at 5.9 keV, ^{55}Fe	787 eV	717 eV	6 µs

Other:

Data Certified by: **Date:** 5/24/02

*Measured at a nominal rate of 1000 counts/s unless otherwise specified.

Appendix B. Core Configurations

Number	Title	Rev. 0
FUEL-1	Movement of Fuel	Date 6/90

Core Arrangement

Reference RELOAD AFTER FLOOD REFLECTOR
Date 4/27/2000

Configuration Number:
Control-~~Fuel~~-~~Space~~-~~Other~~
89F-17G-12W-00

Ⓖ26 Ⓖ27 Ⓖ28 Ⓖ29 Ⓖ30
2668E 1918E 2686 2622E 2639E

G-24 F-21 F-22 F-23 F-24 F-25 F-26 G-32
W 2974 2975 2976 2977 2979 2983 W

Ⓖ23 F-20 E-17 E-18 E-19 E-20 E-21 F-27 Ⓖ33
2644E 2971 2929 2930 2932 2935 2938 2984 2711E

G-22 F-19 E-16 D-13 D-14 D-15 D-16 E-22 F-28 G-34
W 2970 2928 5919 SHM2 5920 6142 2939 2985 W/PNT

Ⓖ21 F-18 E-15 D-12 C-09 C-10 C-11 D-17 E-23 F-29 Ⓖ35
2634E 2969 2927 5918 6929 6930 6889 6923 2940 5198 2712E

G-20 F-17 E-14 D-11 C-08 B-05 B-06 C-12 D-18 E-24 F-30 G-36
W 2968 2925 5915 6928 6886 10708 6932 6925 2941 3513 S

F-16 E-13 D-10 C-07 B-04 B-01 C-01 D-01 E-01 F-01
2965 2918 5914 REG 6143 5921 TRNS 5844 2899 2944

Ⓖ18 F-15 E-12 D-09 C-06 B-03 B-02 C-02 D-02 E-02 F-02 Ⓖ02
2667E 2964 2915 5913 6927 5982 5922 5916 5845 2902 2946 2635E

Ⓖ17 F-14 E-11 D-08 C-05 C-04 C-03 D-03 E-03 F-03 Ⓖ03
2673E 2962 2913 5912 6926 6924 5917 5846 2903 2947 2700E

G-16 F-13 E-10 D-07 D-06 D-05 D-04 E-04 F-04 G-04
W 2960 2912 5904 SHM1 5903 5902 2904 2948 W

Ⓖ15 F-12 E-09 E-08 E-07 E-06 E-05 F-05 Ⓖ05
1946E 2959 2911 2910 2908 2906 2905 2950 2652E

Ⓖ14 F-11 F-10 F-09 F-08 F-07 F-06 Ⓖ06
2671E 2958 2957 2955 2954 2952 2951 2648E

G-12 G-11 G-10 G-09 G-08
W W W W W

1/29/01 REMOVE 5982 FROM B3, INSTALL 10878 TC

COPY

Page 1 of 3

Number	Title	Rev. 0
FUEL-1	Movement of Fuel	Date 6/90

Core Arrangement

Reference 3L configuration
Date 7/30/01

Configuration Number:
~~Control-Fuel-Space-Other~~
95F - 13G - 7W - 00

G-26	G-27	G-28	G-29	G-30							
2668E	2931	2686	2943	2639E							
G-24	F-21	F-22	F-23	F-24	F-25	F-26	G-32				
2939	2974	2975	2976	2977	2979	2983	S				
G-23	F-20	E-17	E-18	E-19	E-20	E-21	F-27	G-33			
2644E	2971	2929	2930	2932	2935	2935	2984	2711E			
G-22	F-19	E-16	D-13	D-14	D-15	D-16	E-22	F-28	G-34		
W	2970	2928	5919	SHM2	5920	6142	W/3L	2955	W/PNT		
G-21	F-18	E-15	D-12	C-09	C-10	C-11	D-17	E-23	F-29	G-35	
2634E	2969	2927	5918	6929	6930	6889	W/3L	W/3L	5198	2712E	
G-20	F-12	E-14	D-11	C-08	B-05	B-06	C-02	D-18	E-24	F-30	G-36
6923	2968	2925	5915	6928	6886	10708	6932	6925	2941	3513	5911
F-16	E-13	D-10	C-07	B-04		B-01	C-01	D-01	E-01	F-01	
2965	2918	5914	REG	6143		5921	TRNS	5844	2899	2944	
G-18	F-15	E-12	D-09	C-06	B-03	B-02	C-02	D-02	E-02	F-02	G-02
3013	2964	2915	5913	6927	10378	5922	5916	5845	2902	2946	2940
G-17	F-14	E-11	D-08	C-05	C-04	C-03	D-03	E-03	F-03	G-03	
2073E	2962	2913	5912	6926	6924	5917	5846	2903	2947	2700E	
G-16	F-13	E-10	D-07	D-06	D-05	D-04	E-04	F-04	G-04		
W	2960	2912	5904	SHM1	5903	5902	2904	2945	W		
G-15	F-12	E-09	E-08	E-07	E-06	E-05	F-05	G-05			
1946E	2959	2911	2910	2908	2906	2905	2950	2652E			
G-14	F-11	F-10	F-09	F-08	F-07	F-06	G-06				
2071E	2958	2957	2955	2954	2952	2951	2648E				
G-12	G-11	G-10	G-09	G-08							
2997	W	W	W	2980							

COPY

Page 1 of 3

Core Arrangement

Reference 3L Configuration
Date 7 / 22 / 02

Configuration Number:
Fuel - Graphite - Water - Other
95F - 13 - 10 - 02 (REV #)

G-26 G-27 G-28 G-29 G-30
2668E 2668 2686E 2943 2936E

G-24 F-21 F-22 F-23 F-24 F-25 F-26 G-32
2939 2974 2975 2941 2977 2979 2983 **S**

G-23 F-20 E-17 E-18 E-19 E-20 E-21 F-27 G-33
2644E 2971 2929 2930 2932 2935 6932 2968 2711E

G-22 F-19 E-16 D-13 D-14 D-15 D-16 E-22 F-28 G-34
W 6925 2928 5919 **SHM2** 5920 2951 **W/3L** 2957 **W/PNT**

G-21 F-18 E-15 D-12 C-09 C-10 C-11 D-17 E-23 F-29 G-35
2634E 2969 6932 5918 6929 6930 2954 **W/3L** **W/3L** 2913 2712E

G-20 F-17 E-14 D-11 C-08 B-05 B-06 C-12 D-18 E-24 F-30 G-36
6923 2984 2925 5915 6928 6886 10708 2927 2970 2941 3513 5911

F-16 E-13 D-10 C-07 B-04 B-01 C-01 D-01 E-01 F-01
2965 2918 5914 **REG** 6143 2952 **TRNS** 2948 2899 2944

G-18 F-15 E-12 D-09 C-06 B-03 B-02 C-02 D-02 E-02 F-02 G-02
3013 2964 2915 5913 6927 10878 5922 2938 2904 2902 2946 2940

G-17 F-14 E-11 D-08 C-05 C-04 C-03 D-03 E-03 F-03 G-03
2073E 2962 5198 5912 6926 6924 5917 5846 2903 2947 2700E

G-16 F-13 E-10 D-07 D-06 D-05 D-04 E-04 F-04 G-04
W 2960 2912 5904 **SHM1** 5903 5902 5845 5844 **W**

G-15 F-12 E-09 E-08 E-07 E-06 E-05 F-05 G-05
1946E 2959 2911 2958 2908 2906 2905 2950 2652E

G-14 F-11 F-10 F-09 F-08 F-07 F-06 G-06
2071E 2910 2985 2955 6889 5921 6142 2648E

G-12 G-11 G-10 G-09 G-08
2992 **W** **W** **W** 2980

L. Welch

Core Arrangement

Reference 3L Configuration
Date 11 / ~~22~~ 13 / 02

Configuration Number:
Fuel - Graphite - Water - Other
103 - 5 - 10 - Rev01

G-26	G-27	G-28	G-29	G-30
10816	2668	2686E	2943	10817

G-24	F-21	F-22	F-23	F-24	F-25	F-26	G-32
2939	2974	2975	2941	2977	2979	2983	S

G-23	F-20	E-17	E-18	E-19	E-20	E-21	F-27	G-33
2644E	2971	2929	2930	2932	2935	6932	2968	2711E

G-22	F-19	E-16	D-13	D-14	D-15	D-16	E-22	F-28	G-34
W	6925	2928	5919	**SHM2**	5920	2951	W/3L	2957	W/PNT

G-21	F-18	E-15	D-12	C-09	C-10	C-11	D-17	E-23	F-29	G-35
2634E	2969	6932	5918	6929	6930	2954	W/3L	W/3L	2913	2712E

G-20	F-17	E-14	D-11	C-08	B-05	B-06	C-12	D-18	E-24	F-30	G-36
6923	2984	2925	5915	6928	6886	10708	2927	2970	2941	3513	5911

F-16	E-13	D-10	C-07	B-04	B-01	C-01	D-01	E-01	F-01
2965	2918	5914	**REG**	6143	2952	**TRNS**	2948	2899	2944

G-18	F-15	E-12	D-09	C-06	B-03	B-02	C-02	D-02	E-02	F-02	G-02
3013	2964	2915	5913	6927	10878	5922	2938	2904	2902	2946	2940

G-17	F-14	E-11	D-08	C-05	C-04	C-03	D-03	E-03	F-03	G-03
10815	2962	5198	5912	6926	6924	5917	5846	2903	2947	10810

G-16	F-13	E-10	D-07	D-06	D-05	D-04	E-04	F-04	G-04
W	2960	2912	5904	**SHM1**	5903	5902	5845	5844	W

G-15	F-12	E-09	E-08	E-07	E-06	E-05	F-05	G-05
10814	2959	2911	2958	2908	2906	2905	2950	10811

G-14	F-11	F-10	F-09	F-08	F-07	F-06	G-06
10813	2910	2985	2955	6889	5921	6142	10812

G-12	G-11	G-10	G-09	G-08
2992	W	W	W	2980

Appendix C. SRM 4218F Certificate

National Institute of Standards & Technology

Certificate

Standard Reference Material 4218F
Europium-152 Radioactivity Standard

This Standard Reference Material (SRM) consists of a dried deposit of radioactive europium-152 chloride and non-radioactive europium chloride on a filter-paper disk sealed between two layers of polyester tape that are supported on an aluminum annulus. The SRM is intended for the calibration of gamma-ray spectrometry systems.

Radiological Hazard

The SRM contains europium-152 with a total activity of less than 150 kBq. Europium-152 decays by beta-particle emission and by electron capture. Some of the beta particles escape from the SRM. During the decay process X-rays and gamma rays with energies from 6 keV to 1600 keV are emitted. Most of these photons escape from the SRM and can represent a radiation hazard. Approximate unshielded dose rates at several distances (as of the reference time) are given in note [a]*. Appropriate shielding and/or distance should be used to minimize personnel exposure. The SRM should be used only by persons qualified to handle radioactive material.

Chemical Hazard

The SRM contains less than 10 μg of europium chloride. The material does not represent a significant chemical hazard.

Storage and Handling

The SRM should be stored and used at a temperature between 5 and 40 °C. If the point source is properly handled and stored, it should remain stable until at least January 2009.

The SRM should always be clearly marked as containing radioactive material. If the SRM is transported it should be packed, marked, labeled, and shipped in accordance with the applicable national, international, and carrier regulations. The SRM is a dangerous good (hazardous material) because of the radioactivity.

Preparation

This Standard Reference Material was prepared in the Physics Laboratory, Ionizing Radiation Division, Radioactivity Group, L.R. Karam, Group Leader. The overall technical direction and physical measurements leading to certification were provided by L.L. Lucas of the Radioactivity Group and D.B. Golas, Nuclear Energy Institute Research Associate.

The support aspects involved in the preparation, certification, and issuance of this SRM were coordinated through the Standard Reference Materials Program by N.M. Trahey.

Gaithersburg, Maryland 20899
January 1999

Thomas E. Gills, Chief
Standard Reference Materials Program

*Notes and references are on pages 5 and 6.

BLANK PAGE

*Notes and references are on pages 5 and 6.

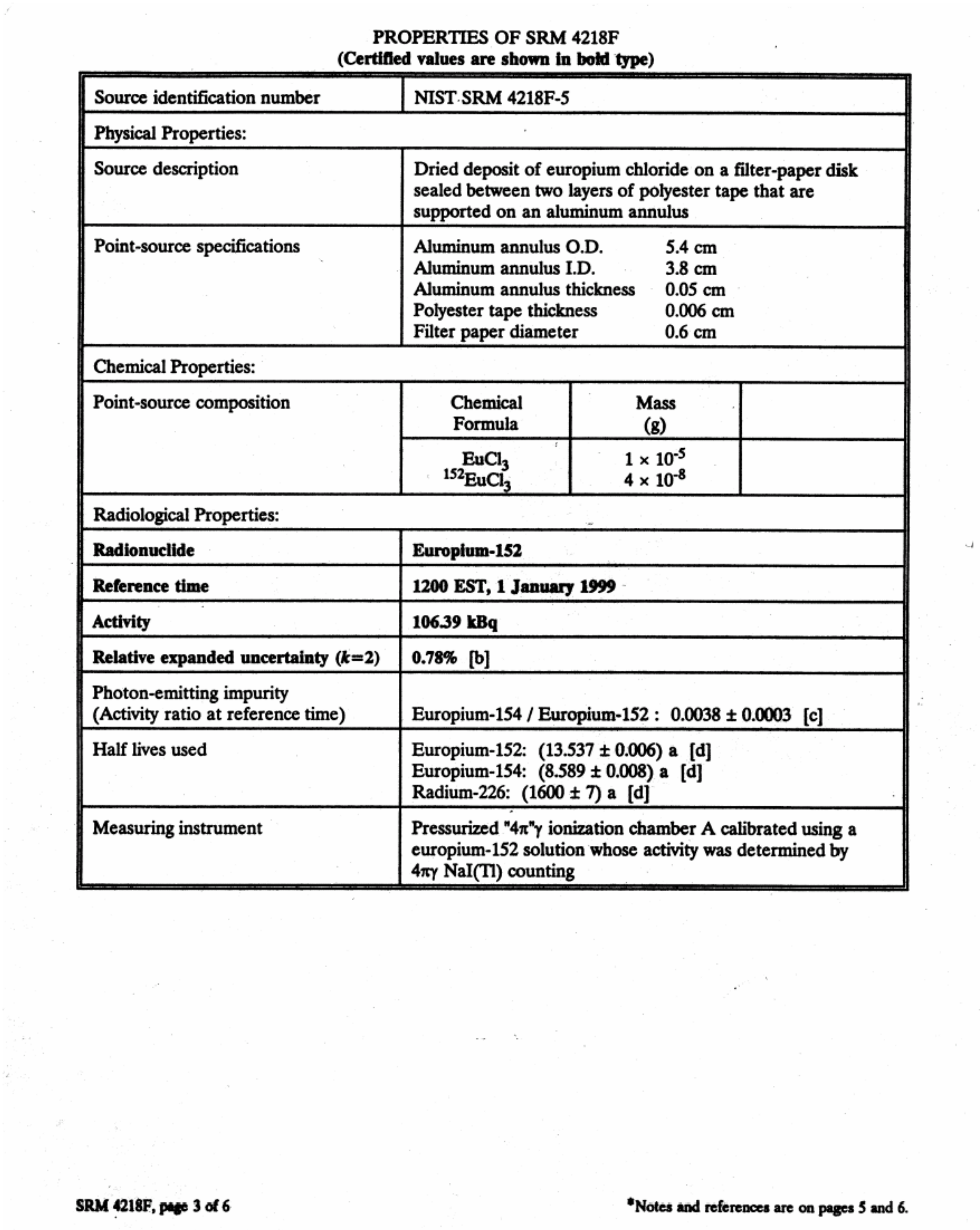

PROPERTIES OF SRM 4218F
(Certified values are shown in bold type)

Source identification number	NIST SRM 4218F-5		
Physical Properties:			
Source description	Dried deposit of europium chloride on a filter-paper disk sealed between two layers of polyester tape that are supported on an aluminum annulus		
Point-source specifications	Aluminum annulus O.D. 5.4 cm Aluminum annulus I.D. 3.8 cm Aluminum annulus thickness 0.05 cm Polyester tape thickness 0.006 cm Filter paper diameter 0.6 cm		
Chemical Properties:			
Point-source composition	Chemical Formula	Mass (g)	
	$EuCl_3$ $^{152}EuCl_3$	1×10^{-5} 4×10^{-8}	
Radiological Properties:			
Radionuclide	**Europium-152**		
Reference time	**1200 EST, 1 January 1999**		
Activity	**106.39 kBq**		
Relative expanded uncertainty (*k*=2)	**0.78%** [b]		
Photon-emitting impurity (Activity ratio at reference time)	Europium-154 / Europium-152 : 0.0038 ± 0.0003 [c]		
Half lives used	Europium-152: (13.537 ± 0.006) a [d] Europium-154: (8.589 ± 0.008) a [d] Radium-226: (1600 ± 7) a [d]		
Measuring instrument	Pressurized "4π"γ ionization chamber A calibrated using a europium-152 solution whose activity was determined by 4πγ NaI(Tl) counting		

[*]Notes and references are on pages 5 and 6.

EVALUATION OF THE UNCERTAINTY OF THE ACTIVITY [b]*

Input Quantity x_i, the source of uncertainty (and individual uncertainty components where appropriate)	Method Used To Evaluate $u(x_i)$, the standard uncertainty of x_i (A) denotes evaluation by statistical methods (B) denotes evaluation by other methods	Relative Uncertainty Of Input Quantity, $u(x_i)/x_i$, (%) [e]	Relative Sensitivity Factor, $\lvert \partial y/\partial x_i \rvert \cdot (x_i/y)$ [f]	Relative Uncertainty Of Output Quantity, $u_i(y)/y$, (%) [g]
PIC A net response per gram of master solution, measured relative to RRS500 [h]	Standard deviation of the mean for 300 repeated measurements (A)	0.005	1.0	0.005
PIC A background response, measured relative to RRS500	Standard deviation of the mean for >250 repeated measurements (A)	0.25	0.00004 [i]	0.00001
PIC A net response for RRS200, measured relative to RRS500	Standard deviation of the mean for >100 repeated measurements (A)	0.07	1.0	0.07
PIC A net response per Bq of europium-152 in solution, measured relative to RRS200.	Standard deviation of the mean for >100 repeated measurements (A)	0.02	1.0	0.02
Gravimetric measurements	Estimated (B)	0.10	1.0	0.10
Half life of europium-152 Half life of radium-226	Standard uncertainty of the half life (A)	0.04 [j] 0.44 [j]	0.006 [k] 0.009 [k]	0.0003 0.004
Activity used to calibrate PIC A net response per Bq of europium-152 in solution	Standard uncertainty of the activity determined by $4\pi\gamma$ NaI(Tl) counting (B)	0.33	1.0	0.33
Live-time [m]	Estimated (B)	0.10	1.0	0.10
PIC A charge collection	Estimated (B)	0.05	1.0	0.05
Source Positioning	Estimated (B)	0.05	1.0	0.05
Photon-emitting impurities	Estimated (B) [n] Limit of detection (B) [p]	4. 100.	0.001 0.001	0.004 0.10
Relative Combined Standard Uncertainty of the Output Quantity, $u_c(y)/y$, (%)				0.39
Coverage Factor, k				x 2
Relative Expanded Uncertainty of the Output Quantity, U/y, (%)				0.78

*Notes and references are on pages 5 and 6.

NOTES

[a] The Sievert is the SI unit for dose equivalent. See reference [1]. One μSv is equal to 0.1 mrem.

Distance from Source (cm):	1	30	100
Approximate Dose Rate (μSv/h):	50	0.5	<0.1

[b] The reported value, y, of activity at the reference time was not measured directly but was derived from measurements and calculations of other quantities. This can be expressed as $y = f(x_1, x_2, x_3, \ldots x_n)$, where f is a mathematical function derived from the assumed model of the measurement process.

The value, x_i, used for each input quantity i has a **standard uncertainty**, $u(x_i)$, that generates a corresponding uncertainty in y, $u_i(y) \equiv |\partial y/\partial x_i| \cdot u(x_i)$, called a **component of combined standard uncertainty** of y.

The **combined standard uncertainty** of y, $u_c(y)$, is the positive square root of the sum of the squares of the components of combined standard uncertainty.

The combined standard uncertainty is multiplied by a **coverage factor** of $k = 2$ to obtain U, the **expanded uncertainty** of y.

Since it can be assumed that the possible estimated values of the massic activity are approximately normally distributed with approximate standard deviation $u_c(y)$, the unknown value of the massic activity is believed to lie in the interval $y \pm U$ with a level of confidence of approximately 95 percent.

For further information on the expression of uncertainties, see references [2] and [3].

[c] The stated uncertainty is two times the standard uncertainty.

Estimated limits of detection for photon-emitting impurities are:
0.0003 $\gamma \cdot s^{-1} \cdot Bq^{-1}$ for energies between 90 and 118 keV,
0.00009 $\gamma \cdot s^{-1} \cdot Bq^{-1}$ for energies between 125 and 440 keV,
0.00003 $\gamma \cdot s^{-1} \cdot Bq^{-1}$ for energies between 448 and 1408 keV,
0.00002 $\gamma \cdot s^{-1} \cdot Bq^{-1}$ for energies between 1412 and 3200 keV, provided that the photons are separated in energy by 4 keV or more from photons emitted in the decay of europium-152.

[d] The stated uncertainty is the standard uncertainty. See reference [5].

[e] Relative standard uncertainty of the input quantity x_i.

[f] The relative change in the output quantity y divided by the relative change in the input quantity x_i. If $|\partial y/\partial x_i| \cdot (x_i/y) = 1.0$, then a 1% change in x_i results in a 1% change in y. If $|\partial y/\partial x_i| \cdot (x_i/y) = 0.05$, then a 1% change in x_i results in a 0.05% change in y.

[g] Relative component of combined standard uncertainty of output quantity y, rounded to two significant figures or less. The relative component of combined standard uncertainty of y is given by $u_i(y)/y \equiv |\partial y/\partial x_i| \cdot u(x_i)/y = |\partial y/\partial x_i| \cdot (x_i/y) \cdot u(x_i)/x_i$. The numerical values of $u(x_i)/x_i$, $|\partial y/\partial x_i| \cdot (x_i/y)$, and $u_i(y)/y$, all dimensionless quantities, are listed in columns 3, 4, and 5, respectively. Thus, the value in column 5 is equal to the value in column 4 multiplied by the value in column 3. The input quantities are independent, or very nearly so. Hence the covariances are zero or negligible.

[h] The response of pressurized ionization chamber A (PIC A) is determined from measurement of the time required to collect a given amount of charge on a stable fixed capacitor. All of the response measurements in the NIST pressurized ionization chambers are made relative to the response of one or more artifact standards. These artifact standards consist of microgram quantities of aged radium-226 in small welded stainless-steel capsules. These capsules are encapsulated in plastic rods whose dimensions are similar to those of the standard NIST ampoule. The artifact standards are called **Radium Reference Sources** and are designated as RRSx, where x is the nominal mass (in micrograms) of radium-226 in the capsule.

[i] $|\partial y/\partial x_i| \cdot (x_i/y)$ = (average background response)/(average net sample response)

[j] The relative standard uncertainty of $\lambda \cdot t$ is determined by the relative standard uncertainty of λ (i.e., of the half life). The relative standard uncertainty of t is negligible.

[k] $|\partial y/\partial x_i| \cdot (x_i/y) = |\lambda \cdot t|$

[m] The live time is determined by counting the pulses from a gated oscillator.

[n] The standard uncertainty given is for the detected impurity. $|\partial y/\partial x_i| \cdot (x_i/y)$ = {(response per Bq of impurity)/(response per Bq of Eu-152)}$\cdot${(Bq of impurity)/(Bq of Eu-152)}.

[p] The standard uncertainty for each undetected impurity that might reasonably be expected to be present is estimated to be equal to the estimated limit of detection for that impurity, i.e. $u(x_i)/x_i$ = 100%. $|\partial y/\partial x_i| \cdot (x_i/y)$ = {(response per Bq of impurity)/(response per Bq of Eu-152)}$\cdot${(Bq of impurity)/(Bq of Eu-152)}. Thus $u_i(y)/y$ is the relative change in y if the impurity were present with a massic activity equal to the estimated limit of detection.

REFERENCES

[1] International Organization for Standardization (ISO), *ISO Standards Handbook - Quantities and Units*, 1993. Available from the American National Standards Institute, 11 West 42nd Street, New York, NY 10036, U.S.A. 1-212-642-4900.

[2] International Organization for Standardization (ISO), *Guide to the Expression of Uncertainty in Measurement*, 1993. Available from the American National Standards Institute, 11 West 42nd Street, New York, NY 10036, U.S.A. 1-212-642-4900. (Listed under ISO miscellaneous publications as "ISO Guide to the Expression 1993".)

[3] B. N. Taylor and C. E. Kuyatt, *Guidelines for Evaluating and Expressing the Uncertainty of NIST Measurement Results*, NIST Technical Note 1297, 1994. Available from the Superintendent of Documents, U.S. Government Printing Office, Washington, DC 20407, U.S.A.

[4] National Council on Radiation Protection and Measurements Report No. 58, *A Handbook of Radioactivity Measurements Procedures*, Second Edition, 1985. Available from the National Council on Radiation Protection and Measurements, 7910 Woodmont Avenue, Bethesda, MD 20814 U.S.A.

[5] Evaluated Nuclear Structure Data File (ENSDF), January 1999.

Appendix D. Sample Holder Schematics

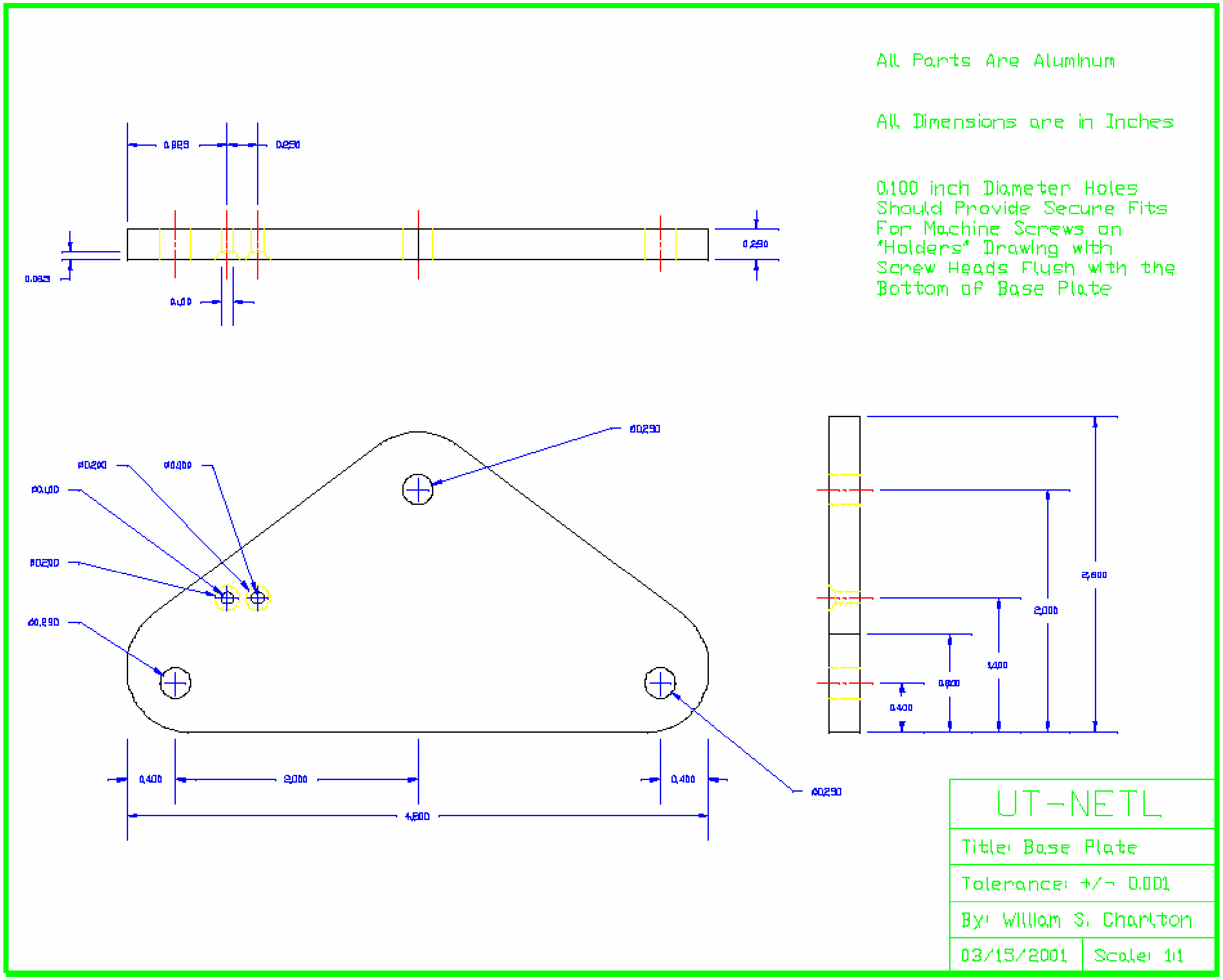
All Parts Are Aluminum
All Dimensions are in Inches
0.100 inch Diameter Holes Should Provide Secure Fits For Machine Screws on "Holders" Drawing with Screw Heads Flush with the Bottom of Base Plate
0.825
0.250
0.085
0.100
0.250
ø0.200
ø0.400
ø0.100
ø0.200
ø0.250
ø0.250
ø0.250
0.400
2.000
0.400
4.800
2.800
2.000
1.400
0.800
0.400
UT-NETL
Title: Base Plate
Tolerance: +/- 0.001
By: William S. Charlton
03/15/2001
Scale: 1:1

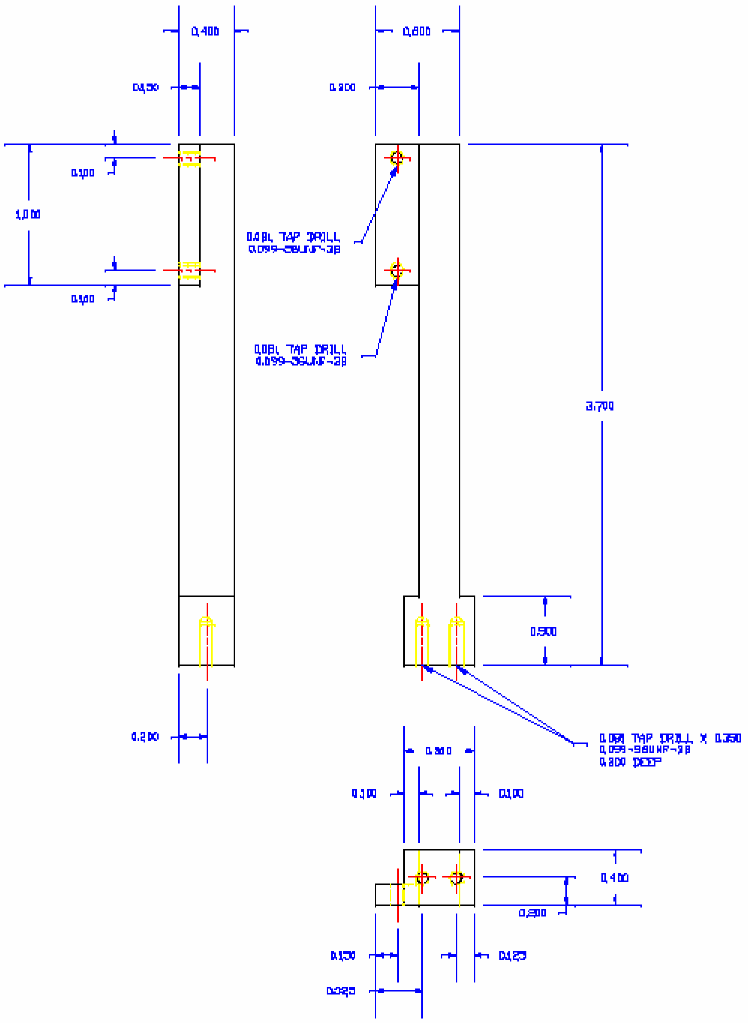

All Parts are Aluminum

All Dimensions are in Inches

Threaded Holes Are
For Machine Screws on
on "Holders" Drawing

Base Plate Connects to
Sample Flag at Bottom of
Sample Flag with Two (2)
Machine Screws

Holders Connect to Flag of
Sample Flag Each Using One (1)
Machine Screw in Thru Hole

UT-NETL

Title: Sample Flag

Tolerance: +/- 0.001

By: William S. Charlton

03/15/2001 | Scale: 1:1

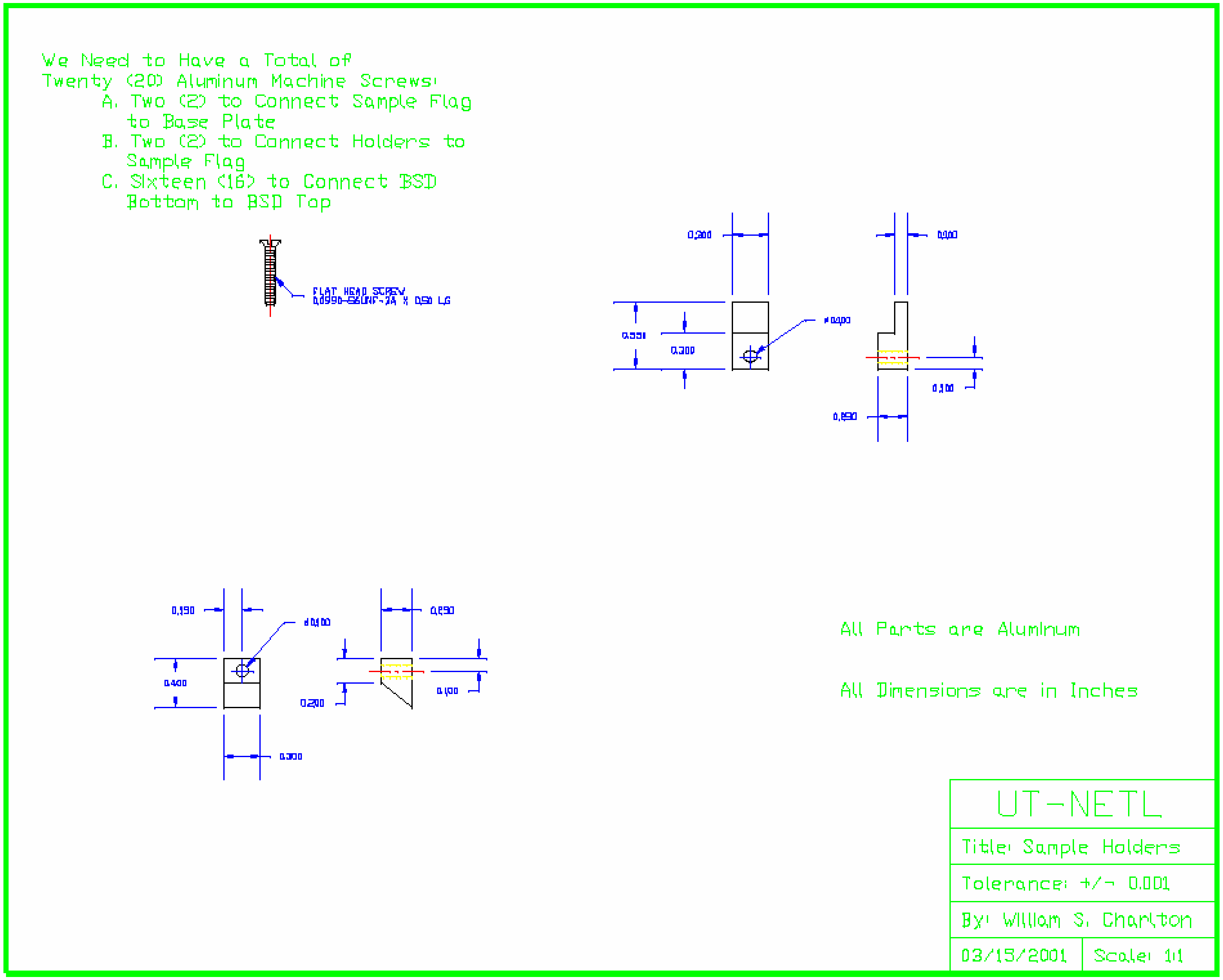

We Need to Have a Total of
Twenty (20) Aluminum Machine Screws:
A. Two (2) to Connect Sample Flag to Base Plate
B. Two (2) to Connect Holders to Sample Flag
C. Sixteen (16) to Connect BSD Bottom to BSD Top

All Parts are Aluminum

All Dimensions are in Inches

UT-NETL
Title: Sample Holders
Tolerance: +/- 0.001
By: William S. Charlton
03/15/2001
Scale: 1:1

Appendix E. Library Data

Table E.1. Cross sections and yields from Molnar Library

Source	Energy [keV]	Cross Section [b]	Yield
^{12}C (n,γ)	1261.765(9)	0.00124	35.33%
^{12}C (n,γ)	3683.920(9)	0.00122	34.76%
^{12}C (n,γ)	4945.301(3)	0.00261	74.36%
^{1}H (n,γ)	2223.25	0.333	100.00%
^{32}S (n,γ)	840.993(13)	0.347	66.73%
^{32}S (n,γ)	2379.661(14)	0.208	40.00%
^{32}S (n,γ)	2930.67(3)	0.0832	16.00%
^{32}S (n,γ)	3220.588(17)	0.117	22.50%
^{32}S (n,γ)	5420.574(24)	0.308	59.23%

Table E.2. Vanadium data

^{51}V	MW	50.94396	Abundance	99.750%	
	n,g Xs	4.9 ± 0.1			
Selected Prompt Gammas					
Energy	Yield	Energy	Yield	Energy	Yield
147.8	5.2%	1358.5	3.1%	5752.1	7.5%
295.0	3.3%	1558.8	6.6%	5892.1	2.6%
419.5	5.1%	1778.0	3.4%	6464.9	8.8%
436.6	8.1%	2145.8	2.9%	6517.3	15.9%
645.7	15.7%	2422.2	2.3%	6874.2	10.0%
793.5	4.1%	5142.4	4.1%	7162.9	12.0%
823.2	6.5%	5210.1	5.0%	7310.7	4.6%
845.9	5.1%	5515.8	8.0%		
^{52}V	$T_{1/2}$	3.743 min			
Selected Decay Gammas					
Energy	Yield				
1434.1	100%				
1530.67	2.4%				

Appendix F. Modified Analysis Scripts

```
$REM Efficiency Calibration Template
$REM
$SEC EffCal
$NOFF
""
$REM  $PH "Efficiency Calibration Report             |DDDDDDD
|TTTTTTTTTT     |I" #datetime #datetime
$REM  $NP 57
$SETE #IV10 1
$REM ----1---------2---------3---------4---------5---------6---------7-
--------
"**********************************************************************
****"
"*****   E F F I C I E N C Y   C A L I B R A T I O N   R E P O R T
*****"
"**********************************************************************
****"
""
"     Detector Name:  |AAAAAAAAAAAAAAAAAAAAAAAAAAAAAAA" DETNAME
"     Sample Title:
|AAAAAAAAAAAAAAAAAAAAAAAAAAAAAAAAAAAAAAAAAAAAAAAAA" STITLE
""
"     Geometry Description: |AAAAAAAAAAAAAAA" GEOMETRY
"     Efficiency Calibration Performed on:  |DDDDDDD |TTTTTTTTTT"
DCALTIME DCALTIME
"                       by: |AAAAAAAAAAAAAAAAAAAAAAA" EFOPNAME
"     Geometry Type Used:   |AAAAAAAAAAAAAAA" EFFTYPE
""
$IF ENTCNT(DENERGY,#IV10)
$SETE #IV1 1
$SETE #IV2 1
"Efficiency Triplets"
"==================="
""
"Energy             Efficiency        Error"
$BT ENTCNT(DENERGY,#IV1)
"|FFFF.FF        |EEEEEEEEEEEEE     |EEEEEEEEEEEEE" DENERGY(1,#IV2)
DEFF(1,#IV2) DEFFERR(1,#IV2)
$SETA #IV2 1
$ET
$ENDIF
""
"DUAL Efficiency Calibration Equation"
"        Form=>   ln(eff)= SUM [Ai*ln(Energy)^(i-1)]"
$IF CROSSOVER
"           Crossover Point ----->   |FFFF.FF" CROSSOVER
""
$IF DLCALFAC1
"Offset      A1:  |EEEEEEEEEEEEEEEEEEEEEEEEEEEEEEEEEEE" DLCALFAC1
"Slope       A2:  |EEEEEEEEEEEEEEEEEEEEEEEEEEEEEEEEEEE" DLCALFAC2
"Quadratic   A3:  |EEEEEEEEEEEEEEEEEEEEEEEEEEEEEEEEEEE" DLCALFAC3
"Cubic       A4:  |EEEEEEEEEEEEEEEEEEEEEEEEEEEEEEEEEEE" DLCALFAC4
"4th Order   A5:  |EEEEEEEEEEEEEEEEEEEEEEEEEEEEEEEEEEE" DLCALFAC5
"5th Order   A6:  |EEEEEEEEEEEEEEEEEEEEEEEEEEEEEEEEEEE" DLCALFAC6
```

```
""
$ELSE
"                                    No DUAL Low Equation"
""
$ENDIF
$IF DHCALFAC1
"Offset       A1:   |EEEEEEEEEEEEEEEEEEEEEEEEEEEEEEEEEEE" DHCALFAC1
"Slope        A2:   |EEEEEEEEEEEEEEEEEEEEEEEEEEEEEEEEEEE" DHCALFAC2
"Quadratic    A3:   |EEEEEEEEEEEEEEEEEEEEEEEEEEEEEEEEEEE" DHCALFAC3
"Cubic        A4:   |EEEEEEEEEEEEEEEEEEEEEEEEEEEEEEEEEEE" DHCALFAC4
"4th Order    A5:   |EEEEEEEEEEEEEEEEEEEEEEEEEEEEEEEEEEE" DHCALFAC5
"5th Order    A6:   |EEEEEEEEEEEEEEEEEEEEEEEEEEEEEEEEEEE" DHCALFAC6
"6th Order    A7:   |EEEEEEEEEEEEEEEEEEEEEEEEEEEEEEEEEEE" DHCALFAC7
"7th Order    A8:   |EEEEEEEEEEEEEEEEEEEEEEEEEEEEEEEEEEE" DHCALFAC8
"8th Order    A9:   |EEEEEEEEEEEEEEEEEEEEEEEEEEEEEEEEEEE" DHCALFAC9
"9th Order   A10:   |EEEEEEEEEEEEEEEEEEEEEEEEEEEEEEEEEEE" DHCALFAC10
""
$ELSE
"                                    No DUAL High Equation"
""
$ENDIF
$ENDIF
$IFNOT CROSSOVER
$IF DHCALFAC1
"Offset       A1:   |EEEEEEEEEEEEEEEEEEEEEEEEEEEEEEEEEEE" DHCALFAC1
"Slope        A2:   |EEEEEEEEEEEEEEEEEEEEEEEEEEEEEEEEEEE" DHCALFAC2
"Quadratic    A3:   |EEEEEEEEEEEEEEEEEEEEEEEEEEEEEEEEEEE" DHCALFAC3
"Cubic        A4:   |EEEEEEEEEEEEEEEEEEEEEEEEEEEEEEEEEEE" DHCALFAC4
"4th Order    A5:   |EEEEEEEEEEEEEEEEEEEEEEEEEEEEEEEEEEE" DHCALFAC5
"5th Order    A6:   |EEEEEEEEEEEEEEEEEEEEEEEEEEEEEEEEEEE" DHCALFAC6
"6th Order    A7:   |EEEEEEEEEEEEEEEEEEEEEEEEEEEEEEEEEEE" DHCALFAC7
"7th Order    A8:   |EEEEEEEEEEEEEEEEEEEEEEEEEEEEEEEEEEE" DHCALFAC8
"8th Order    A9:   |EEEEEEEEEEEEEEEEEEEEEEEEEEEEEEEEEEE" DHCALFAC9
"9th Order   A10:   |EEEEEEEEEEEEEEEEEEEEEEEEEEEEEEEEEEE" DHCALFAC10
$ELSE
"                                    No DUAL Equation"
""
$ENDIF
$ENDIF
$NP
""
"EMPIRICAL Efficiency Calibration Equation"
"         Form=>    ln(eff)= SUM [Ai*(ln(S/Energy)^(i-1)]"
$IF DCALFAC1
"Scaling       S:   |EEEEEEEEEEEEEEEEEEEEEEEEEEEEEEEEEEE" DCALFAC1
"Offset       A1:   |EEEEEEEEEEEEEEEEEEEEEEEEEEEEEEEEEEE" DCALFAC2
"Slope        A2:   |EEEEEEEEEEEEEEEEEEEEEEEEEEEEEEEEEEE" DCALFAC3
"Quadratic    A3:   |EEEEEEEEEEEEEEEEEEEEEEEEEEEEEEEEEEE" DCALFAC4
"Cubic        A4:   |EEEEEEEEEEEEEEEEEEEEEEEEEEEEEEEEEEE" DCALFAC5
"4th Order    A5:   |EEEEEEEEEEEEEEEEEEEEEEEEEEEEEEEEEEE" DCALFAC6
"5th Order    A6:   |EEEEEEEEEEEEEEEEEEEEEEEEEEEEEEEEEEE" DCALFAC7
$ELSE
"                                    No EMPIRICAL Equation"
""
```

```
$ENDIF
""
"LINEAR Efficiency Calibration Equation"
"        Form=>   log(eff)= SUM [Ai*Energy^(2-i)]"
$IF LNCALFAC1
"Offset      A1:  |EEEEEEEEEEEEEEEEEEEEEEEEEEEEEEEEEEE" LNCALFAC1
"Slope       A2:  |EEEEEEEEEEEEEEEEEEEEEEEEEEEEEEEEEEE" LNCALFAC2
"Quadratic   A3:  |EEEEEEEEEEEEEEEEEEEEEEEEEEEEEEEEEEE" LNCALFAC3
"Cubic       A4:  |EEEEEEEEEEEEEEEEEEEEEEEEEEEEEEEEEEE" LNCALFAC4
"4th Order   A5:  |EEEEEEEEEEEEEEEEEEEEEEEEEEEEEEEEEEE" LNCALFAC5
"5th Order   A6:  |EEEEEEEEEEEEEEEEEEEEEEEEEEEEEEEEEEE" LNCALFAC6
"6th Order   A7:  |EEEEEEEEEEEEEEEEEEEEEEEEEEEEEEEEEEE" LNCALFAC7
"7th Order   A8:  |EEEEEEEEEEEEEEEEEEEEEEEEEEEEEEEEEEE" LNCALFAC8
"8th Order   A9:  |EEEEEEEEEEEEEEEEEEEEEEEEEEEEEEEEEEE" LNCALFAC9
"9th Order  A10:  |EEEEEEEEEEEEEEEEEEEEEEEEEEEEEEEEEEE" LNCALFAC10
$ELSE
"                                 No LINEAR Equation"
""
$ENDIF
$REM ------------------------------------------------------------------
----------------------------
```

```
$REM Basic Peak Analysis Template
$SEC PeakAnalysis
$NOFF
$PH "Peak Analysis Report             |DDDDDDD |TTTTTTTTTT
Page |I" #datetime #datetime #pagenum
$NP 57
""
$IF PADATE
$REM ----1---------2---------3---------4---------5---------6---------7-
--------
"**********************************************************************
****"
"*****           P E A K    A N A L Y S I S    R E P O R T
*****"
"**********************************************************************
****"
""
""
$DEFL DETNAME STITLE PADATE PASTART PAEND
$GETL 1 1 0
"     Detector Name:  |AAAAAAAAAAAAAAAAAAAAAAAAAAAAAAA" #LIS1(1)
"     Sample Title:
|AAAAAAAAAAAAAAAAAAAAAAAAAAAAAAAAAAAAAAAAAAAAAAAAA" #LIS1(2)
"     Peak Analysis Performed on:  |DDDDDDD |TTTTTTTTTT" #LIS1(3)
#LIS1(3)
"               Peak Analysis From Channel:  |IIII" #LIS1(4)
"               Peak Analysis To Channel:    |IIII" #LIS1(5)
""
```

```
"Energy      Net Peak         Net Area          Continuum "
" (keV)      Area             Uncert.           Counts "
$SETE #IV1 1
$SETE #IV5 14
$SETE #IV7 0
$SETE #IV9 RECCNT(PSORIGAREA)
$REC 1 PSLEFT 1 0 #IV9
$REC 2 PSPWIDTH 1 0 #IV9
$REC 3 PSCENTRD 1 0 #IV9
$REC 4 PSENERGY 1 0 #IV9
$REC 5 PSORIGAREA 1 0 #IV9
$REC 6 PSORIGERR 1 0 #IV9
$REC 7 PSBACKGND 1 0 #IV9
$REC 8 PSPPFIT 1 0 #IV9
$REC 9 PSPMULT 1 0 #IV9
$REC 10 PSPPADONE 1 0 #IV9
$BT #IV9
$IF #REC10(#IV1)
$SETE #IV2 #REC1(#IV1)
$SETA #IV2 #REC2(#IV1)
$SETS #IV2 1
$IF #REC8(#IV1)
  $IF #REC9(#IV1)
    $SETE #SV1 ' M'
  $ELSE
    $SETE #SV1 'F '
  $ENDIF
$ELSE
  $IF #REC9(#IV1)
    $SETE #SV1 ' m'
  $ELSE
    $SETE #SV1 '  '
  $ENDIF
$ENDIF
"|FFFF.FF |EEEEEEEEEEEEEEE  |EEEEEEEEEEEEEEE  |EEEEEEEEE " #REC4(#IV1)
#REC5(#IV1) #REC6(#IV1)/EM #REC7(#IV1)
$ENDIF
$IFNOT #REC3(#IV1)
$SETA #IV7 1
$ENDIF
$SETA #IV1 1
$REM If new page print column headers.
$REM $SETA #IV5 1
$REM $SETE #IV6 #IV5
$REM $SETD #IV6 56
$REM $IF #IV6
$REM $NP
$REM $SETE #IV5 6
$REM ""
$REM "   Peak  ROI  ROI    Peak    Energy   Net Peak Net Area
Continuum "
$REM "    No. start end  centroid   (keV)     Area    Uncert.    Counts
"
$REM ""
```

```
$REM $ENDIF
$ET
""
$IF #IV7
"One or more peaks were dropped due to multiplet de-convolution."
$ENDIF
"M = First peak in a multiplet region"
"m = Other peak in a multiplet region"
"F = Fitted singlet"
""
"Errors quoted at |F.FFF sigma" 1.0/EM
$ELSE
"No peak analysis results available for reporting purposes"
$ENDIF
$REM
$REM
```

References

[1] R.L. Paul, R.M. Lindstrom, “Prompt Gamma-ray Activation Analysis: Fundamentals and Applications,” J. Radioanal. Nucl. Chem., **243**, pp 181-189 (2000).

[2] F.J. Webb, “Cold Neutron Beams from Small Low-Temperature Moderators in Reactors,” Nucl. Sci. and Eng., **9**, p 120 (1961).

[3] B.W. Wehring, J. Kim, K. Ünlü, “Neutron Focusing System for the Texas Cold Neutron Source,” Nucl. Instrum. Meth., **A353**, pp 137-140 (1994).

[4] H. Chen, D.F.R. Mildner, R.G. Downing, R.L. Paul, R.M. Lindstrom, C.J. Zeissler, Q.F. Xiao and V.A. Sharov, “Prompt Gamma Activation Analysis Enhanced by a Neutron Focusing Capillary Lens,” Nucl. Instrum. Meth., **B95**, pp 107-114 (1995).

[5] D.F.R. Mildner, H.H. Chen-Mayer, “Neutron Absorption Measurements Using Converging Beams – Increased Reaction Rate,” Nucl. Instrum. Meth., **A422**, pp 21-25 (1999).

[6] H.H. Chen-Mayer, E.A. Mackey, R.L. Paul, D.F.R. Mildner, “Quantitative Prompt Gamma Analysis Using a Focused Cold Neutron Beam,” J. Radioanal. Nucl. Chem., **244**, pp 391-397 (2000).

[7] H.D. Choi et al, “Development of a Database for Prompt Gamm-ray Neutron Activation Analysis,” Int. Con. On Nucl. Data for Sci. and Tech., Tsukuba, Japan, Oct. 7-12, 2001.

[8] R.L. Paul, R.M. Lindstrom, A.E. Heald, “Cold Neutron Prompt Gamma-Ray Activation Analysis at NIST – Recent Developments,” J. Radioanal. Nucl. Chem., **215**, pp 63-68 (1997).

[9] J.R.D. Copley, C.A. Stone, “Neutron Scattering and Its Effect on Reaction Rates in Neutron Absorption Experiments,” Nucl. Instrum. Meth., **A281**, pp 593-604 (1989).

[10] J.R.D. Copley, “Scattering Effects Within an Absorbing Sphere Immersed in a Field of Neutrons,” Nucl. Instrum. Meth., **A307**, pp 389-397 (1991).

[11] E.A. Mackey, J.R.D. Copley, “Scattering and Absorption Effects in Neutron Beam Activation Analysis Experiments,” J. Radioanal. Nucl. Chem., **167**, pp 127-132 (1993).

[12] R.L. Paul, E.A. Mackey, “Neutron Scattering by Hydrogen in Cold Neutron Prompt Gamma-Activation Analysis,” J. Radioanal. Nucl. Chem., **181**, pp 321-333 (1993).

[13] R.M. Lindstrom, R.L. Paul, D.H. Vincent, R.R. Greenberg, “Measuring Hydrogen by Cold-Neutron Prompt-Gamma Activation-Analysis,” J. Radioanal. Nucl. Chem., **180**, pp 271-275 (1994).

[14] E.A. Mackey, “Effects of Target Temperature on Analytical Sensitivities of Cold Neutron Capture Prompt γ-Ray Activation Analysis,” Biol. Trace Elem. Res., **43-45**, pp 103-108 (1994).

[15] R.M. Lindstrom, personal communication, (2003).

[16] S.C. Hight et al, “Analysis of Dietary Supplements for Nutritional, Toxic, and Other Elements,” J. Food Composition and Analysis, **6**, pp 121-139 (1993).

[17] D.L. Anderson, “Neutron Capture Prompt Gamma-ray Activation Analysis of Meat Homogenates,” J. Radioanal. Nucl. Chem., **244**, pp 225-229 (2000).

[18] R.L. Paul, “Hydrogen Measurement by Prompt Gamma-ray Activation Analysis, a Review,” Analyst, **122**, pp 35R-41R (1997).

[19] R.L. Paul, “Nondestructive Measurement of Hydrogen and Other Elements by Cold Neutron Prompt Gamma-ray Activation Analysis,” American Laboratory, February, pp 15-20 (2002).

[20] F. Krug, T. Schober, R. Paul, T. Springer, “Investigation of the Hydrogen Uptake of Doped SrCeO3 by TEM, Thermogravimetry, and Cold Neutron Prompt Gamma Activation Analysis (CNPGAA),” Solid State Ionics, **77**, pp 185-188 (1995).

[21] Rick L. Paul, Hugh M. Privett, Richard M. Lindstrom, Wade J. Richards and Robert R. Greenberg, “Determination of Hydrogen in Titanium Alloys by Cold Neutron Prompt Gamma Activation Analysis,” Metallurgical and Materials Transactions, **27A**, pp 3682-3687 (1996).

[22] R.L. Paul, “Cold Neutron Prompt Gamma-Ray Activation Analysis for the Characterization of High-Tech Materials,” Trans. Am. Nucl. Soc., **87**, p 481 (2002).

[23] C.Y. Jones, B.H. Toby, “Cold Neutron Prompt-Gamma Activation Analysis of Hydrogen in H-ZSM-5,” Trans. Am. Nucl. Soc., **87**, p 482 (2002).

[24] S.K. Young, S. Trevino, “Prompt Gamma Neutron Activation Analysis in the Evaluation of Nafion Membranes,” Trans. Am. Nucl. Soc., **87**, p 482-483 (2002).

[25] S.C. McGuire, G.P. Lamaze, E.A. Mackey, “Trace Element Search in Synthetic Sapphire for Advanced LIGO,” Trans. Am. Nucl. Soc., **87**, p 484 (2002).

[26] H.H. Saleh, R.A. Livingston, “Neutron Capture Measurement of Chloride Distribution in Concrete,” Trans. Am. Nucl. Soc., **87**, p 487 (2002).

[27] T. Belgya, Zs. Revay, B. Fazekas, I. Hejja, L. Dabolczi, G. L. Molnar, Z. Kis, J. Ostor, Gy. Kaszas, “The New Budapest Capture Gamma-ray Facility,” Proc. 9th Int. Symp. Capture Gamma-ray Spectroscopy and Related Topics, Budapest, Hungary, pp 826-837 (1996).

[28] G. Molnar, et al, “The New Prompt Gamma-Activation Analysis Facility at Budapest,” J. Radioanal. Nucl. Chem. **215**, pp 111-115 (1997).

[29] Zs. Revay, et al, “A New Gamma-Ray Spectrum Catalog for PGAA,” J. Radioanal. Nucl. Chem. **244**, pp 383-389 (2000).

[30] G. Molnar, et al, “New Catalog of Neutron Capture γ Rays for Prompt Gamma Activation Analysis,” Nucl. Sci. and Tech., August, pp 1338-1343 (2002).

[31] G.L. Molnar, “Nuclear Data for Activation Analysis,” J. Radioanal. Nucl. Chem. **244**, pp 27-33 (2000).

[32] G.L. Molnar, Zs. Revay, T. Belgya, “Wide Energy Range Efficiency Calibration Method for Ge Detectors,” Nucl. Inst. and Meth., **A489**, pp 140-159 (2002).

[33] K. Tompa, P. Bánki, M. Bokor, G. Lasanda and L. Vasáros, “Diffusible and residual hydrogen in amorphous Ni(Cu)–Zr–H alloys,” J. Alloys and Compounds, In Press (2002).

[34] Zs. Kasztovszky, Zs. Révay, G. Molnár, A. Wootsch, Z. Paál, “Assay determination in supported Pt catalysts by prompt-gamma activation analysis (PGAA),” Catalysis Communications, **3**, pp 553-556 (2002).

[35] Zs. Kasztovszky, Zs. Revay, T. Belgya, G.L. Molnar, “Nondestructive analysis of metals by PGAA at the Budapest Research Reactor,” J. Radioanal. Nucl. Chem., **244**, pp 379-382 (2000).

[36] K. Sudarshan, A. G. C. Nair, R. N. Acharya, Y. M. Scindia, A. V. R. Reddy, S. B. Manohar and A. Goswami, “Capture γ-rays from ^{60}Co as Multi γ-ray Efficiency Standard for Prompt γ-ray Neutron Activation Analysis,” Nucl. Inst. and Meth., **A457**, pp 180-186 (2001).

[37] . H. Byun, G. M. Sun and H. D. Choi, “Beam Characteristics of Polychromatic Diffracted Neutrons Used for Prompt Gamma Activation Analysis,” J. Korean Nucl. Soc., **34**, pp 30-41 (2002).

[38] S.H. Byun, H.D. Choi, “Design Features of a Prompt Gamma Neutron Activation Analysis System at HANARO,” J. Radioanal. Nucl. Chem., **244**, pp 413-416 (2000).

[39] S. H. Byun, G. M. Sun and H. D. Choi, “Development of a prompt gamma activation analysis facility using diffracted polychromatic neutron beam,” Nucl. Instrum. Meth., **A487**, pp 521-529 (2002).

[40] C. Yonezawa, A. Khalik, H. Wood, M. Hoshi, Y. Ito, E. Tachikawa, “The Characteristics of the prompt Gamma-ray Analyzing System at the Neutron Beam Guides of JRR-3M,” Nucl. Instrum. Meth., **A329**, pp 207-216 (1993).

[41] S. Miyamoto, M. Sutoh, A. Shlomoto, S. Yamazaki, K. Nishimura, C. Yonezawa, H. Matuse, M. Hoshi, “Determination of Boron in Animals by Reactor Neutron Induced Prompt Gamma-ray Analysis,” J. Radioanal. Nucl. Chem., **244**, pp 307-309 (2000).

[42] Y. Oura, S. Enomoto, H. Nakahara, H. Matsue, C. Yonezawa, “Prompt Gamma-ray Analysis of Rats,” J. Radioanal. Nucl. Chem., **244**, pp 311-315 (2000).

[43] C. Yonezawa, H. Matsue, K. McKay, P. Povinec, “Analysis of Marine Samples by Neutron-induced Prompt Gamma-ray Technique and ICP-MS,” J. Radioanal. Nucl. Chem., **248**, pp 719-725 (2001).

[44] K. Tanoi, H. Iikura, T. M. Nakanishi, “Elemental Analysis in Cultured Cells, Tobacco and Grape, Treated with Aluminum,” J. Radioanal. Nucl. Chem., **249**, pp 519-522 (2001).

[45] M. Crittin, J. Kern and J. -L. Schenker, “The new prompt gamma-ray activation facility at the Paul Scherrer Institute, Switzerland,” Nucl. Instrum. Meth., **A449**, pp 221-236 (2000).

[46] S. Baechler, P. Kudejova, J. Jolie, J. L. Schenker, N. Stritt, “Prompt Gamma-ray Activation Analysis for Determination of Boron in Aqueous Solutions,” Nucl. Instrum. Meth., **A488**, pp 410-418 (2002).

[47] M. Crittin, J. Jolie, J. Kern, S. J. Mannanal and R. Schwarzbach, “Hydrogen Detection by Prompt Gamma-ray Activation Analysis (PGAA),” J. Alloys and Compounds, **253-254**, pp 156-157 (1997).

[48] S. Baechler, et al, “Non-destructive Analysis of a Bulky Sample from a Natural Fossil Reactor,” J. Radioanal. Nucl. Chem. **250**, pp 39-45 (2001).

[49] M. I. Al-Jarallah, A. A. Naqvi, Fazal-ur-Rehman and F. Abu-jarad, “Fast and Thermal Neutron Intensity Measurements at the KFUPM PGNAA Setup,” Nucl. Instrum. Meth., **A195**, pp 435-441 (2002).

[50] M. Borsaru, M. Biggs, W. Nichols, F. Bos, “The Application of Prompt-Gamma Neutron Activation Analysis to Borehole Logging for Coal,” Applied Radiation and Isotopes, **54**, pp 335-343 (2001).

[51] C. G. Clayton, A. M. Hassan, M. R. Wormald, “Multi-element Analysis of Coal During Borehole Logging by Measurement of Prompt γ-rays from Thermal Neutron Capture,” Int. J. Applied Radiation and Isotopes, **34**, pp 83-93 (1983).

[52] M. Borsaru and Z. Jecny, “Application of PGNAA for Bulk Coal Samples in a 4π Geometry,” Applied Radiation and Isotopes, **54**, pp 519-526 (2001).

[53] C. G. Clayton and M. R. Wormald, “Coal Analysis by Nuclear Methods,” Int. J. Applied Radiation and Isotopes, **34**, pp 3-22 (1983).

[54] M. R. Wormald, C. G. Clayton, “In-situ Analysis of Coal by Measurement of Neutron-induced Prompt γ-rays,” Int. J. Applied Radiation and Isotopes, **34**, pp 71-82 (1983).

[55] R. J. Boyd, “The Partitioning Behaviour of Boron from Tourmaline During Ashing of Coal,” Int. J. Coal Geology, **53**, pp 43-54 (2002).

[56] A. S. Abdel-Haleem, M. A. Abdel-Samad, R. A. Zaghloul, A. M. Hassan, “The uses of Neutron Capture γ-rays in Environmental Pollution Measurements,” Radiation Physics and Chemistry, **47**, pp 719-722 (1996).

[57] Jiunn-Hsing Chao, Chien Chung, “In situ Prompt Gamma-ray Measurement of River Water Salinity in Northern Taiwan using HPGe—^{252}Cf Probe,” Int. J. Radiation Applications and Instrumentation, **A42**, pp 723-728 (1991).

[58] Jiunn-Hsing Chao, Chien Chung, "In situ Lake Pollutant Survey using Prompt-gamma Probe," Int. J. Radiation Applications and Instrumentation, **A42**, pp 735-740 (1991).

[59] Chien Chung, Tzu-Cheng Tseng, "In situ Prompt Gamma-ray Activation Analysis of Water Pollutants using a Shallow ^{252}Cf-HPGe Probe," Nucl. Instrum. Meth., **A267**, pp 223-230 (1988).

[60] Chien Chung, Sheng-Ming Liu, Jiunn-Hsing Chao, Cheng-Chan Chan, "Feasibility Study of Explosive Detection for Airport Security using a Neutron Source," Applied Radiation and Isotopes, **44**, pp 1425-1434 (1993).

[61] A. Tavakkoli Farsoni, S. A. Mireshghi, "Design and Evaluation of a TNA Explosive-Detection System to Screen Carry-on Luggage," J. Radioanal. Nucl. Chem., **248**, pp 695-697 (2001).

[62] P. A. Dokhale, J. Csikai, L. Oláh, "Investigations on Neutron-induced Prompt Gamma Ray Analysis of Bulk Samples," Applied Radiation and Isotopes, **54**, pp 967-971 (2001).

[63] W. V. Nunes, A. X. da Silva, V. R. Crispim, R. Schirru, "Explosives Detection using Prompt-gamma Neutron Activation and Neural Networks," Applied Radiation and Isotopes, **56**, pp 937-943 (2002).

[64] S. Pesente, M. Cinausero, D. Fabris, E. Fioretto, M. Lunardon, G. Nebbia, G. Prete, G. Viesti, "Effects of Soil Moisture on the Detection of Buried Explosives by Radiative Neutron Capture," Nucl. Instrum. Meth., **A459**, pp 577-580 (2001).

[65] T.E. Valentine, “Evaluation of Prompt Fission Gamma Rays for use in Simulating Nuclear Safeguard Measurements,” Annals of Nuclear Energy, **28**, pp 191-201 (2001).

[66] Samir Abdul-Majid, “Corrosion and Scale Measurements in Iron Pipes by Prompt Gamma-ray Analysis,” Nucl. Instrum. Meth., **B73**, pp 398-402 (1993).

[67] R. P. Gardner, P. Guo, Y. Y. Wang, A. Sood, S. H. Lee and C. L. Dobbs, “Feasibility of Neutron Activation Methods for Measurement of Sodium and Aluminum in Green Liquor,” Applied Radiation and Isotopes, **48**, pp 1355-1372 (1997).

[68] S. Schneider and T. D. Fay, “Space Material Resource Identification Technology,” Advances in Space Research, **13**, pp 71-78 (1993).

[69] D.J. Dorsey, W.S. Charlton, R. Hebner, “Experimental Measurements of Water Content in Carbon Composites Using PGAA,” Trans. Am. Nucl. Soc., **86**, pp 389-391 (2002).

[70] J.F. Briesmeister, Ed., "MCNP - A General Monte Carlo N-Particle Transport Code, Version 4B," LA-12625-M, Los Alamos National Laboratory (1997).

[71] C. Oliveira, J. Salgado, “Calibration Curves of a PGNAA System for Cement Raw Material Analysis Using the MCNP Code,” Applied Radiation and Isotopes, **49**, pp 1685-1689 (1998).

[72] S.L. Howell, R.A. Sigg, F.S. Moore, T.A. DeVol, “Calibration and Validation of a Monte Carlo model for PGNAA of Chlorine in Soil,” J. Radioanal. Nucl. Chem., **244**, pp 173-178 (2000).

[73] E. Schmidt, P.F. Rose, "Monte Carlo Calculations of Neutron Induced Prompt Spectra," J. Applied Radiation and Isotopes, **35**, pp 796-798 (1984).

[74] J. Tickner, "Determination of the Spatial Response of Neutron Based Analysers Using a Monte Carlo Based Method," Applied Radiation and Isotopes, **53**, pp 507-513 (2000).

[75] T.C. Clark, Robin P. Gardner, K. Verghese, "A Monte Carlo Model for In situ Prompt Gamma-ray Analysis Probes," Nucl. Inst. Meth, **193**, pp 365-370 (1982).

[76] C.J. Evans, S.J.S. Ryde, D.A. Hancock, F. Al-Agel, "Monte Carlo Simulation of Prompt Gamma Neutron Activation Analysis Using MCNP Code," Applied Radiation and Isotopes, **49**, pp 541-543 (1998).

[77] R. J. Shypailo, K. J. Ellis, "Estimation of Background Interference in Prompt-Gamma Neutron Activation Using MCNP," J. Radioanal. Nucl. Chem., **249**, pp 407-412 (2001).

[78] G. E. Nicolaou, Y. S. Khrbish, N. M. Spyrou, "The Effect of Solid Angle on the Reproducibility of an Experimental Set-up in Prompt Gamma-ray Neutron Activation Analysis," Int. J. Radiation Applications and Instrumentation, **A37**, pp 1219-1224 (1986).

[79] A. A. Naqvi, M. M. Nagadi, Khateeb-ur-Rehman, M. Maslehuddin, S. Kidwai, "Monte Carlo Simulations for Design of the KFUPM PGNAA Facility," Radiation Physics and Chemistry, In Press, Corrected Proof (2002).

[80] C. Oliveira, J. Salgado, I. F. Gonçalves, F. G. Carvalho, F. Leitão, "A Monte Carlo Study of the Influence of the Geometry Arrangements and Structural Materials on a

PGNAA System Performance for Cement Raw Material Analysis," Applied Radiation and Isotopes, **48**, pp 1349-1354 (1997).

[81] C. Oliveira, J. Salgado, F. Leitão, "Density and Water Content Corrections in the Gamma Count Rate of a PGNAA System for Cement Raw Material Analysis using the MCNP Code," Applied Radiation and Isotopes, **49**, pp 923-930 (1998).

[82] M.A. Lone, R.A. Leavitt, D.A. Harrison, *Prompt Gamma Rays from Thermal-Neutron Capture*, Atomic Data and Nuclear Data Tables, **26**, 511 (1981).

[83] J.K. Tuli, "Evaluated Nuclear Structure File – A Manual for Preparation of Data Sets," BNL-NCS-51655-01/02-Rev (2001).

[84] R.C. Greenwood, R.G. Helmer, "Gamma-ray Energies from $^{14}N(n,\gamma)^{15}N$ and $^{23}Na(n, \gamma)^{24}Na$ Reactions: a Re-evaluation," Nucl. Instrum. Meth., **121**, pp 385-389 (1974).

[85] R.C. Reedy, S.C. Frankle, "Prompt Gamma Rays from Radiative Capture of Thermal Neutrons by Elements from Hydrogen through Zinc," Atomic Data and Nuclear Data Tables, **80**, pp 1-34 (2002).

[86] S.F. Mughabghab, M. Divadeenam, N.E. Holden, *Neutron Cross Sections*, Academic Press (1981).

[87] G.L. Molnar, "Nuclear Data for Activation Analysis," J. Radioanal. Nucl. Chem., **244**, pp 27-33 (2000).

[88] L. Venturini, B.R.S. Pecequilo, "Thermal Neutron Capture Cross-section of ^{48}Ti, ^{51}V, $^{50,52,53}Cr$ and $^{58,60,62,64}Ni$," Applied Radiation and Isotopes, **48**, pp 493-496 (1997).

[89] S.C. Frankle, R.C. Reedy, P.G. Young, W.P. Madigan, “Improvements to the Photon-Production Data for Radiative Capture in ENDF,” Applied Radiation and Isotopes, **53**, pp 929-935 (2000).

[90] G.Y. Baaklini, K.E. Konno, R.E. Martin, and R. Thompson, “NDE Methodologies for Composite Flywheels Certification,” NASA TM—2000-210473 00PS–63, National Aeronautics and Space Administration (2000).

[91] ASTM Std. D 3171 – 99, “Standard Test Methods for Constituent Content of Composite Materials,” (2000).

[92] A.K. Mal, Y. Bar-Cohen, “Ultrasonic NDE of Thick Composite Laminates,” Review of Progress in Quantitative NDE, **8A**, D.O. Thompson, D.E. Chimenti (Eds.), Plenum Press, NY, pp 1551-1558 (1989).

[93] P.B. Nagy, L. Adler, D. Mih, W. Sheppard, “Single Mode Lamb Wave Inspection of Composite Laminates,” Review of Progress in Quantitative NDE, **8A**, D.O. Thompson, D.E. Chimenti (Eds.), Plenum Press, NY, pp 1535-1542 (1989).

[94] C. Potel, T. Chotard, J. de Belleval, M. Benzaggagh, “Characterization of Composite Materials by Ultrasonic Methods: Modelization and Application to Impact Damage,” Composites, **29B**, pp 159-169 (1998).

[95] N. Guo, P. Cawley, “Lamb Wave Reflection for the Quick Evaluation of Large Composite Laminates,” Materials Evaluation, **52**, 12, pp 404-441 (1994).

[96] J. Zhou and J. P. Lucas, “Hygrothermal effects of epoxy resin. Part I: the nature of water in epoxy,” Polymer, **40**, pp 5505-5512 (1999).

[97] D.A. Froom, W.E. Larson, E.F. Kasper, "Solving Problems with Advanced Technology," Proc. IEEE Digital Avionics Systems Conference, pp 3.D.5-1 – 3.D.5-8 (1999).

[98] L.G.I. Bennett, M.L. Bickerton, W.J. Lewis, " Development of Techniques for the Neutron Radiography of CF 188 Flight Control Surfaces," Nuc. Inst. And Meth., **424A**, pp 104-112 (1999).

[99] D. Cohen, S.C. Mantell, L. Zhao, "The Effect of Fiber Volume Fraction on Filament Wound Composite Pressure Vessel Strength," Composites, **32B**, pp 413-429 (2001).

[100] ASTM Std. D 5300 – 93, "Standard Test Method for Measurement of Resin Content and Other Related Properties of Polymer Matrix Thermoset Prepeg by Combined Mechanical and Ultrasonic Methods," (1993).

[101] K.H. Kim, R.T. Klann, B.B. Raju, "Fast Neutron Radiography for Composite Materials Evaluation and Testing," Nucl. Instrum. Meth., **A422**, pp 929-932 (1999).

[102] J. T. Lindsay, M. Matsubayashi, M. N. Islam, "Water Diffusion Profile Measurements in Epoxy Using Neutron Radiography," Nucl. Instrum. Meth., A**353**, pp 149-151 (1994).

[103] D.S. O'Kelly, "Hydrogen and Oxygen Gas Production in the UT TRIGA Reactor," Trans. Am. Nucl. Soc., **83**, pp 504-505 (2000).

[104] D.J. Dorsey, W.S. Charlton, "Monte Carlo Evaluation of a New Reflector for the UT TRIGA Reactor," Trans. Am. Nucl. Soc., **85**, pp 418-419 (2001).

[105] K. Unlu, C. Rios-Martinez, B.W. Wehring, "The University of Texas Cold Neutron Source," Nucl. Instr. Meth, **A353**, pp 397-401 (1994).

[106] K. Unlu, et al, "Design Features of the Texas Cold Neutron Source," Trans. Am. Nucl. Soc., **65**, pp 134-135 (1992).

[107] J. Kim, "Neutron Focusing System for the Texas Cold Neutron Source," Ph.D. Dissertation, The University of Texas at Austin (1993).

[108] B.W. Wehring, J.Y. Kim, K. Unlu, "Neutron Focusing System for the Texas Cold Neutron Source," Nucl. Instr. Meth., **A353**, pp 137-140 (1994).

[109] J.Y. Kim, B.W. Wehring, K. Unlu, "Converging Guide for the Neutron Focusing at the Texas Cold Neutron Source," Trans. Am. Nucl. Soc., **69**, pp 166-167 (1993).

[110] K. Unlu, C. Rios-Martinez, B.W. Wehring, "Performance of the Texas Cold Neutron Source," Trans. Am. Nucl. Soc., **66**, pp 160-161 (1992).

[111] K. Unlu, et al, " Performance of the Texas Cold Neutron Source at Reactor Power," Trans. Am. Nucl. Soc., **69**, pp 164-165 (1993).

[112] C. Rios-Martinez, "Prompt Gamma Activation Analysis using the Texas Cold Neutron Source," Ph.D. Dissertation, The University of Texas at Austin (1995).

[113] B.W. Wehring, K. Unlu, C. Rios-Martinez, "Application of Cold-neutron Prompt Gamma Activation Analysis at the University of Texas Reactor," *Appl. Radiation Isotopes*, **48**, pp 1343 – 1348 (1997).

[114] R. J. Parsons, "The Reduction of the Influence of Formation Properties on the Calibration of a Prompt γ-ray Interaction Analysis Probe," Int. J. Applied Radiation and Isotopes, **34**, pp 137-142 (1983).

[115] T. He, R.P. Gardner, K. Verghese, "The Monte Carlo – Library Least Squares Approach for Energy-Dispersive x-Ray Fluorescence Analysis", Appl. Radiat. Isot., **44**, pp 1381-1388 (1993).

[116] R. P. Gardner, A. Sood, Y. Y. Wang, L. Liu, P. Guo and R. J. Gehrke, "Single Peak Versus Library Least-Squares Analysis Methods for the PGNAA Analysis of Vitrified Waste," Applied Radiation and Isotopes, **48**, pp 1331-1335 (1997).

[117] Q. Ao, S.H. Lee, R.P. Gardner, "Development of the Specific Purpose Monte Carlo Code CEARXRF for the Design and Use of in Vivo X-ray Fluorescence Analysis Systems for Lead in Bone," Appl. Radiat. Isot., **48**, pp 1403-1412 (1997).

[118] G.L. Molnar, Zs. Revay, R.L. Paul, R.M. Lindstrom, "Prompt-gamma Activation Analysis using the k_0 Approach," J. Radioanal. Nucl. Chem., **234**, pp 21-26 (1998).

[119] F. De Corte, "k_0 and Comparator NAA: Influences and Interactions," J. Radioanal. Nucl. Chem., **245**, pp 157-161 (2000).

[120] H. Matsue, C. Yonezawa, "k_0 Standardization Approach in Neutron-induced Prompt Gamma-ray Analysis at JAERI," J. Radioanal. Nucl. Chem., **245**, pp 189-194 (2000).

[121] R. N. Acharya, et al, "Measurement of k_0-factors in Prompt Gamma-ray Neutron Activation Analysis," J. Radioanal. Nucl. Chem., **250**, pp 303-307 (2000).

[122] H. Matsue, C. Yonezawa, “Multielement Determination of Typical Diet Reference Materials by Neutron-induced Prompt Gamma-ray Analysis using k_0 Standardization,” J. Radioanal. Nucl. Chem., **249**, pp 11-14 (2001).

[123] L.A. Curie, “Limits for Qualitative Detection and Quantitative Determination,” *Anal. Chem.*, **40**, 3, pp 586 – 593 (1968).

VITA

Daniel John Dorsey was born in Mt. Holly, New Jersey, on October 20, 1976, the son of Timothy and Margaret Dorsey. He graduated from Brazoswood High School in Clute, Texas, in 1994 and entered the Nuclear Engineering Department at Texas A&M University in College Station, Texas. He completed a Bachelor of Science degree in Nuclear Engineering in 1998, and continued at Texas A&M University until the completion of a Master of Science degree in 2000. In the Fall of 2000, he entered The Graduate School at The University of Texas at Austin and continued to pursue graduate study towards a Ph.D. in Nuclear Engineering.

He has been married to Staci Ross since February of 2000.

Permanent Address: 102 Silverlace
Lake Jackson, TX 77566

This dissertation was typed by the author.